APPENDICES

APPENDIX A

The Joint Committee for Powder Diffraction Standards (JCPDS)

$SrWO_4$, JCPDS file number 00-008-0490 [91]

Name and formula

Reference code:	00-008-0490		
PDF index name:	Strontium Tungsten Oxide		
Empirical formula:	O_4SrW		
Chemical formula:	$SrWO_4$		

Crystallographic parameters

Crystal system:	Tetragonal		
Space group:	I41/a		
Space group number:	88		
a:	5.4168	α:	90.0000
b:	5.4168	β:	90.0000
c:	11.9510	γ:	90.0000
Calculated density:	6.35	Volume of cell:	350.66
Z:	4.00	RIR:	-

Subfiles and Quality

Subfiles:	Inorganic, Corrosion, Common Phase, NBS pattern

Quality: Star (S)

Comments

Color: Colorless

Sample preparation: Sample precipitated from solutions of $SrCl_2$ and Na_2WO_4 .

Analysis: Spectroscopic analysis showed <0.1% Ba, Ca, K, Na, Si; <0.01% Al, Cu, Li, Mg, Sb; <0.001% Ag, Cr, Cs, Fe, Rb.

Temperature: Pattern made at 25 °C.

References

Primary reference: *Natl. Bur. Stand. (U.S.), Circ. 539*, **7**, 53, (1957)

Peak list

No.	h	k	l	d [A]	2Theta[deg]	I [%]
1	1	0	1	4.93000	17.978	20.0
2	1	1	2	3.22300	27.655	100.0
3	0	0	4	2.98700	29.889	16.0
4	2	0	0	2.70700	33.065	25.0
5	2	1	1	2.37300	37.884	8.0
6	1	1	4	2.35500	38.185	2.0
7	1	0	5	2.18700	41.246	1.0
8	2	1	3	2.06900	43.716	4.0
9	2	0	4	2.00700	45.139	30.0
10	2	2	0	1.91500	47.437	14.0
11	3	0	1	1.78600	51.100	2.0
12	1	1	6	1.76800	51.658	20.0

13	2	1	5	1.70200	53.819	4.0
14	3	1	2	1.64600	55.807	30.0
15	2	2	4	1.61200	57.091	14.0
16	0	0	8	1.49300	62.121	4.0
17	3	2	1	1.49000	62.260	4.0
18	3	0	5	1.44110	64.623	2.0
19	3	2	3	1.40590	66.447	2.0
20	2	1	7	1.39530	67.018	2.0
21	4	0	0	1.35420	69.336	4.0
22	2	0	8	1.30770	72.179	10.0
23	3	1	6	1.29890	72.746	16.0
24	3	3	2	1.24880	76.170	8.0
25	4	0	4	1.23350	77.289	6.0
26	4	2	0	1.21120	78.986	8.0
27	2	2	8	1.17810	81.665	4.0
28	1	1	10	1.14110	84.916	4.0
29	4	2	4	1.12260	86.656	8.0
30	4	3	1	1.07900	91.107	2.0
31	3	3	6	1.07490	91.553	4.0
32	5	1	2	1.04620	94.832	8.0
33	4	0	8	1.00330	100.307	4.0
34	0	0	12	0.99590	101.333	1.0
35	4	3	5	0.98680	102.632	1.0
36	3	1	10	0.98010	103.615	6.0
37	4	4	0	0.95760	107.106	2.0
38	4	2	8	0.94080	109.924	6.0
39	5	1	6	0.93740	110.519	6.0

Stick Pattern

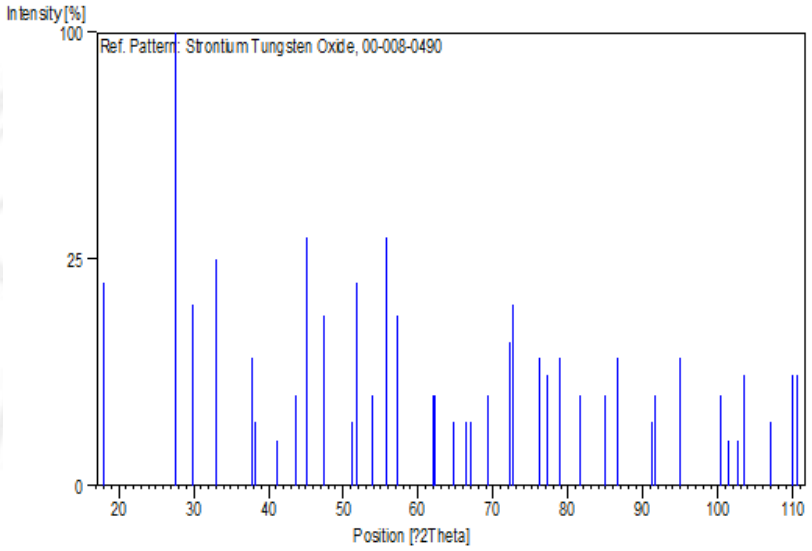

$MgWO_4$, JCPDS file number 00-045-0412 [92]

Name and formula

Reference code:	00-045-0412
PDF index name:	Magnesium Tungsten Oxide
Empirical formula:	MgO_4W
Chemical formula:	$MgWO_4$

Crystallographic parameters

Crystal system:	Anorthic		
a:	5.6079	α:	123.170
b:	6.5792	β:	112.7500
c:	8.8475	γ:	101.3500
Calculated density:	8.45	Volume of cell:	213.83
Z:	4.00	RIR:	-

Subfiles and Quality

Subfiles: Inorganic, Corrosion

Quality: Blank (B)

Comments

General comments: High temperature form. Cell parameters generated by least squares refinement.

Sample preparation: Prepared by dehydration of $MgWO_4 \cdot H_2O$ at 155 ^oC for 7 days.

Unit cell: Reference reports: a=5.60, b=6.58, c=8.84, a=123.2, b=112.7, g=101.4.

References

Primary reference: Gunter, J., Amberg, M., *Solid State Ionics*, **32**, 141, (1989)

Peak list

No.	h	k	l	d [A]	2Theta[deg]	I [%]
1	0	1	-1	6.26000	14.136	36.0
2	0	0	1	5.82300	15.203	22.0
3	1	0	-1	5.37800	16.470	22.0
4	1	-1	0	4.64800	19.079	72.0
5	1	-1	1	3.74400	23.746	31.0
6	1	-1	-1	3.57500	24.886	57.0
7				3.33300	26.725	7.0
8	0	2	-2	3.18800	27.965	100.0
9	1	-2	1	3.04700	29.287	40.0
10	0	0	2	2.96600	30.106	14.0
11	1	-2	0	2.74200	32.631	40.0

12	2	0	-2	2.70500	33.090	23.0
13	2	-1	0	2.58100	34.729	11.0
14	1	2	-3	2.53100	35.438	14.0
15	1	2	-2	2.49200	36.011	15.0
16	1	-1	-2	2.44300	36.759	20.0
17	-1	2	1	2.16200	41.745	25.0
18	0	3	-3	2.13700	42.257	47.0
19	1	-3	1	2.07800	43.517	27.0
20	2	-1	-3	1.89700	47.915	28.0

Stick Pattern

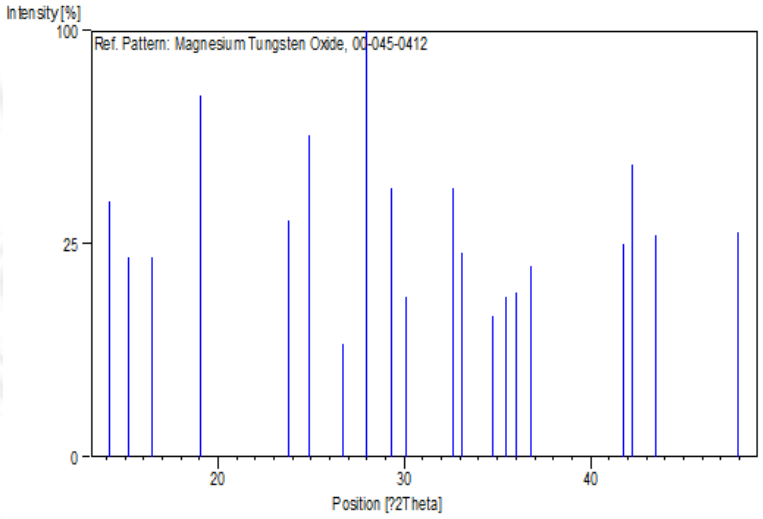

$MgWO_4$, JCPDS file number 01-072-2191 [93]

Name and formula

Reference code: 01-072-2191

ICSD name: Magnesium Tungsten Oxide

Empirical formula: MgO_4W

Chemical formula: $MgWO_4$

Crystallographic parameters

Crystal system:	Monoclinic		
Space group:	P2/c		
Space group number:	13		
a:	4.6800	α:	90.0000
b:	5.6600	β:	90.3330
c:	4.9200	γ:	90.0000
Calculated density:	6.93	Volume of cell:	130.32
Z:	2.00	RIR:	4.48

Subfiles and Quality

Subfiles: Inorganic, Corrosion, ICSD Pattern

Quality: Calculated (C)

Comments

ICSD collection code: 020470

Test from ICSD: At least one TF missing.

References

Primary reference: *Calculated from ICSD using POWD-12++*, (1997)

Structure: Kravchenko, V.B., *Zh. Strukt. Khim.*, **10**, 148, (1969)

Peak list

No.	h	k	l	d [A]	2Theta[deg]	I [%]
1	0	1	0	5.66000	15.644	25.8
2	1	0	0	4.67992	18.948	100.0
3	0	1	1	3.71319	23.946	96.4
4	1	1	0	3.60670	24.664	41.1
5	-1	1	1	2.91504	30.645	80.9
6	1	1	1	2.90262	30.779	90.0

7	0	2	0	2.83000	31.589	13.8
8	0	0	2	2.45996	36.497	23.4
9	0	2	1	2.45312	36.602	32.1
10	1	2	0	2.42166	37.095	14.1
11	2	0	0	2.33996	38.440	11.4
12	0	1	2	2.25609	39.928	2.3
13	-1	0	2	2.18270	41.331	20.4
14	-1	2	1	2.17531	41.478	14.4
15	1	0	2	2.17014	41.581	28.8
16	2	1	0	2.16245	41.736	16.4
17	-1	1	2	2.03651	44.450	5.1
18	1	1	2	2.02804	44.646	6.2
19	-2	1	1	1.98359	45.702	10.6
20	2	1	1	1.97576	45.893	14.6
21	0	3	0	1.88667	48.194	5.1
22	0	2	2	1.85659	49.026	9.4
23	2	2	0	1.80335	50.574	9.1
24	0	3	1	1.76158	51.861	1.3
25	1	3	0	1.74982	52.235	16.9
26	-1	2	2	1.72835	52.934	4.0
27	1	2	2	1.72316	53.106	6.9
28	-2	0	2	1.70038	53.875	10.9
29	-2	2	1	1.69565	54.037	18.3
30	2	2	1	1.69075	54.207	28.1
31	-1	3	1	1.64979	55.668	1.2
32	1	3	1	1.64753	55.751	1.0
33	-2	1	2	1.62848	56.461	2.0
34	2	1	2	1.61983	56.790	1.1

35	0	1	3	1.57518	58.553	5.3
36	3	0	0	1.55997	59.180	2.8
37	3	1	0	1.50390	61.621	1.3
38	-1	1	3	1.49541	62.010	10.5
39	1	1	3	1.49037	62.243	8.8
40	2	3	0	1.46873	63.265	4.8
41	-2	2	2	1.45752	63.808	3.1
42	2	2	2	1.45131	64.114	3.3
43	-3	1	1	1.44047	64.655	7.1
44	3	1	1	1.43596	64.883	8.9
45	-1	3	2	1.42735	65.323	7.1
46	1	3	2	1.42442	65.474	10.4
47	0	2	3	1.41894	65.758	8.4
48	0	4	0	1.41500	65.965	4.8
49	-2	3	1	1.40876	66.295	1.0
50	2	3	1	1.40595	66.444	0.8
51	3	2	0	1.36616	68.644	1.9
52	0	4	1	1.35987	69.006	8.1
53	1	2	3	1.35600	69.231	5.8
54	-3	0	2	1.32089	71.347	1.1
55	-3	2	1	1.31809	71.522	3.3
56	3	2	1	1.31396	71.782	3.9
57	-2	1	3	1.31009	72.027	3.7
58	-1	4	1	1.30642	72.261	5.6
59	2	1	3	1.30333	72.459	4.9
60	-3	1	2	1.28632	73.574	1.2
61	3	1	2	1.27992	74.003	1.0
62	-2	3	2	1.26309	75.158	2.5

63	2	3	2	1.25904	75.442	2.6
64	0	3	3	1.23773	76.976	0.2
65	0	0	4	1.22998	77.551	1.5
66	0	4	2	1.22656	77.808	0.8
67	-2	2	3	1.21601	78.612	1.3
68	2	4	0	1.21060	79.032	1.2
69	3	3	0	1.20223	79.692	3.5
70	-3	2	2	1.19693	80.116	1.2
71	1	3	3	1.19529	80.248	0.5
72	3	2	2	1.19177	80.534	1.4
73	1	0	4	1.18788	80.852	1.9
74	1	4	2	1.18564	81.037	0.9
75	-2	4	1	1.17657	81.794	3.1
76	2	4	1	1.17493	81.932	3.1
77	4	0	0	1.16998	82.354	2.5
78	3	3	1	1.16667	82.639	1.4
79	1	1	4	1.16256	82.995	0.9
80	4	1	0	1.14576	84.490	0.2
81	0	5	0	1.13200	85.762	0.7
82	0	2	4	1.12804	86.136	1.2
83	-4	1	1	1.11730	87.170	1.6
84	4	1	1	1.11450	87.444	2.0
85	-3	1	3	1.11151	87.739	2.2
86	3	1	3	1.10533	88.357	2.1
87	0	5	1	1.10318	88.574	1.3
88	1	5	0	1.10027	88.870	1.6
89	-1	2	4	1.09797	89.106	1.3
90	1	2	4	1.09531	89.380	1.1

91 -2 0 4 1.09135 89.792 1.5

Stick Pattern

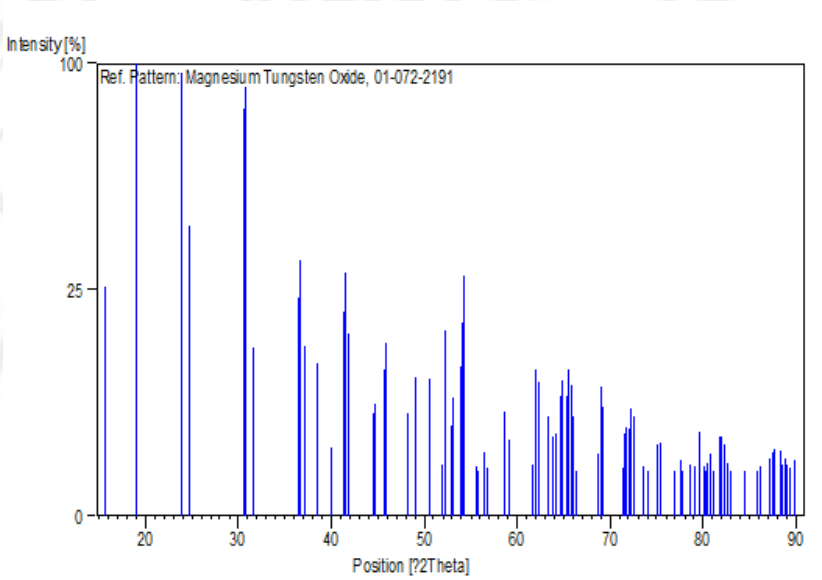

$MgMoO_4$, JCPDS file number 01-072-2153 [94]

Name and formula

Reference code: 01-072-2153

ICSD name: Magnesium Molybdenum Oxide

Empirical formula: $MgMoO_4$

Chemical formula: $MgMoO_4$

Crystallographic parameters

Crystal system: Monoclinic

Space group: C2/m

Space group number: 12

a:	10.2730	α:	90.0000
b:	9.2880	β:	106.9600
c:	7.0250	γ:	90.0000
Calculated density:	3.82	Volume of cell:	641.14
Z:	8.00	RIR:	3.98

Subfiles and Quality

Subfiles: Inorganic, Corrosion, ICSD Pattern

Quality: Calculated (C)

Comments

ICSD collection code: 020418

References

Primary reference: *Calculated from ICSD using POWD-12++*, (1997)

Structure: Bakakin, V.V., Klevtsova, R.F., Gaponenko, L.A., *Kristallografiya*, **27**, 38, (1982

Peak list

No.	h	k	l	d [A]	2Theta[deg]	I [%]
1	1	1	0	6.74986	13.106	2.6
2	-1	1	1	5.32543	16.634	6.8
3	2	0	0	4.91311	18.041	0.3
4	-2	0	1	4.66743	18.999	24.2
5	1	1	1	4.34649	20.416	2.2
6	0	2	1	3.82037	23.265	47.8
7	2	0	1	3.50830	25.367	22.4
8	2	2	0	3.37493	26.387	100.0
9	-1	1	2	3.28146	27.153	26.5
10	-2	0	2	3.25000	27.421	11.7
11	-3	1	1	3.15529	28.261	15.5
12	3	1	0	3.08896	28.881	2.6
13	1	3	0	2.95290	30.242	0.1
14	-1	3	1	2.79278	32.022	13.1
15	0	2	2	2.72207	32.877	4.9
16	-3	1	2	2.66900	33.550	8.8

17	-2	2	2	2.66272	33.631	14.2
18	1	3	1	2.62010	34.195	1.4
19	-4	0	1	2.56062	35.014	0.6
20	3	1	1	2.55272	35.126	0.6
21	2	0	2	2.45655	36.549	7.7
22	0	4	0	2.32200	38.749	7.7
23	-2	0	3	2.30791	38.995	0.9
24	-3	3	1	2.27520	39.579	0.7
25	-1	1	3	2.26589	39.748	1.0
26	3	3	0	2.24995	40.042	5.1
27	-4	2	1	2.24235	40.183	5.1
28	0	4	1	2.19466	41.096	0.4
29	2	2	2	2.17325	41.519	8.9
30	1	3	2	2.12743	42.456	2.6
31	4	0	1	2.11666	42.683	0.5
32	-3	1	3	2.11001	42.824	2.3
33	2	4	0	2.09935	43.052	1.2
34	-4	2	2	2.08523	43.358	4.7
35	-2	4	1	2.07894	43.496	8.0
36	-3	3	2	2.07117	43.668	4.9
37	-2	2	3	2.06676	43.766	5.6
38	0	2	3	2.01744	44.893	2.6
39	1	1	3	2.00891	45.094	4.9
40	-5	1	1	2.00610	45.161	4.7
41	-4	0	3	1.96491	46.162	4.3
42	2	4	1	1.93631	46.884	8.9
43	4	2	1	1.92604	47.149	9.2
44	5	1	0	1.92185	47.258	6.7

45	0	4	2	1.91019	47.564	4.0
46	-2	4	2	1.88933	48.122	1.6
47	-1	3	3	1.86499	48.791	1.9
48	2	0	3	1.84499	49.355	0.8
49	1	5	0	1.82527	49.924	0.2
50	-4	2	3	1.80960	50.387	0.1
51	-1	5	1	1.78609	51.097	0.3
52	-3	3	3	1.77514	51.435	0.2
53	4	0	2	1.75384	52.107	10.4
54	1	5	1	1.73778	52.625	0.6
55	-5	1	3	1.72009	53.208	2.8
56	3	3	2	1.71715	53.307	4.7
57	-1	1	4	1.71193	53.482	6.9
58	2	4	2	1.68747	54.321	7.4
59	-3	1	4	1.68278	54.485	4.6
60	-6	0	2	1.67740	54.674	1.4
61	5	3	0	1.65867	55.344	4.3
62	-4	4	2	1.64603	55.806	2.4
63	-1	5	2	1.64161	55.969	2.5
64	6	0	0	1.63690	56.145	2.1
65	-3	5	1	1.62510	56.589	1.8
66	3	5	0	1.61447	56.995	1.5
67	0	4	3	1.61206	57.088	2.4
68	-6	2	1	1.60469	57.375	0.6
69	0	2	4	1.57969	58.370	5.8
70	1	5	2	1.56861	58.822	1.5
71	4	4	1	1.56427	59.001	0.8
72	1	1	4	1.55859	59.238	0.8

73	-6	0	3	1.55581	59.354	0.5
74	0	6	0	1.54800	59.684	1.5
75	-3	5	2	1.54448	59.834	4.6
76	-4	2	4	1.53381	60.293	6.4
77	5	3	1	1.52492	60.681	0.8
78	3	5	1	1.52204	60.808	0.5
79	-1	3	4	1.51846	60.967	0.6
80	0	6	1	1.50849	61.413	3.8
81	-4	4	3	1.49994	61.802	2.7
82	6	0	1	1.49402	62.074	2.6
83	2	6	0	1.47645	62.896	4.5
84	-2	6	1	1.46930	63.237	1.0
85	2	0	4	1.46415	63.486	1.3
86	4	0	3	1.45699	63.834	0.2
87	-1	5	3	1.45405	63.979	0.3
88	3	3	3	1.44883	64.237	3.8
89	2	4	3	1.44451	64.452	5.9
90	-7	1	2	1.43745	64.807	0.8
91	6	2	1	1.42223	65.587	0.1
92	2	6	1	1.41626	65.899	0.1
93	-3	5	3	1.41025	66.215	0.4
94	0	6	2	1.40594	66.445	0.3
95	4	4	2	1.39949	66.791	4.3
96	2	2	4	1.39639	66.959	2.6
97	-6	0	4	1.39326	67.129	2.0
98	4	2	3	1.39018	67.298	2.0
99	-3	1	5	1.37883	67.927	1.7
100	-5	5	1	1.37692	68.034	1.9

101	-6	4	2	1.35972	69.015	2.5
102	-4	0	5	1.35746	69.146	2.0
103	5	5	0	1.34969	69.601	0.7
104	-2	2	5	1.34458	69.904	2.4
105	-6	2	4	1.33450	70.510	0.1
106	3	1	4	1.33015	70.776	0.3
107	6	0	2	1.32748	70.939	0.6
108	-4	6	1	1.32474	71.108	1.4
109	-7	3	1	1.32209	71.273	1.0
110	-7	3	2	1.31681	71.602	0.6
111	2	6	2	1.31005	72.029	1.4
112	-4	2	5	1.30294	72.485	0.1
113	-1	7	1	1.30005	72.671	0.2
114	0	2	5	1.29000	73.330	1.3
115	5	1	3	1.28844	73.433	1.8
116	-2	6	3	1.28559	73.622	2.1
117	1	7	1	1.28031	73.976	0.6
118	7	3	0	1.27847	74.101	0.6
119	6	2	2	1.27636	74.244	2.2
120	0	6	3	1.27346	74.441	2.7
121	-1	5	4	1.27085	74.620	1.1
122	-1	3	5	1.26572	74.975	0.1
123	-7	3	3	1.26386	75.104	0.2
124	-3	5	4	1.25854	75.477	0.4
125	6	4	1	1.25642	75.627	1.7
126	4	6	1	1.24950	76.120	1.6
127	-1	7	2	1.24103	76.734	1.5
128	2	4	4	1.23849	76.920	2.0

129	-8	2	2	1.23426	77.232	1.8
130	-8	2	1	1.23029	77.528	1.1
131	4	0	4	1.22918	77.611	1.1
132	8	0	0	1.22828	77.678	1.0
133	-4	6	3	1.21597	78.616	0.1
134	1	7	2	1.20858	79.190	0.4
135	1	5	4	1.20398	79.553	0.2
136	-8	2	3	1.19798	80.032	0.5
137	-6	4	4	1.19470	80.296	1.6
138	4	2	4	1.18860	80.793	1.7
139	2	6	3	1.18588	81.017	1.3
140	-7	3	4	1.17952	81.546	0.1
141	5	5	2	1.17390	82.020	0.3
142	-4	4	5	1.17189	82.191	1.0
143	2	2	5	1.17053	82.307	1.5
144	-2	0	6	1.16824	82.503	1.3
145	0	4	5	1.16313	82.946	1.6
146	0	8	0	1.16100	83.132	1.7
147	-4	0	6	1.15379	83.768	0.2
148	-7	5	1	1.14891	84.205	0.9
149	-6	6	1	1.14762	84.322	0.8
150	-7	5	2	1.14544	84.519	0.8
151	-7	1	5	1.14444	84.610	0.8
152	-1	1	6	1.14239	84.798	0.6
153	0	6	4	1.13837	85.168	1.0

Stick Pattern

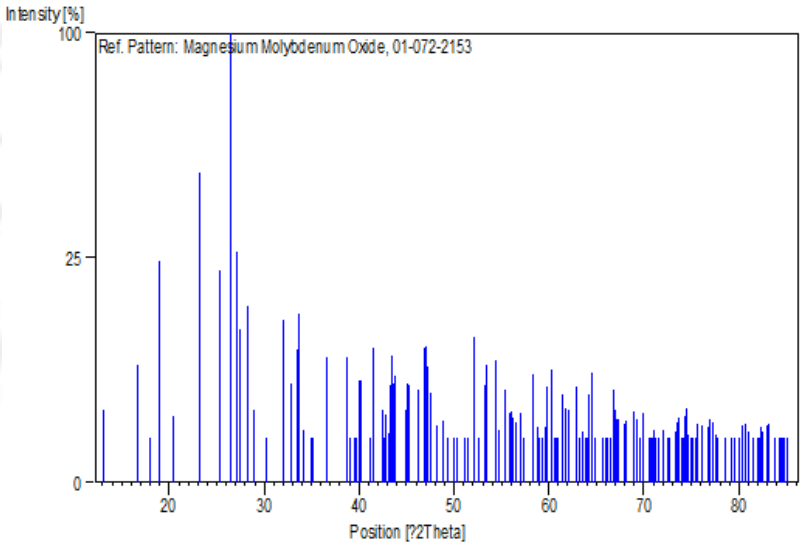

Carbon, JCPDS file number 00-001-0640 [100]

Name and formula

Reference code:	00-001-0640
Mineral name:	Graphite
PDF index name:	Carbon
Empirical formula:	C
Chemical formula:	C

Crystallographic parameters

Crystal system:	Hexagonal		
a:	2.4700	α:	90.0000
b:	2.4700	β:	90.0000
c:	6.8000	γ:	120.0000
Measured density:	2.16	Volume of cell:	35.93
Z:	4.00	RIR:	-

Status, subfiles and quality

Status:	Marked as deleted by ICDD
Subfiles:	Inorganic
	Mineral
Quality:	Blank (B)

Comments

Deleted by:	see SW comments August 31, 1956, 23-64, 25-284
	calc.
Color:	Black
Optical data:	B=1.93-2.07, Sign=-
Additional pattern:	To replace 2-456.

References

Primary reference:	Hanawalt. et al., *Anal. Chem.*, **10**, 475, (1938)
Unit cell:	*Dana's System of Mineralogy, 7th Ed.*

Peak list

No.	h	k	l	d [A]	2Theta[deg]	I [%]
1	0	0	2	3.38000	26.347	100.0
2	1	0	0	2.12000	42.612	5.0
3	1	0	1	2.02000	44.833	10.0
4	0	0	4	1.69000	54.233	10.0
5	1	1	0	1.23000	77.549	18.0
6	1	0	5	1.15000	84.107	9.0
7	0	0	6	1.12000	86.907	1.0
8	2	0	1	1.05000	94.381	1.0
9	1	1	4	0.99000	102.170	3.0
10	1	1	6	0.83000	136.273	1.0
11	2	1	1	0.80000	148.678	1.0
12	3	0	1	0.71000	189.744	1.0

13 1 1 8 0.70000 191.528 1.0

Stick Pattern

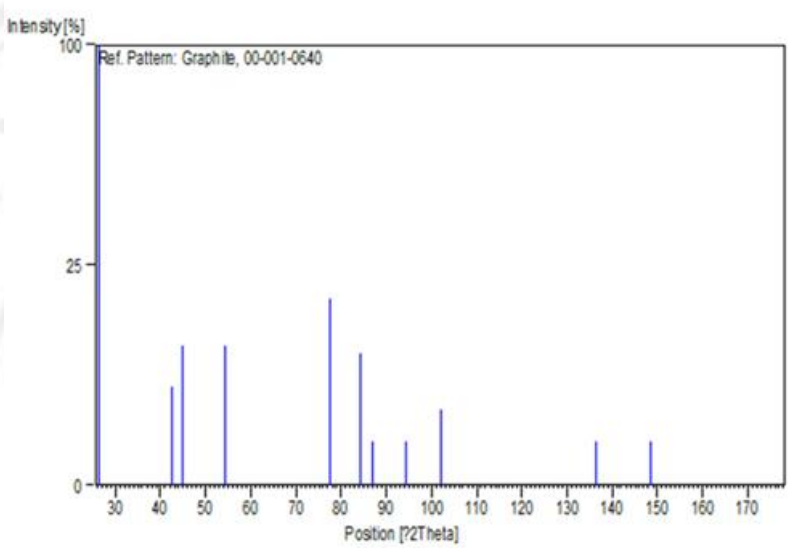

$SrMoO_4$, JCPDS file number 01-085-0586 [128]

Name and formula

Reference code: 01-085-0586

ICSD name: Strontium Molybdenum Oxide

Empirical formula: MoO4Sr

Chemical formula: SrMoO4

Crystallographic parameters

Crystal system: Tetragonal

Space group: I41/a

Space group number: 88

a:	5.3944	α:	90.0000
b:	5.3944	β:	90.0000
c:	12.0200	γ:	90.0000

Calculated density: 4.70 Volume of cell: 349.78

Z: 4.00 RIR: 10.21

Subfiles and Quality

Subfiles: Inorganic, Corrosion, ICSD Pattern

Quality: Calculated (C)

Comments

ICSD collection code: 023700

Test from ICSD: No R value given.

References

Primary reference: *Calculated from ICSD using POWD-12++*, (1997)

Structure: Guermen, E., Daniels, E., King, J.S., *J. Chem. Phys.*, 55, 1093, (1971)

Peak list

No.	h	k	l	d [A]	2Theta[deg]	I [%]
1	1	0	1	4.92150	18.010	2.8
2	1	1	2	3.22053	27.677	100.0
3	0	0	4	3.00500	29.706	13.7
4	2	0	0	2.69720	33.189	18.1
5	2	0	2	2.46075	36.484	0.7
6	2	1	1	2.36528	38.012	2.4
7	1	1	4	2.36049	38.092	3.2
8	1	0	5	2.19582	41.073	0.2
9	2	1	3	2.06673	43.766	0.9
10	2	0	4	2.00724	45.134	25.4
11	2	2	0	1.90721	47.643	9.9

12	2	2	2	1.81787	50.142	0.1
13	1	1	6	1.77360	51.483	13.5
14	1	2	5	1.70286	53.790	0.4
15	3	1	2	1.64104	55.990	20.4
16	1	0	7	1.63624	56.169	11.0
17	2	2	4	1.61027	57.158	9.4
18	0	0	8	1.50250	61.685	1.3
19	3	2	1	1.48468	62.508	0.3
20	3	0	5	1.43990	64.683	0.2
21	2	3	3	1.40161	66.677	0.2
22	1	2	7	1.39796	66.874	0.4
23	4	0	0	1.34860	69.666	2.4
24	4	0	2	1.31588	71.661	0.4
25	2	0	8	1.31258	71.869	5.2
26	1	3	6	1.29879	72.753	9.0
27	1	0	9	1.29641	72.908	4.7
28	3	2	5	1.27023	74.663	0.1
29	3	3	2	1.24394	76.522	3.8
30	4	0	4	1.23038	77.521	3.4
31	4	2	0	1.20622	79.376	3.8
32	2	2	8	1.18025	81.485	2.8
33	3	3	4	1.17097	82.269	0.1
34	2	1	9	1.16845	82.485	0.1
35	1	1	10	1.14643	84.430	2.6
36	3	2	7	1.12803	86.137	0.1
37	2	4	4	1.11941	86.965	4.3

38 2 0 10 1.09791 89.112 0.1

Stick Pattern

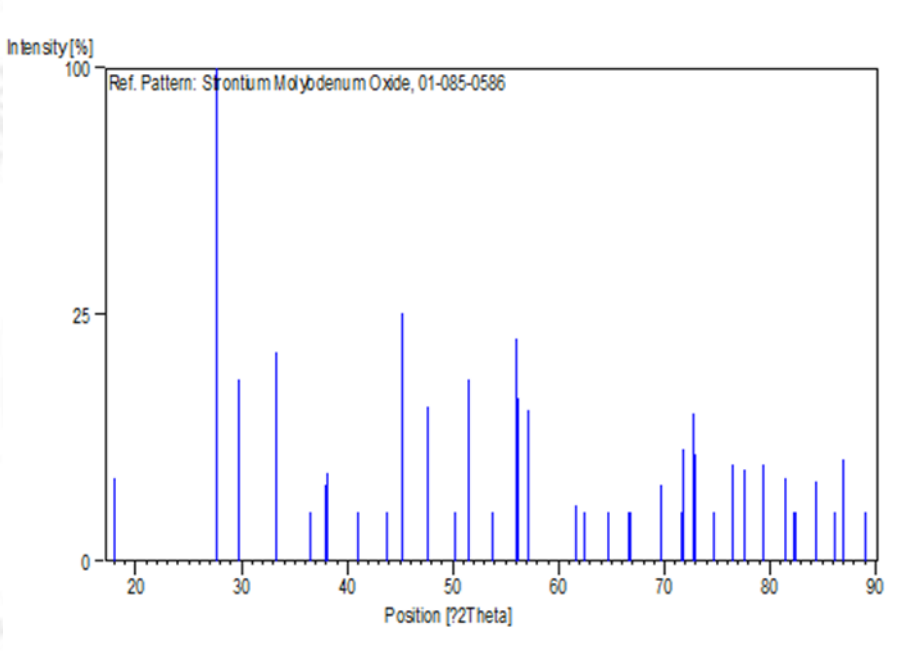

APPENDIX B

Camera constant used for the indexing of SAED pattern

Table appendix B. TEM constant (Lλ) at 200 kV

L (cm)	D111Au (mm)	r111Au (mm)	D111Auv (A)	Lλ (mm.A)
40	8.70	4.35	2.355	10.2442
60	13.2	6.60	2.355	15.5430
80	17.2	8.60	2.355	20.2530
100	21.2	10.60	2.355	24.9630
120	25.2	12.60	2.355	29.6730
150	31.5	15.75	2.355	37.0912
200	41.5	20.75	2.355	48.8662
250	51.8	25.90	2.355	60.9945

CURRICULUM VITAE

Name Miss Surangkana Wannapop

Date of Birth December 9, 1983

Educational Background

2006 – 2009 Master of Science (Materials Science), Chiang Mai University

2002 -2005 Bachelor of education (Physics), Uttaradit Rajabhat University

Scholarship

2009 Strategic Scholarships Fellowships Frontier Research Networks

Experience

2013 Training as a visiting researcher at Georgia Institute of Technology, Atlanta, Georgia, U.S.A. with the research topic as Dye Sensitized Solar Cell achieved by doping Au, $BaTiO_3$ on the surface Rutile TiO_2 Nanorods into Photoanodes. (March 2013- September 2013)

2009 Workshop on Atomic Force Microscope (AFM), August 9-10, Organized by Nanomaterial Research Unit, Faculty of Science, Chiang Mai University, Thailand

2008 TEM Operating (JEOL JEM-2013)

International Publications

[1] **S. Wannapop**, T. Thongtem, S. Thongtem, Characterization of donut-like $SrMoO_4$ produced by microwave-hydrothermal process, Journal of Nanomaterials, 2013 (2013) Art. 474576, 6 pp.

[2] **S. Wannapop**, T. Thongtem, S. Thongtem, Fabrication of $MgMoO_4$–PVA and $MgMoO_4$ fibrous webs via a direct high voltage electrospinning process, Journal of Physics and Chemistry of Solids, 74 (2013) 677-681.

[3] **S. Wannapop**, T. Thongtem, S. Thongtem, Photoemission and energy gap of $MgWO_4$ particles connecting as nanofibers synthesized by electrospinning-calcination combinations, Applied Surface Science, 258 (2012) 4971-4976

[4] **S. Wannapop**, T. Thongtem, S. Thongtem, Characterization of $SrWO_4$-PVA and $SrWO_4$ spiders' webs synthesized by electrospinning, Ceramics Inter-national, 37 (2011) 3499–3507.

[5] T. Thongtem, A. Phuruangrat, **S. Wannapop**, S. Thongtem, Charac-terization of Bi_2S_3 with different morphologies synthesized using microwave radiation, Materials Letters, 64 (2010) 122-124.

[6] S. Thongtem, **S. Wannapop**, A. Phuruangrat, T. Thongtem, Cyclic microwave-assisted spray synthesis of nanostructured $MnWO_4$, Materials Letters, 63 (2009) 833-836.

[7] S. Thongtem, **S. Wannapop**, T. Thongtem, Characterization of $CoWO_4$ nano-particles produced using the spray pyrolysis, Ceramics International, 35 (2009) 2087-2091.

[8] S. Thongtem, **S. Wannapop**, T. Thongtem, Characterization of $MnWO_4$ with flower-like clusters produced using spray pyrolysis, Transactions of Nonferrous Metals Society of China, 19 (2009) s100-s104.

Hindawi Publishing Corporation
Journal of Nanomaterials
Volume 2013, Article ID 474576, 6 pages
http://dx.doi.org/10.1155/2013/474576

Research Article

Characterization of Donut-Like $SrMoO_4$ Produced by Microwave-Hydrothermal Process

Surangkana Wannapop,[1] Titipun Thongtem,[2,3] and Somchai Thongtem[1,3]

[1] *Department of Physics and Materials Science, Faculty of Science, Chiang Mai University, Chiang Mai 50200, Thailand*
[2] *Department of Chemistry, Faculty of Science, Chiang Mai University, Chiang Mai 50200, Thailand*
[3] *Materials Science Research Center, Faculty of Science, Chiang Mai University, Chiang Mai 50200, Thailand*

Correspondence should be addressed to Titipun Thongtem; ttpthongtem@yahoo.com
and Somchai Thongtem; schthongtem@yahoo.com

Received 10 July 2013; Accepted 23 September 2013

Academic Editor: Anukorn Phuruangrat

$SrMoO_4$ hierarchical nanostructures were successfully produced by a one step of 270 W microwave-hydrothermal process of one of the solutions containing three strontium salts [$Sr(NO_3)_2$, $Sr(CH_3CO_2)_2$, and $SrCl_2{\cdot}6H_2O$] and $(NH_4)_6Mo_7O_{24}{\cdot}4H_2O$ for different lengths of time. The as-produced products were characterized by X-ray diffraction, electron microscopy, and spectroscopy. In this research, they were primitive tetragonal structured donut-like $SrMoO_4$, with the main 881 cm^{-1} $\nu_1(A_g)$ symmetric stretching vibration mode of $[MoO_4]^{2-}$ units and 3.92 eV energy gap.

1. Introduction

Alkaline earth scheelite structured molybdate has been very attractive material for a wide variety of applications such as scintillating materials, laser-host materials, cryogenic detectors, heterogeneous catalysts, photoluminescence, optical fibers, solid-state optical masers, and electrochromic materials [1, 2]. One of them is $SrMoO_4$ which is very attractive for using as optoelectronic and electrochromic materials. It was produced by different methods: irregular aggregates of particles and microdisks by an electrochemical process [1], films of micrograins by a nonreversible galvanic cell method [2], hierarchical crystallites by simple precipitation [3], round nanoparticles with uniform sizes by coprecipitation at room temperature [4], spheres and dumbbells by simple aqueous mineralization [5], nanocrystals by microwave-assisted synthesis [6], nanostructured material by solvothermal-mediated microemulsion [7], and powders by coprecipitation and microwave-hydrothermal combination [8].

In this research, hierarchical nanostructures of $SrMoO_4$ with donut shape were produced by microwave-hydrothermal method for different lengths of time without using surfactants, complexing agents, and other additives. The process is very simple, attractive, and novel for large scale synthesis.

2. Experimental Procedures

To produce donut-like $SrMoO_4$, 5 mmol each of strontium salts [A = $Sr(NO_3)_2$, B = $Sr(CH_3CO_2)_2$, and C = $SrCl_2{\cdot}6H_2O$] and 5 mmol ammonium molybdate tetrahydrate [$(NH_4)_6Mo_7O_{24}{\cdot}4H_2O$] were separately dissolved in 25 mL distilled water to form strontium and molybdenum solutions, which were mixed, stirred for 10 min at room temperature, and processed by a 270 W microwave-hydrothermal method for 5, 15, 30, and 90 min (encoded as 1, 2, 3, and 4 in sequence) to form precipitates. In this research, the products were encoded as A1, A2, A3, A4, B1, B2, B3, C1, C2, and C3. The A2 product implied that it was produced from $Sr(NO_3)_2$ + $(NH_4)_6Mo_7O_{24}{\cdot}4H_2O$ for 15 min, the C3 product from $SrCl_2{\cdot}6H_2O$ + $(NH_4)_6Mo_7O_{24}{\cdot}4H_2O$ for 30 min, and similarly for other products.

The products were characterized by an X-ray diffractometer (XRD, SIEMENS D500) operating at 20 kV and 15 mA

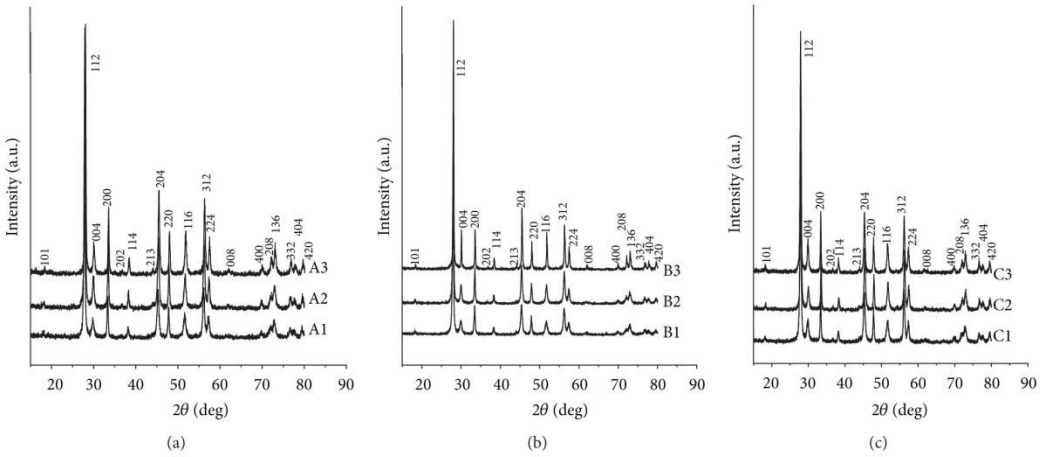

FIGURE 1: XRD patterns of (a) A1, A2, and A3; (b) B1, B2, and B3; and (c) C1, C2, and C3.

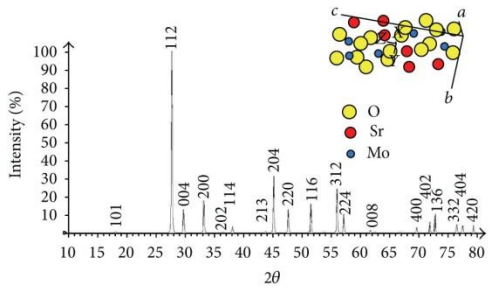

FIGURE 2: Simulated XRD pattern and crystal structure of $SrMoO_4$.

to create Cu-K_α line for the analysis; a scanning electron microscope (SEM, JEOL JSM-6335F) operating at 15 kV; a transmission electron microscope (TEM, JEOL JEM-2010), high resolution transmission electron microscope (HRTEM), and selected area electron diffractometer (SAED) operating at 200 kV; a Raman spectrometer (HORIBA Jobin Yvon T64000) using a 50 mW and 514.5 nm wavelength Ar green laser; and a UV-visible spectrometer (PerkinElmer Lambda 25) using a UV lamp with the resolution of 1 nm.

3. Results and Discussion

Comparing XRD patterns (Figure 1) to the JCPDS no. 85-0586 [9], they were specified as primitive tetragonal scheelite structured $SrMoO_4$ [1–3, 5]. No other characteristic peaks of impurities were detected. The Sr^{2+} cations were mixed with $[Mo_7O_{24}]^{6-}$ anions to form intermediate complexes at room temperature. Upon processing the complexes by the microwave-hydrothermal combination, they were gradually transformed for a few steps into $SrMoO_4$ precipitates. The XRD peaks became sharpened with the increase in the length of time, including the crystalline degree being much improved and the crystals being enlarged. The longer processing time was used, the larger crystallite size and the better crystalline degree would be. Calculated crystallite sizes of the A3, B3, and C3 products [10] were 34.7, 64.7, and 83.2 nm, respectively. They seemed to be influenced by different intermediates, which led to form crystals with different sizes.

XRD peaks of the purified $SrMoO_4$ produced in the solution containing $Sr(NO_3)_2$ and $(NH_4)_6Mo_7O_{24}{\cdot}4H_2O$ by the microwave-hydrothermal reaction for 30 min were compared with that obtained by simulation [11] (Figure 2). The 2θ Bragg angles and peak intensities obtained from the experiment, simulation, and JCPDS database were in good accordance. Crystal growth rates along the x-, y-, and z-directions could be different. The simulated scheelite-type tetragonal structured $SrMoO_4$ (Figure 2) belongs to $I4_1/a$ space group with two $SrMoO_4$ formula units with inversion centers per primitive unit cell. The Sr and Mo sites have S_4 point symmetry. The O sites have only a little symmetry and reside as almost tetrahedral coordination surrounding each of the Mo sites, composing as $[MoO_4]^{2-}$ tetrahedral configuration. Each Sr atom shares corners with eight adjacent O atoms of $[MoO_4]^{2-}$ tetrahedrons. $Sr^{\alpha+}$ cations form bond with $[MoO_4]^{\alpha-}$ anions to produce $SrMoO_4$ crystal structure with $\alpha \rightarrow 2$, including the $[MoO_4]^{2-}$ units with strong Mo–O covalent bonds [4, 5, 8].

SEM images (Figure 3) show some examples of the hierarchical architectures of $SrMoO_4$ produced using different strontium salts and $(NH_4)_6Mo_7O_{24}{\cdot}4H_2O$ by microwave-hydrothermal reactions for different lengths of time. The hierarchical architectures with donut-like or flower-like shape were composed of a number of $SrMoO_4$ nanosheets with 2-3 nm thickness for the products produced using $Sr(NO_3)_2$ or $SrCl_2{\cdot}6H_2O$ and $(NH_4)_6Mo_7O_{24}{\cdot}4H_2O$, and of $SrMoO_4$

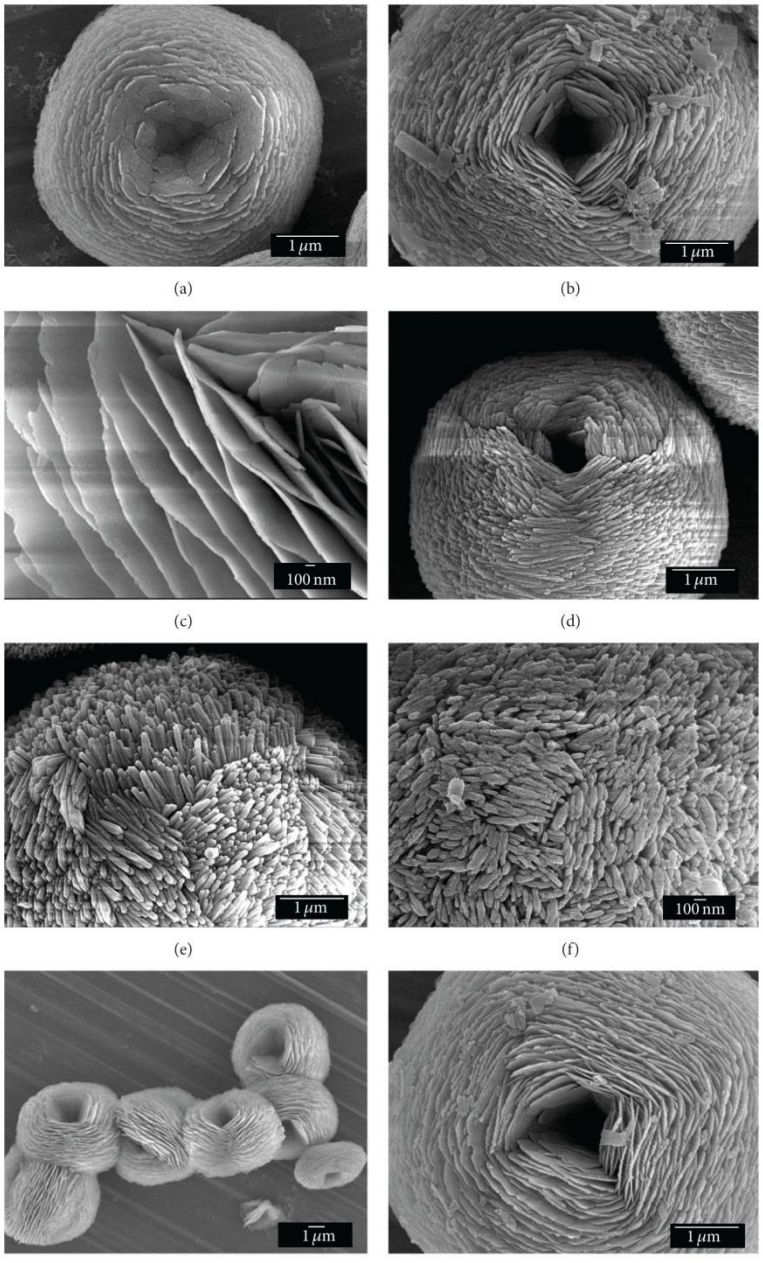

FIGURE 3: Donut-like $SrMoO_4$ colonies of the (a–h) A1, A3, A4, B1, B2, B3, C1, and C3 products, respectively.

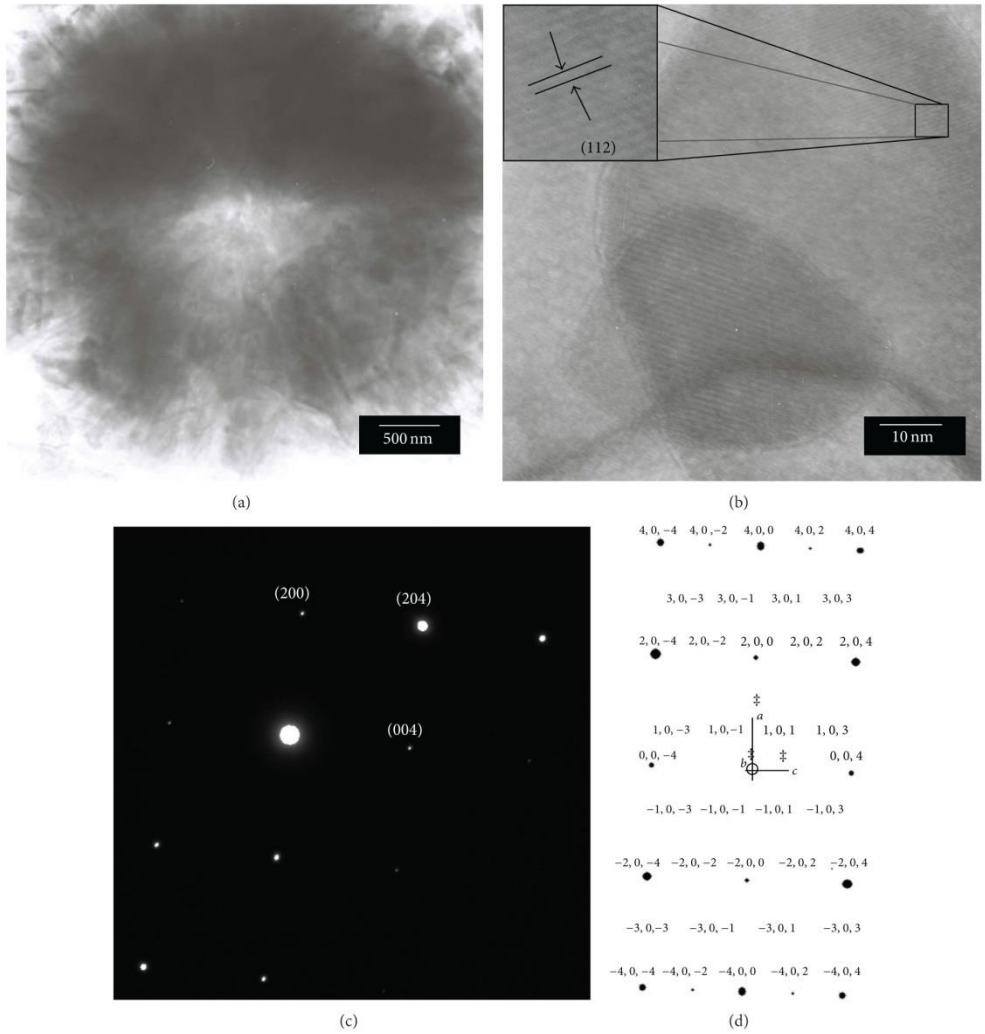

Figure 4: (a, b) TEM and HRTEM images and (c, d) SAED and simulated patterns of the A3 product.

nanorods with 100–150 nm length for the product produced using $Sr(CH_3CO_2)_2$ and $(NH_4)_6Mo_7O_{24}{\cdot}4H_2O$. Different morphologies seemed to be obtained from different intermediate complexes, influenced by different anions of Sr salts. They were continuously enlarged and densely populated and their sizes were increased with the increase in the processing time. At these stages, the nanosheets and nanorods were squeezed and their shapes lack symmetry, due to the stress developed inside.

The donut-like product was confirmed by the TEM image (Figures 4(a) and 4(b)) of the A3 product, appeared as dark spherical area around the middle white one. A number of the (112) planes with 0.322 nm apart were detected. An ED pattern (Figure 4(c)) with electron beam in the [0 − 1 0] direction belongs to the $SrMoO_4$ crystalline nanosheet. This interpreted pattern was in good accordance with the simulated one (Figure 4(d)), although some spots of the simulated pattern did not appear on the interpreted one. To simulate the pattern, intensity and size of the spots (planes) were mutually related. The stronger intensity was used, the larger size was achieved. The intensity and size of the spots were limited by a saturated intensity used for simulation. Thus the spots of the simulated pattern with low intensity were absent from the interpreted one.

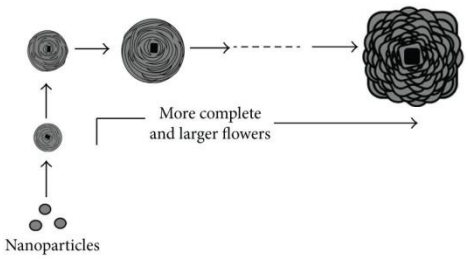

FIGURE 5: Schematic illustration for the formation of hierarchical architecture of $SrMoO_4$.

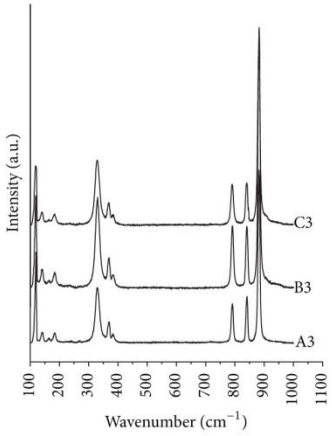

FIGURE 6: Raman spectra of the A3, B3, and C3 products.

When Sr and Mo solutions were mixed, the intermediate complexes formed. Subsequently, they were processed by the microwave-hydrothermal reaction and gradually transformed for a few steps into hierarchical nanostructures of $SrMoO_4$ with donut-like or flower-like shape:

$$Sr^{2+} + (Mo_7O_{24})^{6-} \longrightarrow \text{intermediate complexes}$$
$$\longrightarrow SrMoO_4 \text{ (molecules)}$$

$SrMoO_4$ molecules nucleated and grew to form nanoparticles. Furthermore, these nanoparticles selectively grew to form nanosheet petals for the A1 to A4 and C1 to C3 products and nanorod petals for the B1 to B3 products on top. As the processing time passed, the petals were enlarged and squeezed each other. Some petals were bent and some were broken to release stress energy. The flowers (donuts) became more complete as well. In the end, the particles became completely donut-like shape (Figure 5).

Several different vibrations were detected on Raman spectra of the $SrMoO_4$ crystals (Figure 6). The Raman peaks at 881 cm^{-1} were specified as the $\nu_1(A_g)$ symmetric stretching vibration mode of $[MoO_4]^{2-}$ units. Those at 838–841 and 788–790 cm^{-1} corresponded to the $\nu_3(B_g)$ and $\nu_3(E_g)$ antisymmetric stretching vibration modes, respectively. The peaks at 368 and 328–330 cm^{-1}, respectively, corresponded to the $\nu_4(B_g)$ antisymmetric and $\nu_2(A_g)$ symmetric bending modes, including the 181–183 cm^{-1} to the $\nu_{f.r.}(F_1)$ free rotation modes. Those at 118, 141, and 163 cm^{-1} were specified as the external vibration modes of Sr^{2+} cations and $[MoO_4]^{2-}$ units. These vibration modes were very close to those reported by other researchers [3, 5, 8] and provided the evidence of scheelite structure.

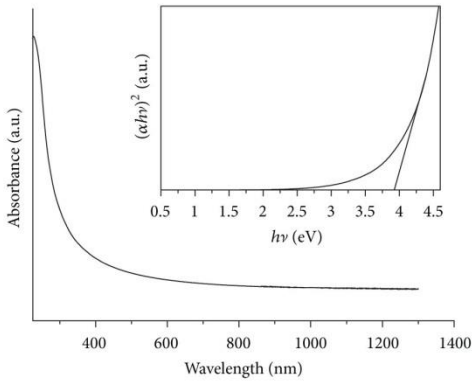

FIGURE 7: UV-visible absorption and the $(\alpha h\nu)^2$ versus $h\nu$ plot of the C3 product.

UV-visible absorption (Figure 7) of the hierarchical $SrMoO_4$ architecture of the C3 product synthesized by the 270 W and 30 min microwave-hydrothermal process indicated an exponential decreasing of the UV-visible energy attenuated through the crystalline C3 product. During attenuation, the absorption was controlled by two photon energy ($h\nu$) ranges. For $h\nu < E_g$, the absorption was linearly increased with the increasing of photon energy. The steep inclination of the linear portion of the curve was caused by the UV absorption for charged transition from the topmost occupied state of valence band to the bottommost unoccupied state of the conduction band. For $h\nu < E_g$, the absorption curve became different from linearity, caused by the UV absorption for charged transition relating to defects. Band gap of the product is related to its absorbance and photonic energy. Thus the combination of absorbance and photonic energy was used to determine the photonic band gap. By extrapolating the linear portion curve (tail of the curve) of the $(\alpha h\nu)^2$ versus $h\nu$ plot to zero absorption, its direct energy gap was determined to be 3.92 eV for the hierarchical architecture of the C3 product. This energy gap was very close to the 3.98 eV of $SrMoO_4$ powder processed by the microwave-hydrothermal reaction at 413 K for 5 h reported by Sczancoski et al. [8].

4. Conclusions

$SrMoO_4$ hierarchical nanostructures were successfully produced by the one-step microwave-hydrothermal process. In

this research, the products were tetragonal scheelite crystal with donut-like or flower-like $SrMoO_4$. Their main vibration modes were detected at 881 cm^{-1} and the energy gap of 3.92 eV.

Acknowledgments

The authors wish to thank the Thailand's Office of the Higher Education Commission for providing financial support through the National Research University (NRU) Project and the Strategic Scholarships for Frontier Research Network of the Joint Ph.D. Research Program. They also thank the National Nanotechnology Center (NANOTEC), National Science and Technology Development Agency, for providing financial support through the project P-10-11345, including the Graduate School of Chiang Mai University through a general support.

References

[1] Y. Sun, J. Ma, J. Fang, C. Gao, and Z. Liu, "Photoluminescent improvement of $SrMoO_4$ by the electrochemical formation of Ca^{2+}-doped solid solutions," *Inorganic Chemistry Communications*, vol. 14, no. 8, pp. 1221–1223, 2011.

[2] J. Bi, C.-H. Cui, X. Lai, F. Shi, and D.-J. Gao, "Synthesis of luminescent $SrMoO_4$ thin films by a non-reversible galvanic cell method," *Materials Research Bulletin*, vol. 43, no. 3, pp. 743–747, 2008.

[3] G. Xing, Y. Li, Y. Li et al., "Morphology-controllable synthesis of $SrMoO_4$ hierarchical crystallites via a simple precipitation method," *Materials Chemistry and Physics*, vol. 127, no. 3, pp. 465–470, 2011.

[4] T. Thongtem, S. Kungwankunakorn, B. Kuntalue, A. Phuruangrat, and S. Thongtem, "Luminescence and absorbance of highly crystalline $CaMoO_4$, $SrMoO_4$, $CaWO_4$ and $SrWO_4$ nanoparticles synthesized by co-precipitation method at room temperature," *Journal of Alloys and Compounds*, vol. 506, no. 1, pp. 475–481, 2010.

[5] D. Chen, K. Tang, F. Li, and H. Zheng, "A simple aqueous mineralization process to synthesize tetragonal molybdate microcrystallites," *Crystal Growth and Design*, vol. 6, no. 1, pp. 247–252, 2006.

[6] T. Thongtem, A. Phuruangrat, and S. Thongtem, "Microwave-assisted synthesis and characterization of $SrMoO_4$ and $SrWO_4$ nanocrystals," *Journal of Nanoparticle Research*, vol. 12, no. 6, pp. 2287–2294, 2010.

[7] L. Sun, Q. Guo, X. Wu et al., "Synthesis and photoluminescent properties of strontium tungstate nanostructures," *Journal of Physical Chemistry C*, vol. 111, no. 2, pp. 532–537, 2007.

[8] J. C. Sczancoski, L. S. Cavalcante, M. R. Joya, J. A. Varela, P. S. Pizani, and E. Longo, "$SrMoO_4$ powders processed in microwave-hydrothermal: synthesis, characterization and optical properties," *Chemical Engineering Journal*, vol. 140, no. 1–3, pp. 632–637, 2008.

[9] "Powder Diffraction File," JCPDS-ICDD, 12 Campus Boulevard, Newtown Square, PA 19073-3273, U.S.A., 2001.

[10] C. Suryanarayana and M. G. Norton, *X-Ray Diffraction: A Practical Approach*, Plenum Press, New York, NY, USA, 1998.

[11] C. Boudias and D. Monceau, "CaRIne Crystallography 3.1," DIVERGENT S.A., Centre de Transfert, 60200 Compiègne, France, 1989–1998.

Journal of Physics and Chemistry of Solids 74 (2013) 677–681

Contents lists available at SciVerse ScienceDirect

Journal of Physics and Chemistry of Solids

journal homepage: www.elsevier.com/locate/jpcs

Fabrication of $MgMoO_4$–PVA and $MgMoO_4$ fibrous webs via a direct high voltage electrospinning process

Surangkana Wannapop [a], Titipun Thongtem [b,c,*], Somchai Thongtem [a,c]

[a] Department of Physics and Materials Science, Faculty of Science, Chiang Mai University, Chiang Mai 50200, Thailand
[b] Department of Chemistry, Faculty of Science, Chiang Mai University, Chiang Mai 50200, Thailand
[c] Materials Science Research Center, Faculty of Science, Chiang Mai University, Chiang Mai 50200, Thailand

ARTICLE INFO

Article history:
Received 9 December 2011
Accepted 6 January 2013
Available online 16 January 2013

Keywords:
A. Nanostructures
C. Electron microscopy
C. Infrared spectroscopy
C. Raman spectroscopy
C. X-ray diffraction

ABSTRACT

Mixtures of $(CH_3COO)_2Mg \cdot 4H_2O$ and $(NH_4)_6Mo_7O_{24} \cdot 4H_2O$ containing 0.7, 1.0 and 1.3 g of poly(vinyl alcohol) (PVA, 125,000 MW) were electrospun by +15 kV direct voltage to form fibrous webs. In the present research, the fibrous web of the 1.3 g PVA was characterized by a thermogravimetric analyser (TGA), and calcined at 400–600 °C for 3 h. $MgMoO_4$ contained in the fibrous webs was characterized by X-ray diffraction (XRD), morphologies of the webs by scanning and transmission electron microscopy (SEM, TEM) and atomic force microscopy (AFM), and their vibration modes by Fourier transform infrared (FTIR) and Raman spectrometry. The 5.15 eV direct energy gap, caused by the electronic transition in the $(MoO_4)^{2-}$ complex, was determined by UV–visible absorption. Formation mechanism of the fibrous webs was also proposed according to the experimental results.

1. Introduction

Recently, a considerable attention has been paid on $AMoO_4$ (A=Mg, Mn, Fe, Co, Ni, and Zn) which have two main structural types: α and β, with $(MoO_4)^{2-}$ complex as prime constituents [1–3]. Among them, $MgMoO_4$ is able to be used for a variety of applications: light emitting diodes [1], scintillation bolometers [4], and catalytic precursors [5,6].

In the present research, $MgMoO_4$–PVA electrospun fibers were firstly produced by a lab-made electrospinning equipment. They were subsequently calcined at high temperature to form $MgMoO_4$ nanofibers. To the best of our knowledge, there are no $MgMoO_4$ nanofibers ever been produced by the present process. It is therefore for us to use the mixture of inorganic and organic materials to produce the inorganic material–polymer electrospun fibers, which would be transformed into nanofibrous inorganic material by subsequent calcination at high temperature. The success in producing the solid nanofibrous material may lead to new industrial process by a direct high voltage electrospinning process.

2. Experiment

$(CH_3COO)_2Mg \cdot 4H_2O$ and $(NH_4)_6Mo_7O_{24} \cdot 4H_2O$ each 4.5 mmol was dissolved in 30 ml deionized water, which was subsequently divided into three solutions with equal volume. Then 0.7, 1.0 and 1.3 g of PVA (125,000 MW) were added to form M1, M2, and M3 mixtures. Each was electrospun through a horizontal plastic syringe, biased with +15 kV direct voltage, to form a fibrous web on a ground flat aluminum foil, placed 15 cm apart. The webs produced from the M3 mixture were also calcined at 400, 500 and 600 °C, held at each of these temperatures for 3 h, and cooled down to room temperature. All the final webs were further characterized using different methods.

3. Results and discussion

3.1. TGA and XRD

The weight loss of PVA (Fig. 1a) exhibited the degradation process for three steps: 10.5 wt% due to the evaporation of loosely bound water at 32–200 °C, 79.3 wt% predominantly caused by the decomposition of PVA structure at 200–420 °C, and 8.3 wt% by the breaking of PVA backbone at 420–490 °C. Its weight tended to be constant upon further heating above 490 °C [7]. For the M3 as-spun fibrous web, it weight loss (Fig. 1a) was 33.5 wt% associated with water evaporation at 32–226 °C, 41.2 wt% caused by the decomposition of PVA at 226–420 °C, and 7.7 wt% seemed to be the oxidation and decomposition of the PVA main chain at 420–519 °C. These last two steps were attributed to the loss of

* Corresponding author at: Department of Chemistry, Chiang Mai University, 239 Huay Kaew Road, Muang, Chiang Mai 50200, Thailand.
Tel.: +66 053 943344; fax: +66 053 892277.
E-mail addresses: ttpthongtem@yahoo.com, ttpthongtem@gmail.com (T. Thongtem).

0022-3697/$ - see front matter © 2013 Elsevier Ltd. All rights reserved.
http://dx.doi.org/10.1016/j.jpcs.2013.01.002

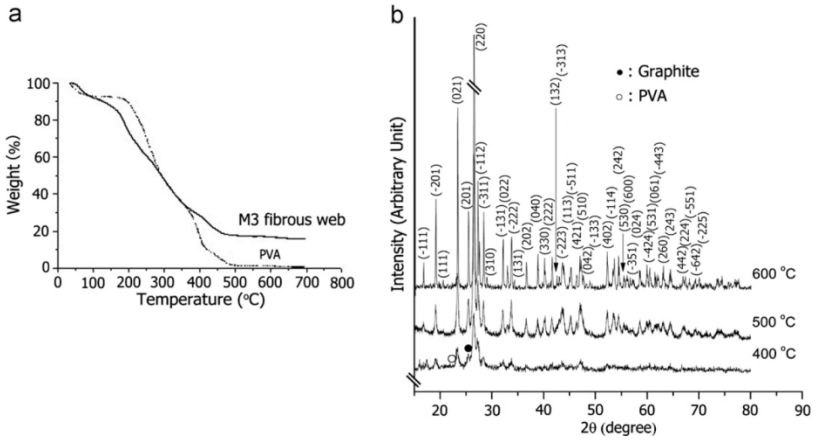

Fig. 1. (a) TGA curves of PVA and the M3 as-spun fibrous web, and (b) XRD spectra of the M3 fibrous webs with 400–600 °C and 3 h calcination.

PVA and organic compound blended in the fibrous web. Above 519 °C, there was no significant change in its weight.

XRD spectra (Fig. 1b) of the M3 fibrous webs after calcination at 400, 500 and 600 °C for 3 h corresponded to the monoclinic structured $MgMoO_4$ and C2/m space group (JCPDS database no. 72-2153) [8]. The temperatures played a role in the crystalline degree and purity of the $MgMoO_4$ fibrous webs. At 400 °C, the fibrous web was not perfectly pure $MgMoO_4$, containing some residual PVA at 2θ of approximately 22.5° [9], and graphite (JCPDS database no. 01-0640) at 2θ=26.3° of the (002) crystallographic plane [8]. Upon increasing the calcination temperatures to 500 and 600 °C, the spectra became sharper and the XRD intensities were stronger. The crystalline degree of the fibrous webs was considerably improved. No PVA and graphite were detected. At 600 °C calcination, the fibrous web was the best pure crystal. Its crystalline degree was the highest, and the atoms resided in the perfect crystal lattice. By using the Scherrer formula [10], crystallite sizes of the M3 fibrous webs after 400, 500 and 600 °C calcination for 3 h were 23.1, 25.9, and 52.0 nm, respectively.

3.2. SEM, TEM, HRTEM, and AFM

SEM images (Fig. 2a–c) of the as-spun products of the M1, M2, and M3 mixtures were composed of fibers and electrospun like spiders' webs with smooth surfaces. Some beads were also detected on the M1 and M2 fibrous webs, controlled by viscosity and density of the mixtures. When the content of PVA was as high as 1.3 g, the beads were no longer detected. It was exactly right to eject the mixture with sufficiently high viscosity and density out of the hollow needle to form the bead-free web. In the present research, the $MgMoO_4$ nuclei blended in the fibrous webs were invisible. When the M3 fibrous webs were calcined at 400, 500 and 600 °C for 3 h, the fibers were thinned—caused by the evaporation of PVA and volatile components. The $MgMoO_4$ nuclei also grew up to be nanoparticles. At 400 °C and 3 h calcination, the fibrous surface (Fig. 2d) was smooth, showing that some PVA coating remained on the surface. Upon increasing the calcination temperatures from 400 °C to 500 °C (Figs. 2e and 3a) and 600 °C (Figs. 2f and 3c), their surfaces became roughened. At 600 °C and 3 h calcination, the fibers were of 50–100 nm diameters, and were composed of 20–50 nm nanoparticles. External surfaces of the M3 fibers were also characterized by AFM (Fig. 4). Before and after 600 °C and 3 h calcination, their high profiles (rms) were 1.12 nm and 4.36 nm, respectively. A number of the (021) and (−111) crystallographic planes of typical nanoparticles (Fig. 3b and d) with 500 °C and 600 °C calcination for 3 h were detected by HRTEM–revealing the presence of $MgMoO_4$ contained in the fibrous webs.

3.3. FTIR and Raman analyses

Fig. 5a shows FTIR spectra of PVA and the M3 fibrous webs before and after calcination at 400, 500 and 600 °C for 3 h. Obviously, the major vibrational modes associated with PVA were the following. The O–H stretching of alcohol and residual water was detected at 3600–3200 cm^{-1}. The vibrational mode at 2943 cm^{-1} corresponds to the C–H stretching of alkyl groups. The C=O stretching mode was detected at 1721 cm^{-1}, CH_2 bending mode at 1448 cm^{-1}, and C–O stretching mode of carboxyl at 1098 cm^{-1} [11,12]. When the M3 as-spun fibrous web was characterized by FTIR, additional four asymmetric stretching modes of Mo–O–Mo were detected at 970, 893, 835, and 736 cm^{-1} [5], and bending mode of Mo–O at 427 cm^{-1}. Once, the M3 as-spun fibrous webs were calcined at 400, 500 and 600 °C for 3 h, the PVA evaporated and decomposed. At higher temperatures, the vibrational modes of PVA became weakened, and those of $MgMoO_4$ were stronger until at 500 and 600 °C and 3 h calcination, where the vibrations of PVA were no longer detected. The vibrations of $MgMoO_4$ were the strongest at 600 °C and 3 h calcination.

Raman spectrum of the M3 fibrous web with 600 °C and 3 h calcination is shown in Fig. 5b. The strong peaks at 962 and 949 cm^{-1} were assigned to the $\nu_1(A_g)$ symmetric stretching modes. Those at 904, 870, and 848 cm^{-1} belonged to the ν_3 (A_g/B_g) modes, which were similar to the two split triply degenerate ν_3 modes. The splitting could be as large as 150 cm^{-1}. Comparing the ν_1 and ν_3 vibration modes, the first have stronger intensities and higher frequencies (wavenumbers) than those of the second. The Raman shifts at 423, 386, 370, 335 and 279 cm^{-1} were unable to be specifically identified among the two ν_2 and ν_4 bending and lattice vibration modes equal in intensities, due to the strong interaction between the tetrahedrons and the coupling with the Mg–O stretching modes. The remaining ones at 205, 177, and 156 cm^{-1} corresponded to the lattice vibrations of A_g/B_g modes [3].

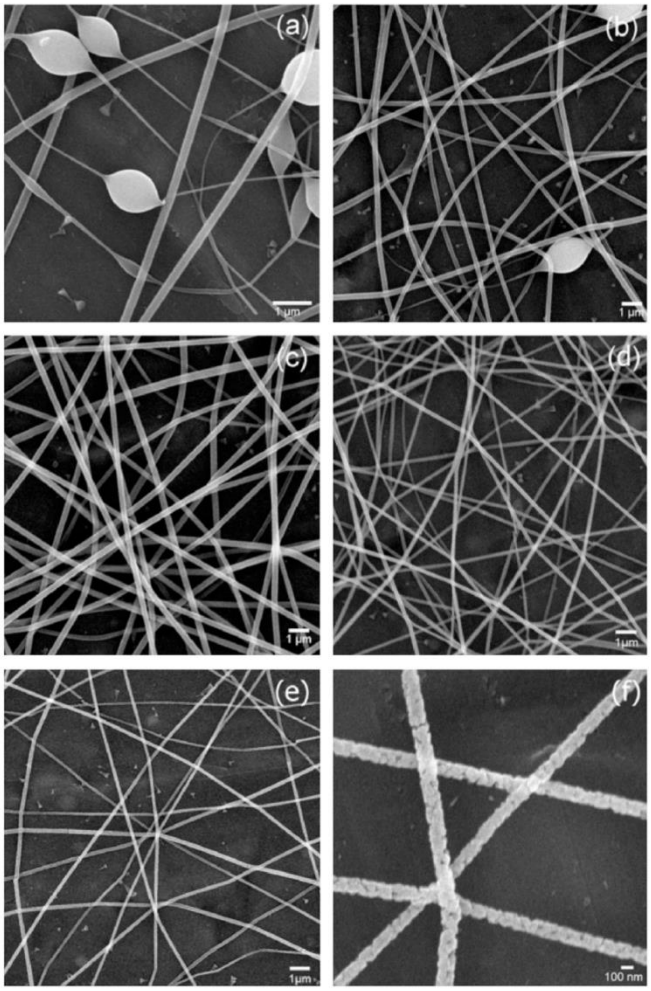

Fig. 2. SEM images of (a)–(c) the as-spun fibrous webs produced from the M1, M2, and M3 mixtures, and (d)–(f) the M3 fibrous webs after 400, 500 and 600 °C calcination for 3 h.

3.4. Formation mechanism

A formation mechanism of $MgMoO_4$ fibrous webs was proposed as follows. Mixtures of $(CH_3COO)_2Mg \cdot 4H_2O$, $(NH_4)_6Mo_7O_{24} \cdot 4H_2O$ and PVA were ejected out of a hollow needle with +15 kV biased voltage, and deposited on ground aluminum foils. During electrospinning, the fibers were heated up by the direct high voltage. $(CH_3COO)_2Mg \cdot 4H_2O$ reacted with $(NH_4)_6Mo_7O_{24} \cdot 4H_2O$ to produce $MgMoO_4$ molecules, which nucleated and blended in the PVA template:

$$7Mg^{2+} + (Mo_7O_{24})^{6-} + 4H_2O \rightarrow 7MgMoO_4 + 8H^+ \quad (1)$$

At this stage, $MgMoO_4$–PVA electrospun products formed and deposited as fibrous webs on the grounded aluminum foils. Upon calcination at 400–600 °C for 3 h, PVA and residual water evaporated and decomposed. $MgMoO_4$ nuclei in the PVA template grew to form nanoparticles. The rates of evaporation and decomposition increased with the increasing in the calcination temperatures. At 600 °C and 3 h calcination, PVA and water were no longer detected. A number of the nanoparticles with the highest crystalline degree joined together and a fibrous web was produced.

3.5. UV–visible absorption

UV–visible absorption of the M3 fibrous web with 600 °C and 3 h calcination is shown in Fig. 5c. For photon energy ($h\nu$) greater than energy gap (E_g), the relationship between the square absorbance and the $h\nu$ for direct interband transitions was linearly increased with the increasing of $h\nu$ [13]. Its direct energy gap was 5.15 eV, due to the absorption spectrum in the vicinity of the fundamental absorption edge, caused by the electronic transition in the $(MoO_4)^{2-}$ complex. This energy gap is in accordance with that reported by Spasskii et al. [4]. Particle sizes

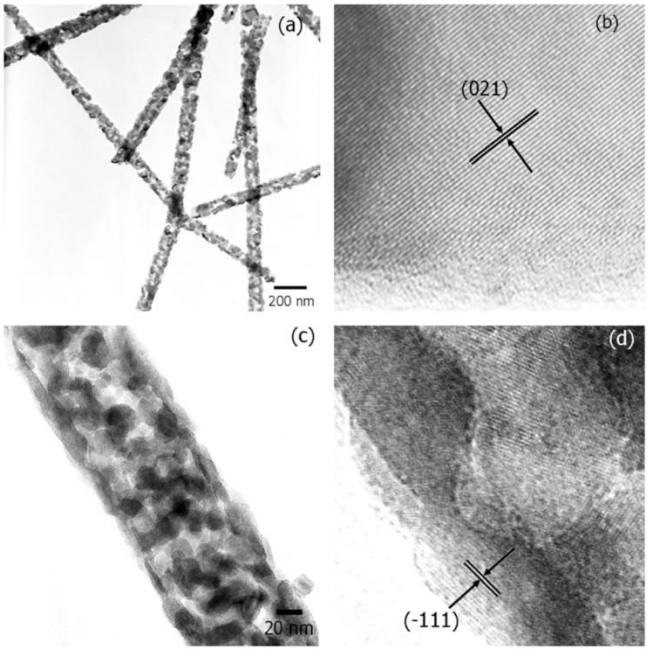

Fig. 3. TEM and HRTEM images of the M3 fibrous webs after calcination at (a, b) 500 °C, and (c, d) 600 °C for 3 h.

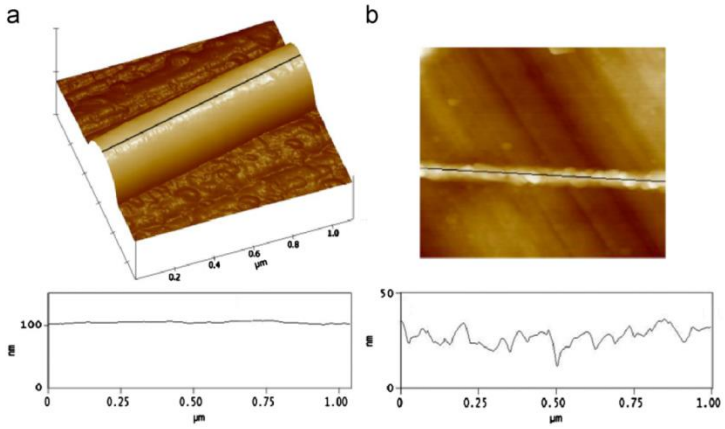

Fig. 4. AFM images and height profiles of the M3 fibers (a) before and (b) after calcination at 600 °C for 3 h.

and morphologies were found to play a role in the absorbance characteristics [14], which have an influence on the energy gap as well.

4. Conclusions

$(CH_3COO)_2Mg \cdot 4H_2O$ and $(NH_4)_6Mo_7O_{24} \cdot 4H_2O$ mixtures containing different contents of PVA were electrospun by a direct high voltage to form fibrous webs of $MgMoO_4$–PVA, which was followed by high temperature calcination to form fibrous web of $MgMoO_4$ nanoparticles. Weight loss of the M3 $MgMoO_4$–PVA fibrous web tended to terminate at 519 °C and above. At 600 °C and 3 h calcination, the web was the best pure $MgMoO_4$ crystals, with 50–100 nm fibrous diameters and 20–50 nm particle sizes. FTIR asymmetric stretching modes of Mo–O–Mo were detected at 970, 893, 835, and 736 cm^{-1}, and two strong $\nu_1(A_g)$ Raman symmetric stretching modes at 962 and 949 cm^{-1}. The direct E_g of the M3 $MgMoO_4$ fibrous web was determined to be 5.15 eV—a promising material for a variety of applications.

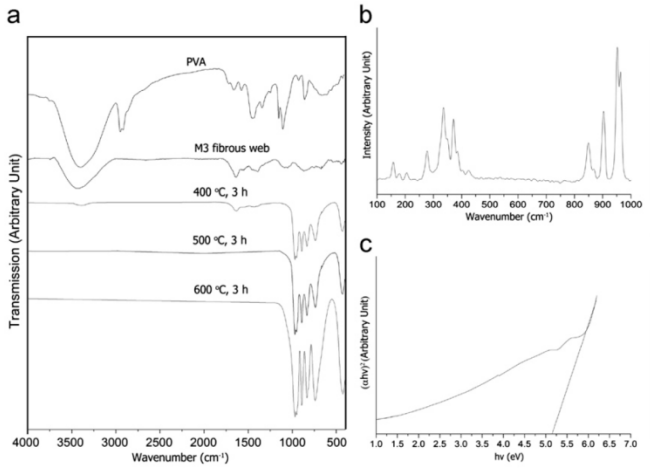

Fig. 5. (a) FTIR spectra of PVA and the M3 fibrous webs before and after calcination at 400, 500 and 600 °C for 3 h. (b) Raman spectrum and (c) UV–visible absorption of the M3 fibrous web after calcination at 600 °C for 3 h.

Acknowledgments

We wish to thank the National Nanotechnology Center (NANOTEC), National Science and Technology Development Agency, Thailand, for financial support through the Project code P-10-11345, the Thailand's Office of the Higher Education Commission through the National Research University Project, and the Strategic Scholarships for Frontier Research Network of the Joint Ph.D. Research Program, and the Graduate School of Chiang Mai University through a general support.

References

[1] L.Y. Zhou, J.S. Wei, L.H. Yi, F.Z. Gong, J.L. Huang, W. Wang, Mater. Res. Bull. 44 (2009) 1411–1414.
[2] S.F. Matar, A. Largeteau, G. Demazeau, Solid State Sci. 12 (2010) 1779–1785.
[3] P.J. Miller, Spectrochim. Acta 27 A (1971) 957–960.
[4] D.A. Spasskii, V.N. Kolobanov, V.V. Mikhaĭlin, L.Y. Berezovskaya, L.I. Ivleva, I.S. Voronina, Opt. Spectros 106 (2009) 556–563.
[5] Y.S. Yoon, K. Suzuki, T. Hayakawa, S. Hamakawa, T. Shishido, K. Takehira, Catal. Lett. 59 (1999) 165–172.
[6] Z. Shang, S. Huang, X. Xu, J. Chen, Mater. Chem. Phys. 114 (2009) 173–178.
[7] E.A. El-hefian, M.M. Nasef, A.H. Yahaya, E-J. Chem 7 (2010) 1212–1219.
[8] Powder Diffract. File, JCPDS-ICDD, 12 Campus Boulevard, Newtown Square, PA 19073-3273, USA, 2001.
[9] K. Pal, A.K. Banthia, D.K. Majumdar, AAPS PharmSciTech (2007), http://dx.doi.org/10.1208/pt080121, Art. No. 21.
[10] E.A. Souza, J.G.S. Duque, L. Kubota, C.T. Meneses, J. Phys. Chem. Solids 68 (2007) 594–599.
[11] H.S. Mansur, R.L. Oréfice, A.A.P. Mansur, Polymer 45 (2004) 7193–7202.
[12] H.S. Mansur, C.M. Sadahira, A.N. Souza, A.A.P. Mansur, Mater. Sci. Eng. C 28 (2008) 539–548.
[13] O. Yayapao, T. Thongtem, A. Phuruangrat, S. Thongtem, J. Alloys Compd 509 (2011) 2294–2299.
[14] M. Hojamberdiev, G. Zhu, Y. Xu, Mater. Res. Bull. 45 (2010) 1934–1940.

Applied Surface Science 258 (2012) 4971–4976

Contents lists available at SciVerse ScienceDirect

Applied Surface Science

journal homepage: www.elsevier.com/locate/apsusc

Photoemission and energy gap of $MgWO_4$ particles connecting as nanofibers synthesized by electrospinning–calcination combinations

Surangkana Wannapop[a], Titipun Thongtem[b,c,*], Somchai Thongtem[a,c,**]

[a] Department of Physics and Materials Science, Faculty of Science, Chiang Mai University, Chiang Mai 50200, Thailand
[b] Department of Chemistry, Faculty of Science, Chiang Mai University, Chiang Mai 50200, Thailand
[c] Materials Science Research Center, Faculty of Science, Chiang Mai University, Chiang Mai 50200, Thailand

ARTICLE INFO

Article history:
Received 4 November 2011
Received in revised form 10 January 2012
Accepted 23 January 2012
Available online 1 February 2012

Keywords:
$MgWO_4$ nanofibers
Electrospinning
Indirect band gap

ABSTRACT

Mixtures of magnesium acetate tetrahydrate ($(CH_3COO)_2Mg{\cdot}4H_2O$), ammonium tungstate tetrahydrate ($(NH_4)_6W_7O_{24}{\cdot}4H_2O$), and poly(vinyl alcohol) with the molecular weight of 72,000 were electrospun through a +15 kV direct voltage to form fibers on ground flat aluminum foils. The electrospun fibers of 1.5, 3.0, and 4.5 mmol of each starting material containing 1.3 g poly(vinyl alcohol) were further calcined at 500–700 °C for 3 h constant length of time. At 500 and 600 °C calcination, both monoclinic and anorthic phases of $MgWO_4$ particles with different sizes connecting as fibrous assemblies were detected. Upon increasing the calcination temperature to 700 °C, only monoclinic phase of facet nanoparticles interconnecting along the fibrous axes with 4.19 eV indirect band gap and 461 nm photoemission was synthesized. In the present research, formation of $MgWO_4$ molecules as well as nucleation and growth of nanoparticles was also proposed.

1. Introduction

Two majorities of AWO_4 (A^{2+} = divalent cations) naturally crystallized on Earth are tetragonal scheelite ($I4_1/a$ space group) with large cationic radii (>0.099 nm: Ba, Ca, Sr, Pb, Eu), and monoclinic wolframite ($P2/c$ space group) with small cationic radii (<0.077 nm: Co, Cd, Fe, Mn, Mg, Ni, Zn). For the first, each W^{6+} ion is surrounded by four O^{2-} ions forming $(WO_4)^{2-}$ tetrahedral unit. But for the second, each W^{6+} ion is surrounded by six O^{2-} ions forming $(WO_6)^{6-}$ octahedral complex [1–6]. $MgWO_4$ is a semiconducting material, containing both light (Mg and O) and heavy (W) elements. It is very interesting for different technological applications: luminescence, scintillation [7,8], tunable microwave applications [9] and tunable solid state lasers [10]. Thus the study of photonic absorption and emission of $MgWO_4$ particles interconnecting as fiber-like assemblies became increasingly attractive for a number of applications.

Basically, electrospinning equipment is composed of three components: a direct current (d.c.) power supply, a long hollow needle and an electrical conducting screen. During electrospinning, a drop of polymeric solution at the tip of the hollow needle is charged by a positive d.c. high voltage. The mutual positive charge repulsion on the polymeric droplet is created. When the applied d.c. voltage is increased, the liquid droplet is stretched to be a conical shape, known as Taylor cone. Upon further increasing the d.c. voltage until it is sufficiently high, the repulsive force overcomes the surface tension of the polymeric liquid, and the jet of liquid is ejected out of the Taylor cone. Meanwhile, the liquid jet evaporates and solidifies, leaving behind the polymeric fibers deposited on the ground conducting screen [11,12].

There are several parameters playing the role in electrospun fibers: (a) variable parameters of electrospinning equipment (applied voltage at the needle tips as well as electric field inside fibers, pressure used to push the liquid out of the hollow needles, and a distance between the needle tip and ground conducting screen), (b) solution properties (viscosity, surface tension, elasticity and conductivity) and (c) ambient parameters (temperature, humidity and wind blow). These can play the role in the surface morphologies of electrospun fibers, fibrous diameter, number of beads including their shape and size, and defects (pores) on fibers [11,12]. Inclination (vertical or horizontal) of the hollow needle also has the influence on electrospun fibers.

To the best of our knowledge, no $MgWO_4$ nanofibers have ever been synthesized by electrospinning and high temperature calcination. It is therefore for us to use the mixture of inorganic and organic salts dissolving in poly(vinyl alcohol) (PVA) to synthesize inorganic–polymeric fibers, which would transform into nanofibers by subsequent calcination at high temperature. This success may

* Corresponding author at: Department of Chemistry, Faculty of Science, Chiang Mai University, Chiang Mai 50200, Thailand. Tel.: +66 53 943344; fax: +66 53 892277.
** Corresponding author at: Department of Physics and Materials Science, Faculty of Science, Chiang Mai University, Chiang Mai 50200, Thailand. Tel.: +66 53 941924; fax: +66 53 943445.
E-mail addresses: ttpthongtem@yahoo.com, ttpthongtem@gmail.com (T. Thongtem), schthongtem@yahoo.com (S. Thongtem).

0169-4332/$ – see front matter © 2012 Elsevier B.V. All rights reserved.
doi:10.1016/j.apsusc.2012.01.133

Table 1
Product codes of the present research.

Product code	$(CH_3COO)_2Mg{\cdot}4H_2O$ (mmol)	$(NH_4)_6W_7O_{24}{\cdot}4H_2O$ (mmol)	PVA (g)	Calcination temperature (°C)/time (h)
P1	1.5	1.5	0.9	None
P2	1.5	1.5	1.1	None
P3	1.5	1.5	1.3	None
P3C1	1.5	1.5	1.3	500/3
P4	3.0	3.0	1.3	None
P4C1	3.0	3.0	1.3	500/3
P5	4.5	4.5	1.3	None
P5C1	4.5	4.5	1.3	500/3
P5C2	4.5	4.5	1.3	600/3
P5C3	4.5	4.5	1.3	700/3

lead to new industrial process by direct high voltage electrospinning.

2. Experiment

Different contents of magnesium acetate tetrahydrate ($(CH_3COO)_2Mg{\cdot}4H_2O$), ammonium (meta) tungstate tetrahydrate ($(NH_4)_6W_7O_{24}{\cdot}4H_2O$), and poly(vinyl alcohol) (PVA, 72,000 MW) were thoroughly mixed by dissolving in 30 ml deionized water each with 30 min stirring. Each of these mixtures was electrospun through a horizontal plastic syringe, biased with a +15 kV direct voltage to form fibers on a ground flat aluminum foil placed 15 cm apart. The fibers were also calcined at 500, 600, and 700 °C for 3 h constant length of time, and left them cool down to room

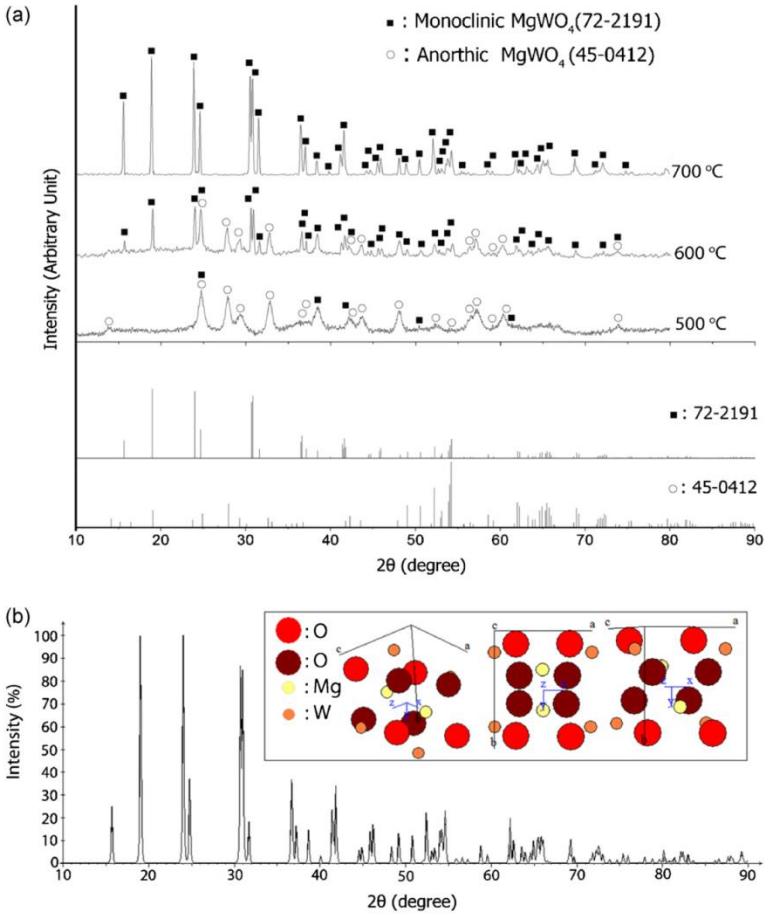

Fig. 1. (a) XRD spectra of the P5C1, P5C2 and P5C3 products, compared with the anorthic and monoclinic $MgWO_4$ phases. (b) Simulated XRD pattern and crystal structure of monoclinic $MgWO_4$.

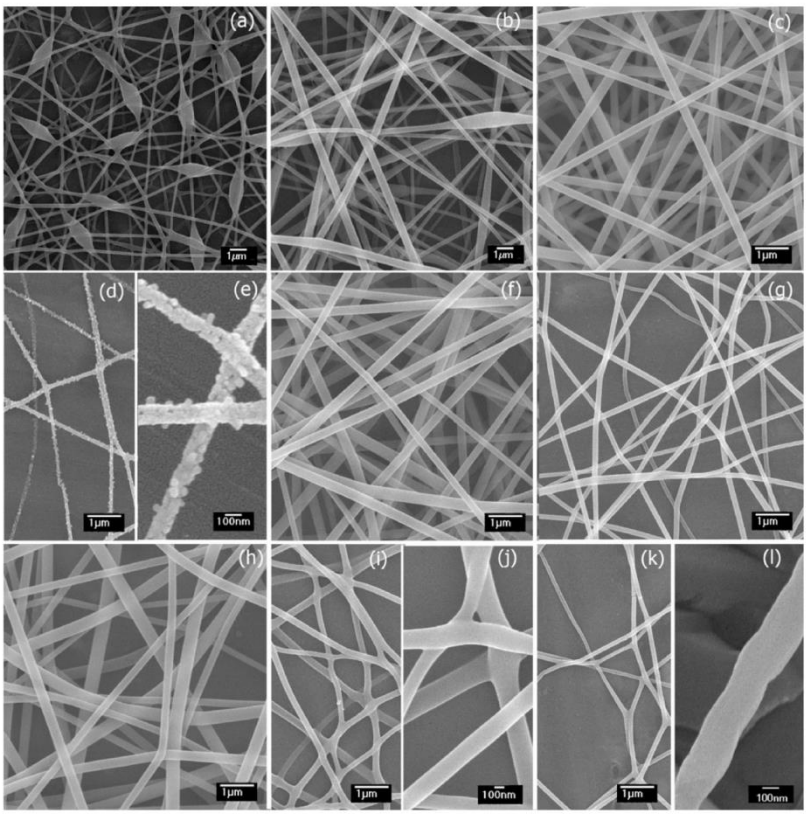

Fig. 2. SEM images of the (a) P1, (b) P2, (c) P3, (d and e) P3C1, (f) P4, (g) P4C1, (h) P5, (i and j) P5C1, (k) P5C2 and (l) P5C3 products.

temperature. The products synthesized from different contents of the starting materials with and without subsequent calcination at high temperatures were summarized and encoded (Table 1). These products were further characterized by X-ray diffractometer (XRD, SIEMENS D500) operating at 20 kV 15 mA, and using Cu-K_α line, in combination with the database of the Joint Committee on Powder Diffraction Standards (JCPDS) [13]; scanning electron microscope (SEM, JEOL JSM-6335F) operating at 15 kV; transmission electron microscope (TEM, JEOL JEM-2010), high resolution transmission electron microscope (HRTEM) and selected area electron diffractometer (SAED) operating at 200 kV; atomic force microscope (AFM, NanoScope IIIa, MMAFML N, Veeco) with silicon tip driven at a frequency of 200–300 kHz tapping mode; UV–visible spectrometer (Lambda 25 PerkinElmer) using a UV lamp with the resolution of 1 nm; and photoluminescence (PL) spectrometer (LS 50B PerkinElmer) using a 290 nm excitation wavelength at room temperature.

3. Results and discussion

3.1. XRD

XRD spectra (Fig. 1a) of the P5C1, P5C2 and P5C3 products show that chemical reactions of the starting materials were completed. $MgWO_4$ with anorthic (JCPDS no. 45-0412) and monoclinic (JCPDS no. 72-2191) [13] were successfully synthesized. During electrospinning by a +15 kV direct voltage, $(CH_3COO)_2Mg{\cdot}4H_2O$ reacted with $(NH_4)_6W_7O_{24}{\cdot}4H_2O$ to synthesize $MgWO_4$ molecules, blended in the PVA template.

$$7Mg^{2+} + (W_7O_{24})^{6-} + 4H_2O \rightarrow 7MgWO_4 + 8H^+ \quad (1)$$

$(CH_3COO)_2Mg{\cdot}4H_2O$ and $(NH_4)_6W_7O_{24}{\cdot}4H_2O$ could remain in the template but their concentrations were too low to be detected by XRD. By calcination at 500 °C for 3 h, PVA evaporated and decomposed. The PVA was no longer detected at 494 °C and above [14]. At the same time, the $(CH_3COO)_2Mg{\cdot}4H_2O$ and $(NH_4)_6W_7O_{24}{\cdot}4H_2O$ residues combined to form $MgWO_4$ molecules, which nucleated and grew to be particles (mixed phases) with different orientations. Upon increasing of the calcination temperature to 600 °C, the anorthic phase became lessened, with the greater extent of the monoclinic one. At 700 °C and 3 h calcination, only the monoclinic crystal structure was detected, and the product was the best crystal – the atoms resided in perfect crystal lattice. Its calculated lattice parameters [15] (Table 2) were very close to those of the standard values [13], which supported the presence of $MgWO_4$ with monoclinic crystal system. By using the Scherrer formula [15], crystallite sizes of the P5C1, P5C2 and P5C3 products were calculated and summarized in Table 2. Crystallite sizes of both anorthic and monoclinic phases were increased

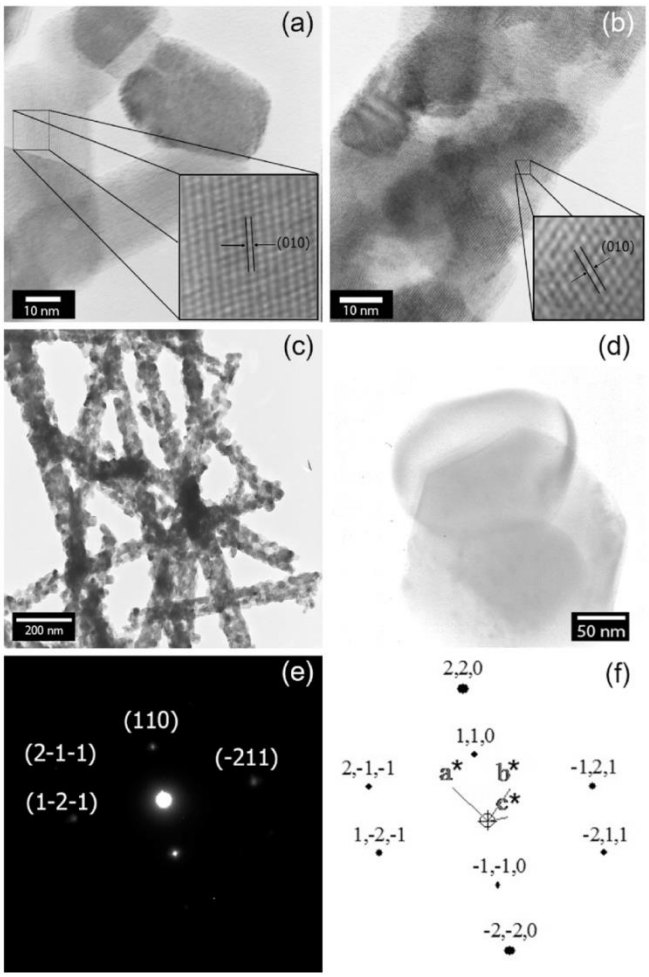

Fig. 3. TEM and HRTEM images, and SAED and simulated patterns of the (a) P3C1, (b and c) P5C1 and (d–f) P5C3 products.

with the increasing in the calcination temperatures, but the rate of increasing for the first was slower than that for the second. It should be noted that the anorthic crystallites were smaller than the monoclinic ones.

XRD pattern of monoclinic $MgWO_4$ was simulated [16] as shown in Fig. 1b. In the present research, the 2θ Bragg's angles and peak intensities of the experiment, simulation and JCPDS database were in good accordance. Simulated crystal structure of monoclinic $MgWO_4$ (inset of Fig. 1b) was explained as network of interconnecting zigzag chains of alternate MgO_6 and WO_6 distorted octahedrons running along the [0 0 1] direction, with Mg ions in the O ion polyhedrons [10].

Table 2
Lattice parameters and crystallite sizes of the P5C1, P5C2 and P5C3 products.

Product	Lattice parameter (nm)			Crystallite size (nm)	
	a	*b*	*c*	Anorthic	Monoclinic
P5C1	–	–	–	15.0	23.0
P5C2	–	–	–	29.6	68.8
P5C3	0.465	0.564	0.490	–	69.8

3.2. SEM, TEM, HRTEM, SAED and AFM

SEM, TEM and HRTEM images (Figs. 2 and 3a–d) show external surfaces of the products electrospun from different contents of the starting materials, before and after calcination at 500, 600, and 700 °C for 3 h constant length of time. Before calcination, some beads were detected on the P1 and P2 products (Fig. 2a and b) but no longer detected on the P3 product (Fig. 2c). Upon increasing the amount of PVA, the beads became lessened. Finally, they were no longer detected. These showed that the increase of viscosity of the mixtures played the role in the absence of beads on the electrospun fibers. The mixture of 1.5 mmol $(CH_3COO)_2Mg{\cdot}4H_2O$), 1.5 mmol $(NH_4)_6W_7O_{24}{\cdot}4H_2O$ and 1.3 g PVA has the viscosity and density high enough to form the bead-free electrospun fibers. By

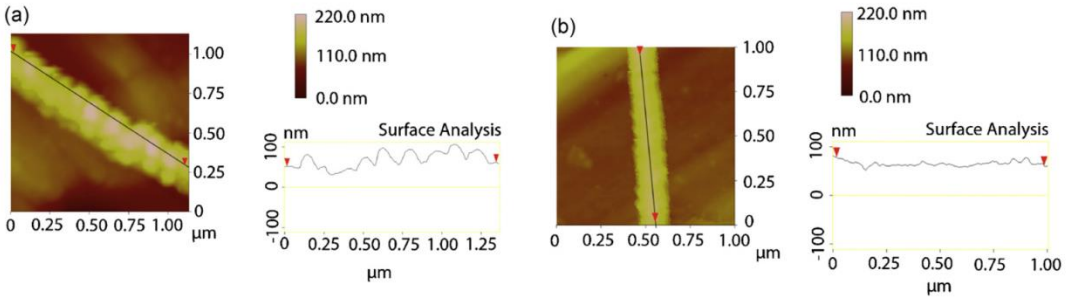

Fig. 4. AFM images and surface roughness of the (a) P4C1 and (b) P5C1 products.

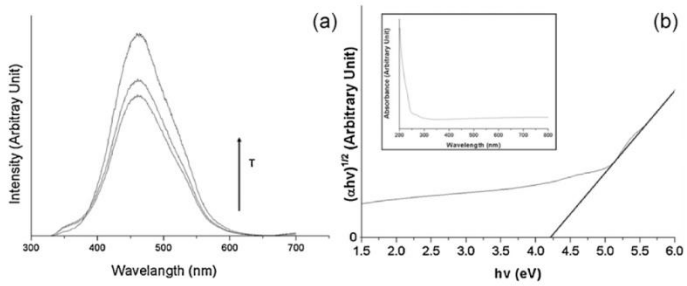

Fig. 5. (a) PL emission of the P5C1, P5C2 and P5C3 products, and (b) UV–visible absorption of the P5C3 product.

increasing the amount of the starting materials but keeping the amount of PVA constant at 1.3 g, the products were still to be bead-free electrospun fibers (Fig. 2f and h). $MgWO_4$ molecules and nanoparticles in the fibers became denser, proved by the P3C1, P4C1 and P5C1 products (Figs. 2d, e, g, i, j, and 3a–c). Surfaces of the fibers were roughened. The products were composed of interconnecting of facet nanoparticles along the fibrous axes. Upon increasing the calcination temperature of the P5C1 product from 500 °C to 600 °C (P5C2) and 700 °C (P5C3) (Figs. 2k, l, and 3d), both the nanoparticles and fibers were enlarged. A number of the (0 1 0) crystallographic planes of typical nanoparticles of the P3C1 and P5C1 products (insets of Fig. 3a and b) were detected by HRTEM – revealing the presence of crystalline $MgWO_4$ in the fibers. A SAED pattern of the P5C3 product (Fig. 3e) corresponded to the database of the monoclinic $MgWO_4$ [13], and the pattern obtained by simulation (Fig. 3f) [16].

AFM images and surface roughness of the P4C1 and P5C1 products are shown in Fig. 4. After 500 °C and 3 h calcination, the fibers were very rough and uneven, which reflected on their surface energy. Root mean square (RMS) values and maximum heights were 19.671 nm and 60.275 nm for the first, and 4.761 nm and 27.421 nm for the second, respectively. Each of these products contained particles with different sizes connecting as fiber-like assembly – in accordance with the above SEM and TEM analyses.

3.3. PL emission and UV–visible absorption

By using 290 nm excitation wavelength, PL emissions (Fig. 5a) of the P5C1, P5C2 and P5C3 products were detected at 461 nm – in accordance with the report of Danevich et al. [8]. The different emission was caused by the distorted $(WO_6)^{6-}$ octahedrons, Jahn–Teller effect, and the perturbation of $(WO_4)^{2-}$ tetrahedrons induced by defects [17].

UV–visible absorption (Fig. 5b) of P5C3 indicated an exponential decreasing of photonic absorption attenuated through the product. Its indirect E_g was determined, by extrapolating linear portion of the curve to zero absorption, to be 4.19 eV – very close to that reported by Lacomba-Perales et al. [1], and Kim et al. [18]. Particle-sizes and morphologies could play the role in the absorbance characteristics [19,20], having the influence on the energy gap.

4. Conclusions

The mixture of 4.5 mmol $(CH_3COO)_2Mg{\cdot}4H_2O$, 4.5 mmol $(NH_4)_6W_7O_{24}{\cdot}4H_2O$ and 1.3 g PVA was electrospun through a +15 kV direct voltage to form $MgWO_4$–PVA fibers, which were followed by 700 °C calcination for 3 h to form interconnecting facet nanoparticles of $MgWO_4$ along the fibrous axes with 4.19 eV indirect band gap and 461 nm PL emission – the promising nanofibers for a variety of applications.

Acknowledgements

We wish to thank the National Nanotechnology Center (NANOTEC), National Science and Technology Development Agency, Thailand, for providing financial support through the project code: P-10-11345; the Thailand's Office of the Higher Education Commission through the National Research University Project, and the Strategic Scholarships for Frontier Research Network of the Joint Ph.D. Research Program; and the Thailand Research Fund (TRF) through the TRF Research Grant, including the Graduate School of Chiang Mai University through the general support.

References

[1] R. Lacomba-Perales, J. Ruiz-Fuertes, D. Errandonea, D. Martínez-García, A. Segura, Optical absorption of divalent metal tungstates: correlation between the band-gap energy and the cation ionic radius, EPL 83 (2008), 37002 (5pp).

[2] Z. Lou, M. Cocivera, Cathodoluminescence of $CaWO_4$ and $SrWO_4$ thin films prepared by spray pyrolysis, Mater. Res. Bull. 37 (2002) 1573–1582.

[3] S.H. Yu, B. Liu, M.S. Mo, J.H. Huang, X.M. Liu, Y.T. Qian, General synthesis of single-crystal tungstate nanorods/nanowires: a facile, low-temperature solution approach, Adv. Funct. Mater. 13 (2003) 639–647.

[4] A. Golubović, R. Gajić, Z. Dohčević-Mitrović, S. Nikolić, Nd induced changes in IR spectra of $CaWO_4$ single crystals, J. Alloys Compd. 415 (2006) 16–22.

[5] X. Wang, H. Xu, H. Wang, H. Yan, Morphology-controlled $BaWO_4$ powders via a template-free precipitation technique, J. Cryst. Growth 284 (2005) 254–261.

[6] J.T. Kloprogge, M.L. Weier, L.V. Duong, R.L. Frost, Microwave-assisted synthesis and characterisation of divalent metal tungstate nanocrystalline minerals: ferberite, hübnerite, sanmartinite, scheelite and stolzite, Mater. Chem. Phys. 88 (2004) 438–443.

[7] V.B. Mikhailik, H. Kraus, V. Kapustyanyk, M. Panasyuk, Y. Prots, V. Tsybulskyi, L. Vasylechko, Structure, luminescence and scintillation properties of the $MgWO_4$–$MgMoO_4$ system, J. Phys.: Condens. Matter 20 (2008) 365219 (8 pp).

[8] F.A. Danevich, D.M. Chernyak, A.M. Dubovik, B.V. Grinyov, S. Henry, H. Kraus, V.M. Kudovbenko, V.B. Mikhailik, L.L. Nagornaya, R.B. Podviyanuk, O.G. Polischuk, I.A. Tupitsyna, Y.Y. Vostretsov, $MgWO_4$ – a new crystal scintillator, Nucl. Instrum. Methods Phys. Res. A 608 (2009) 107–115.

[9] M. Zhang, J. Zhai, J. Zhang, H. Jiang, X. Yao, Effect of $MgWO_4$ content on properties of $Ba_{0.5}Sr_{0.5}TiO_3$ composite ceramics for tunable microwave applications, Mater. Res. Bull. 46 (2011) 1102–1106.

[10] E. Cavalli, A. Belletti, M.G. Brik, Optical spectra and energy levels of the Cr^{3+} ions in MWO_4 (M = Mg, Zn, Cd) and $MgMoO_4$ crystals, J. Phys. Chem. Solids 69 (2008) 29–34.

[11] J.M. Deitzel, J. Kleinmeyer, D. Harris, N.C.B. Tan, The effect of processing variables on the morphology of electrospun nanofibers and textiles, Polymer 42 (2001) 261–272.

[12] Z.M. Huang, Y.Z. Zhang, M. Kotaki, S. Ramakrishna, A review on polymer nanofibers by electrospinning and their applications in nanocomposites, Compos. Sci. Technol. 63 (2003) 2223–2253.

[13] Powder Diffract. File, JCPDS-ICDD, 12 Campus Boulevard, Newtown Square, PA 19073-3273, USA, 2001.

[14] S. Wannapop, T. Thongtem, S. Thongtem, Characterization of $SrWO_4$–PVA and $SrWO_4$ spiders' webs synthesized by electrospinning, Ceram. Int. 37 (2011) 3499–3507.

[15] C. Suryanarayana, M.G. Norton, X-ray Diffraction: A Practical Approach, Plenum Press, New York, 1998.

[16] C. Boudias, D. Monceau, CaRIne Crystallography 3.1, Divergent S.A., Centre de Transfert, 60200 Compiègne, France, 1989–1998.

[17] V.B. Mikhailik, H. Kraus, D. Wahl, H. Ehrenberg, M.S. Mykhaylyk, Optical and luminescence studies of $ZnMoO_4$ using vacuum ultraviolet synchrotron radiation, Nucl. Instrum. Methods Phys. Res. A 562 (2006) 513–516.

[18] D.W. Kim, I.S. Cho, S.S. Shin, S. Lee, T.H. Noh, D.H. Kim, H.S. Jung, K.S. Hong, Electronic band structures and photovoltaic properties of MWO_4 (M = Zn, Mg, Ca, Sr) compounds, J. Solid State Chem. 184 (2011) 2103–2107.

[19] M. Hojamberdiev, G. Zhu, Y. Xu, Template-free synthesis of $ZnWO_4$ powders via hydrothermal process in a wide pH range, Mater. Res. Bull. 45 (2010) 1934–1940.

[20] Y. Keereeta, T. Thongtem, S. Thongtem, Fabrication of $ZnWO_4$ nanofibers by a high direct voltage electrospinning process, J. Alloys Compd. 509 (2011) 6689–6695.

Available online at www.sciencedirect.com
ScienceDirect
Ceramics International 37 (2011) 3499–3507
CERAMICS INTERNATIONAL
www.elsevier.com/locate/ceramint

Characterization of $SrWO_4$–PVA and $SrWO_4$ spiders' webs synthesized by electrospinning

Surangkana Wannapop [a], Titipun Thongtem [b,c,*], Somchai Thongtem [a,c]

[a] Department of Physics and Materials Science, Faculty of Science, Chiang Mai University, Chiang Mai 50200, Thailand
[b] Department of Chemistry, Faculty of Science, Chiang Mai University, Chiang Mai 50200, Thailand
[c] Materials Science Research Center, Faculty of Science, Chiang Mai University, Chiang Mai 50200, Thailand

Received 30 March 2011; received in revised form 31 May 2011; accepted 6 June 2011
Available online 12 June 2011

Abstract

Mixtures of strontium acetate, ammonium metatungstate hydrate, and different contents of poly (vinyl alcohol) (PVA, 125,000 MW) were electrospun by a +15 kV direct voltage to synthesize $SrWO_4$–PVA spiders' webs. The spider's web, synthesized from the solution containing 1.3 g PVA, was further calcined in air at 300–600 °C for 3 h. The $SrWO_4$–PVA spider's web was analyzed by thermogravimetric analyzer (TGA) to specify the evaporation and decomposition of PVA and volatile components. In addition, the $SrWO_4$–PVA and $SrWO_4$ spiders' webs were characterized by X-ray diffractometer (XRD), selected area electron diffraction (SAED), scanning and transmission electron microscopes (SEM, TEM), and ultraviolet (UV)–visible and photoluminescence (PL) spectrometers, including the vibration modes by Fourier transform infrared (FTIR) and Raman spectrometers. A possible formation mechanism of $SrWO_4$–PVA and $SrWO_4$ spiders' webs was also proposed according to the experimental results.

Keywords: A. Electrospinning; B. Electron microscopy; C. Optical properties; E. Sensors

1. Introduction

Strontium tungstate, one of scheelite-type tetragonal metal tungstates, is very interesting for a variety of applications, such as photoluminescence, light emitting diodes (LEDs), solid state Raman lasers, optical fibers, scintillating materials, humidity sensors, and catalysts [1–5]. It belongs to $I4_1/a$ space group with two formula units per primitive cell. Each of W atoms is surrounded by four equivalent O atoms composing the $[WO_4]^{2-}$ tetrahedral configuration, and each divalent strontium atom shares corners with eight adjacent O atoms of $[WO_4]^{2-}$ tetrahedrons [3,4]. It is very interesting and attractive phosphor material, due to its structural properties, great potential and promising applications, excellent thermal and hydrolytic stability, strong absorption in the near ultraviolet range, and good mechanical property and Raman gains [2,3,5].

Nanomaterials have very interesting properties, which are different from their bulks. These properties are controlled by uniform shape and narrow size distribution [6,7]. There are a variety of methods used to synthesize metal tungstates, such as high temperature solid state reaction in ambient air [2,3], spray pyrolysis [7], co-precipitation [4], sonochemistry [1,8], and Czochralski method [9].

Basically, there are three components used to synthesize electrospun fibers by the electrospinning process: a direct current (d.c.) power supply, a long hollow needle, and an electrical conducting screen. During electrospinning, a drop of polymeric solution at the tip of the hollow needle is charged by a positive direct high voltage. The mutual positive charge repulsion on the polymeric droplet is created. When the applied d.c. voltage is increased, the liquid droplet is stretched to be a conical shape, known as Taylor cone. Upon further increasing the d.c. voltage until it is sufficiently high, the repulsive force overcomes the surface tension of the polymeric liquid, and the jet of liquid is ejected out of the Taylor cone. Meanwhile, the

? Corresponding author at: Department of Chemistry, Faculty of Science, Chiang Mai University, Chiang Mai 50200, Thailand. Tel.: +66 (0) 53 943344; fax: +66 (0) 53 892277.
E-mail addresses: ttpthongtem@yahoo.com, ttpthongtem@hotmail.com (T. Thongtem).

0272-8842/$36.00
doi:10.1016/j.ceramint.2011.06.005

liquid jet evaporates and solidifies, leaving behind the polymeric fibers deposited on the ground-conducting screen [10].

There are several parameters that have the influence on the electrospun fibers: (a) variable parameters of the electrospinning equipment (applied voltage at the needle tip as well as electric field inside the fiber, pressure used to push the liquid out of the hollow needle, and distance between the needle tip and the ground conducting screen), (b) solution properties (viscosity, surface tension, elasticity, and conductivity), and (c) ambient parameters (temperature, humidity, and wind blow). These can play the role in the morphologies of the electrospun fiber, like fibrous diameter, number of the beads including their shape and size, and defects (pores) on the fiber [11]. Inclination (vertical or horizontal) of the hollow needle has the influence on the fiber as well.

$SrWO_4$–PVA spiders' webs are very novel and promising products for a variety of applications. They are able to be synthesized by a high d.c. voltage electrospinning process. To the best of our knowledge, no $SrWO_4$–PVA spiders' webs have ever been synthesized by this process. In the present research, the mixture of inorganic and polymeric materials were used to synthesize the inorganic material-polymer electrospun fibrous webs, which would transformed into nanofibrous inorganic material webs by subsequent calcination at high temperatures. Moreover, the success in synthesizing the solid nanofibrous webs may lead to a new process for industrial scale production.

2. Experiment

In the present research, 4.5 mmol strontium acetate [$Sr(CH_3COO)_2$], 4.5 mmol ammonium metatungstate hydrate ($H_{26}N_6O_{40}W_{12}{\cdot}xH_2O$), and different contents of poly (vinyl alcohol) (PVA, 125,000 MW) were separately dissolved in 10 ml deionized water each, mixed, and vigorously stirred at 80 °C for 30 min. These mixtures were encoded as M10, M11, M12, and M13 for using 1.0, 1.1, 1.2, and 1.3 g PVA, respectively. Each of them was electrospun by a horizontal syringe needle biased with +15 kV from a d.c. power supply, to synthesize $SrWO_4$–PVA spiders' webs on a grounded vertical flat aluminum foil. The $SrWO_4$–PVA spider's web synthesized from the M13 mixture was selected to be calcined in air at 300 °C, 400 °C, 500 °C and 600 °C for 3 h, to synthesize $SrWO_4$ nanoparticles joined together as a spider's web. These products were characterized using thermogravimetric analyzer (TGA, Shimadzu TGA-50 analyzer, Japan) using a heating rate of 5 °C/min; X-ray diffractometer (XRD, SIEMENS D500, Germany) operating at 20 kV, 15 mA, and using Cu-Kα line, in combination with the database of the Joint Committee on Powder Diffraction Standards (JCPDS) [12]; scanning electron microscope (SEM, JEOL JSM-6335F, Japan) operating at 15 kV; transmission electron microscope (TEM, JEOL JEM-2010, Japan), high resolution transmission electron microscope (HRTEM) and selected area electron diffractometer (SAED) operating at 200 kV; Fourier transform infrared spectrometer (FTIR, Bruker Tensor 27, Germany) with KBr as a diluting agent and operated in the range of 4000–400 cm^{-1}; Raman spectrometer (T64000 HORIBA Jobin Yvon, U.S.A.) using a 50 mW and 514.5 nm wavelength Ar green laser; UV–vis spectrometer (Lambda 25 PerkinElmer, U.S.A.) using a UV lamp with the resolution of 1 nm; and photoluminescence (PL) spectrometer (LS 50B PerkinElmer, U.S.A.) using a 245 nm excitation wavelength at room temperature.

3. Results and discussion

3.1. TGA

Fig. 1 compares TGA curve of the M13 spider's web to that of PVA. The weight loss of pure PVA exhibited the evaporation and degradation processes for three steps over the temperature range of 32–494 °C. First, the weight loss of 9.5% was caused by the evaporation of loosely bound water at 32–194 °C. Second, the large amount of weight loss of 79.7% was predominantly due to the decomposition of PVA structure at 194–415 °C. Third, the 9.3% weight loss was by the breaking of PVA main chains at 415–494 °C. The weight loss tended to terminate upon further heating at above 494 °C [13].

Consider TGA curve of the M13 spider's web, the weight losses were divided into three different steps. The first weight loss at 32–218 °C was 15.8%, and associated with water evaporation. The second weight loss of 25.5% at 218–405 °C was caused by the decomposition of PVA. The final weight loss of 18.2% at 405–520 °C seemed to be the oxidation and decomposition of the PVA main chains. These last two steps were attributed to the loss of PVA and organic compound blended in the fibers. At a temperature above 520 °C, there was no significant change in their weight.

3.2. XRD

Fig. 2 shows XRD patterns of $SrWO_4$–PVA spider's web, synthesized from the M13 solution, after calcination at 300 °C, 400 °C, 500 °C and 600 °C for 3 h. Comparing with the JCPDS database no. 08-0490 [12], they were specified as the crystalline

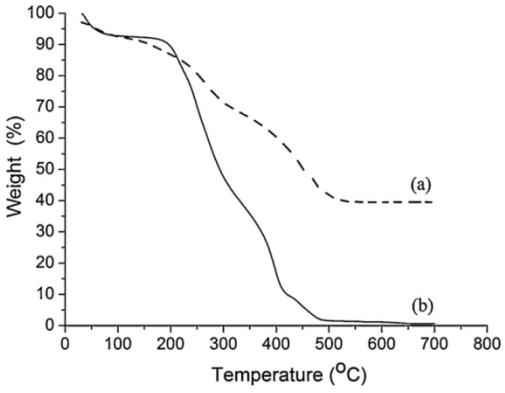

Fig. 1. TGA curves of (a) a spider's web synthesized from the M13 solution, and (b) PVA.

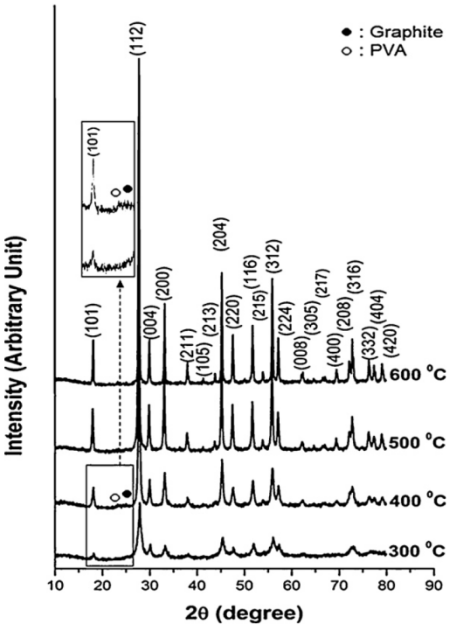

Fig. 2. XRD patterns of $SrWO_4$–PVA spider's web, synthesized from the M13 solution, after calcination at 300 °C, 400 °C, 500 °C and 600 °C for 3 h.

phase of tetragonal system ($a = b = 5.4168$ Å, $c = 11.9510$ Å, and $\alpha = \beta = \gamma = 90^\circ$) of $SrWO_4$ structure. At 300 °C calcination, the peaks of $SrWO_4$ were quite broad. This product contained very small contents of residual PVA at $2\theta = 22.5^\circ$ [14], and graphite at $2\theta = 26.3^\circ$ of JCPDS database no. 01-0640 [12] caused by the decomposition of PVA. The product has the color of light grey, due to some graphite residue. Upon calcination at 400 °C, both residual PVA and graphite were reduced, due to the evaporation of PVA and oxidation of graphite to be its oxides in gaseous form. Until at 500 °C and 600 °C calcination, they were no longer detected by the XRD. In addition, the XRD peaks became narrower and sharper, implying the improvement of products' crystalline degree and purity. At 600 °C calcination, the product was the best pure white crystalline $SrWO_4$.

Their average lattice parameters, calculated from the plane-spacing equation for tetragonal structure and Bragg's law for diffraction [15], were $a = b = 5.388$ Å, and $c = 11.898$ Å—very close to their corresponding standard values [12]. For scheelite structured $SrWO_4$, each Sr divalent ion was surrounded by eight O ions with each W ion in the tetrahedrons of O ions [4,16].

3.3. FTIR

The FTIR spectra (Fig. 3) were provided further insight into the structure of PVA, and $SrWO_4$–PVA spider's web synthesized from the M13 solution, before and after calcination at 300 °C, 400 °C, 500 °C and 600 °C for 3 h. Consider the PVA spectrum, a broad strong O–H stretching mode of alcohol and residual water was detected at 3600–3200 cm^{-1}. It was the stretching of hydroxyl groups with strong hydrogen bonding of

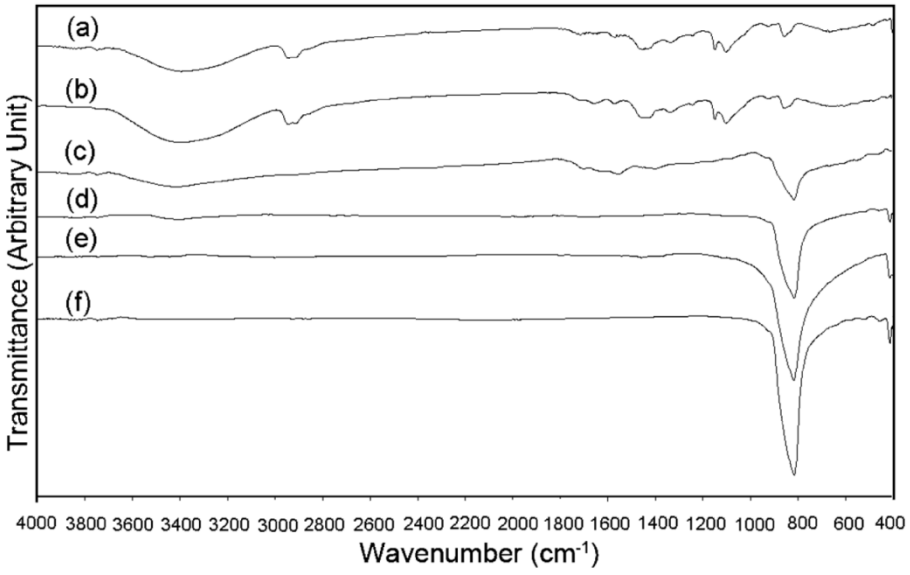

Fig. 3. FTIR spectra of (a) PVA, and (b)–(f) $SrWO_4$–PVA spider's web, synthesized from the M13 solution, before and after calcination at 300 °C, 400 °C, 500 °C and 600 °C for 3 h, respectively.

intra- and inter-types. Two strong vibration modes at 2945 and 2909 cm^{-1} corresponded to the asymmetric and symmetric C–H stretching of alkyl groups, respectively. The C=O stretching mode at 1656 cm^{-1} was caused by the carbonyl functional groups of the acetate remaining in PVA by the hydrolysis of polyvinyl acetate and oxidation process during manufacturing. The C=C stretching mode at 1566 cm^{-1} was caused by cross-linking of the PVA during heating. The presence of C=O and/or C=C stretching modes implied that PVA molecules have the same resonant structures: alkene ↔ alkane, and C=O ↔ C–O^-, or the presence of hydrogen bonds with oxygen of C=O groups. The 1439 cm^{-1} was specified as the CH_2 bending mode, the 1342 cm^{-1} as the C–CH_3 deformation vibration, and the 1241 cm^{-1} as the CH_2 wagging mode. The C–C and C–O–C stretching vibrations, recognized as the crystallization sensitive modes, were detected at 1147 cm^{-1}. The vibration at 1096 cm^{-1} was specified as the C–O stretching, and at 851 cm^{-1} as the C–C stretching [17]. Once, the as-synthesized $SrWO_4$-PVA spider's web was characterized by FTIR, additional modes of $SrWO_4$ were detected. For T_d-symmetry, vibration frequencies of $[WO_4]^{2-}$ tetrahedrons were $\nu_1(A_1)$, $\nu_2(E)$, $\nu_3(F_2)$ and $\nu_4(F_2)$ [18]. In lattice space, the site symmetries became S_4. The correlation of the two point groups ($T_d \rightarrow S_4$) is the following: $A_1 \rightarrow A$, $E \rightarrow A + B$ and $F_2 \rightarrow B + E$. Only the modes corresponding to ν_2, ν_3 and ν_4 were detected [18]. Main transmittance mode (ν_3) specified as W–O anti-symmetric stretching vibration of $[WO_4]^{2-}$ tetrahedrons in lattice space [18] was detected at 638–1003 cm^{-1}. Sometimes it split into two modes, sometimes it did not [18–20]. In the present research, they appeared as the strong broad band. The ν_4 split into two modes at the wavenumbers of less than 400 cm^{-1} [18]. When the $SrWO_4$–PVA spider's web was calcined in air at 300–600 °C for 3 h, the PVA and residual water began to evaporate and decompose. Additional weak peaks of W–O vibrations for 300 °C, 400 °C, 500 °C, and 600 °C were also detected at 410 cm^{-1}, specified as ν_2 bending modes [18,21]. At higher temperatures, the FTIR intensities were strengthened. The evaporation rates of PVA and water became faster, and their residues were lessened. Until at 600 °C calcination, the vibrations of PVA and water were no longer detected. The ν_3 anti-symmetric stretching and ν_2 bending modes became the strongest, and the product was really $SrWO_4$ electrospun nanofibrous web.

3.4. Raman analysis

The Raman vibrations of $SrWO_4$ were divided into two groups, the internal and external [22]. The internal mode was the W–O vibration within the $[WO_4]^{2-}$ tetrahedral units with immobile mass centers. The external or lattice phonon mode corresponded to the vibration of Sr^{2+} cations relative to the rigid $[WO_4]^{2-}$ tetrahedral units. In free space, $[WO_4]^{2-}$ tetrahedrons have T_d-symmetry [22,23]. Their vibrations were specified as four internal modes of $\nu_1(A_1)$, $\nu_2(E)$, $\nu_3(F_2)$ and $\nu_4(F_2)$, one free rotation of $\nu_{f.r.}(F_1)$, and one translation (F_2) [22]. In lattice space, they have S_4-symmetry. All degenerative vibrations were split [22,23] due to the crystal field effect and Davydov splitting [22]. According to group-theory calculation, there are 26 different modes for tetragonal scheelite primitive cell with zero wavevector ($\vec{k} = \vec{0}$): three for A_g and B_u, and five for A_u, B_g, E_g and E_u each. All modes of A_g, B_g and E_g were Raman-active. Four of five A_u and E_u modes were IR-active, and their remains were acoustic vibrations. Three vibrations of B_u were silent modes [22,24]. In the present research, six different modes of $\nu_1(A_g)$, $\nu_3(B_g)$, $\nu_3(E_g)$, $\nu_4(B_g)$, $\nu_2(A_g)$ and free rotation were detected on the Raman spectrum (Fig. 4) at 912, 831, 791, 373, 334 and 187 cm^{-1}—in accordance with those of the previous reports [22,23]. This spectrum provided the evidence of scheelite structure of $SrWO_4$ [22,23] spider's web. Comparing to Ar laser (λ = 514.5 nm), a great deal of energy was lost during the inelastic scattering process.

3.5. SEM, TEM, HRTEM, and SAED

The $SrWO_4$–PVA spiders' webs synthesized from the solutions containing different contents of PVA are shown in Fig. 5a–d. The spiders' webs of the M10, M11, M12, and M13 solutions, respective containing 1.0, 1.1, 1.2, and 1.3 g PVA, were composed of fibers woven like spiders' webs. Some beads were also detected; especially, those synthesized from the mixtures of less than 1.3 g PVA. The number of beads was lessened in sequence with the increase of the PVA masses, and was no longer detected for 1.3 g PVA (M13) solution. The content of PVA can also play the role in the viscosity of the mixtures, which influenced the stability of the solution jets. For 1.3 g PVA, it was exactly right to eject the inorganic material-polymeric solution through the syringe out of the hollow needle, and the web was composed of the bead-free fibers. These implied that the fibers and beads were influenced by the stability of the jet of inorganic material-polymeric solutions, and PVA contents [11,25]. The M13 spider's web was then selected for further studies.

When the $SrWO_4$–PVA spider's web was calcined at 300–600 °C for 3 h (Figs. 5e–h and 6a, b, e and f), the fibers became thinner, due to the evaporation and decomposition of PVA and

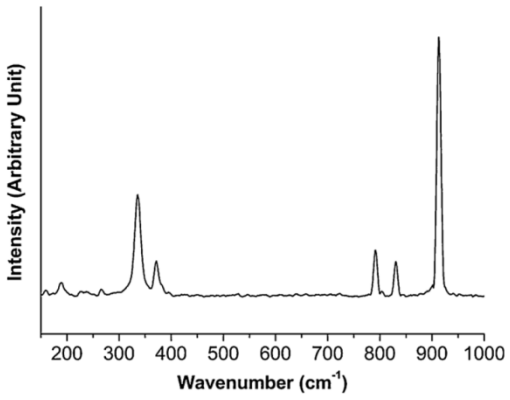

Fig. 4. Raman spectrum of $SrWO_4$ spider's web, synthesized from the M13 solution.

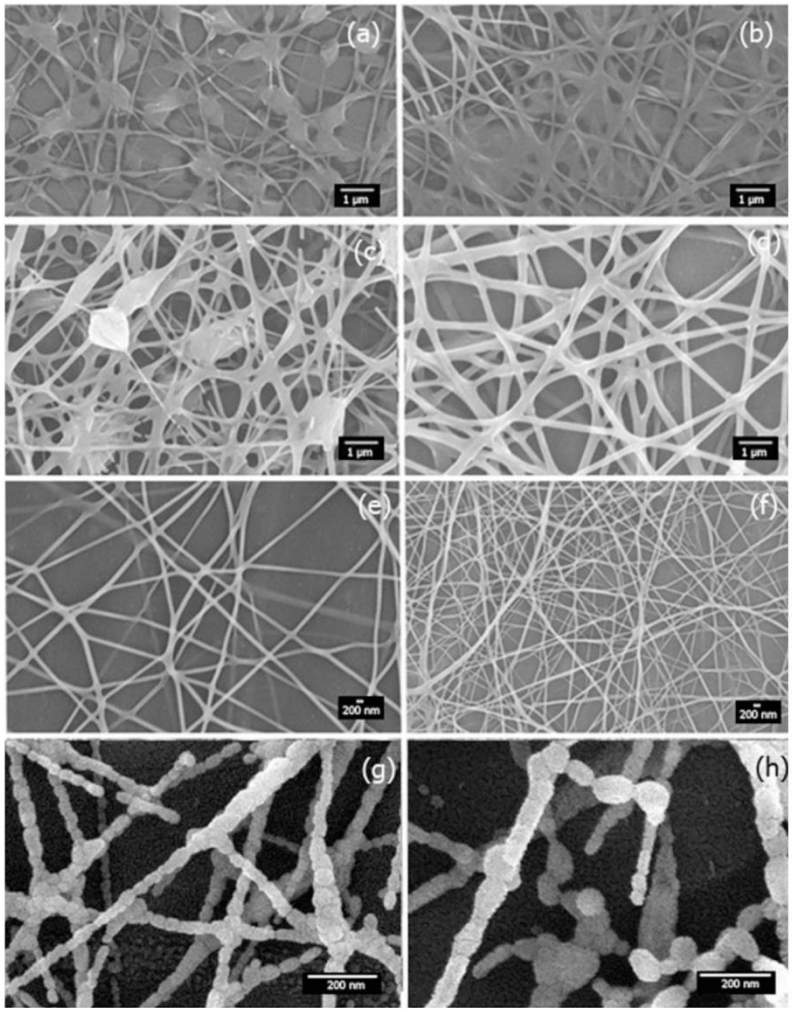

Fig. 5. SEM images of (a)–(d) $SrWO_4$–PVA spiders' webs synthesized from the M10, M11, M12, and M13 solutions, and (e)–(h) $SrWO_4$–PVA spider's web synthesized from the M13 solution after calcination at 300 °C, 400 °C, 500 °C, and 600 °C for 3 h, respectively.

volatile components. $SrWO_4$ nuclei also grew to form larger nanoparticles. Upon increasing the calcination temperatures, the evaporation and decomposition rates of PVA, as well as the growth rate of $SrWO_4$ nanoparticles, were increased. It was more than likely that PVA did not remain in the products with 500 °C and 600 °C calcination. These products were composed of nanoparticles with different sizes and orientations joined together like a spider's web. For close examination on a nanoparticle calcined at 500 °C, a number of parallel crystallographic planes were detected by HRTEM (Fig. 6b). They were specified as the (1 0 1) plane of tetragonal structured $SrWO_4$, implying that the nanoparticle was really a single crystal. SAED patterns were interpreted [26], and specified as the (1 0 1), (1 1 2) and (0 1 1) planes (Fig. 6c) with electron beam in the $[\bar{1}\,\bar{1}\,1]$ direction, and the (2 0 0), (2 2 0) and (0 2 0) planes (Fig. 6g) with electron beam in the [0 0 1] direction for the nanoparticles of 500 °C and 600 °C calcination, respectively. They corresponded to the JCPDS database for tetragonal structured $SrWO_4$ [12]–in good accordance with the above XRD analysis. Diffraction patterns of these products (Fig. 6d and h) were also simulated [27] using the corresponding electron beams. They are in systematic and symmetric order, with the a*, b* and c* reciprocal lattice vectors for both patterns in the [1 0 0], [0 1 0], and [0 0 1] directions. For one crystal structure, the corresponding reciprocal lattice vectors were the same although the electron beams were different. Comparing

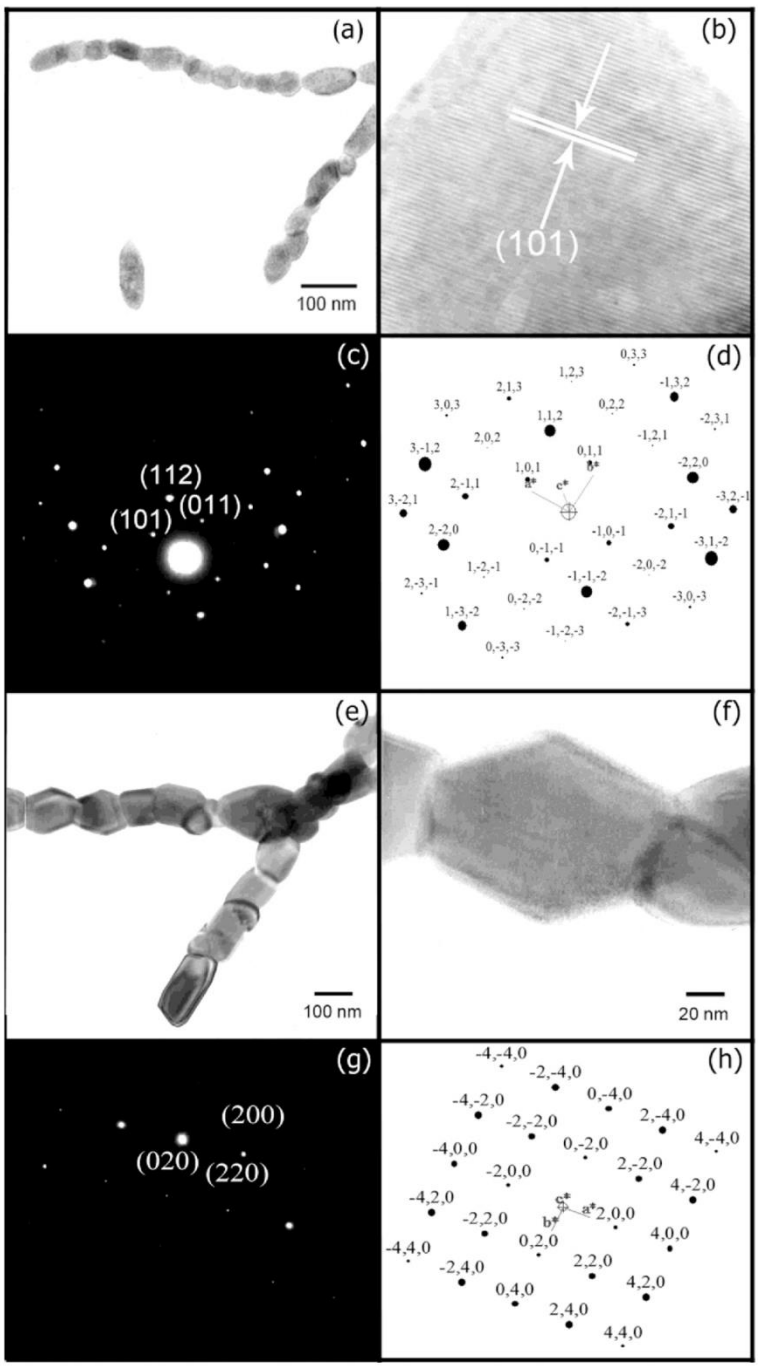

Fig. 6. TEM and HRTEM images, and SAED and simulated patterns of $SrWO_4$–PVA spider's web, synthesized from the M13 solution, after calcination at (a)–(d) 500 °C, and (e)–(h) 600 °C for 3 h.

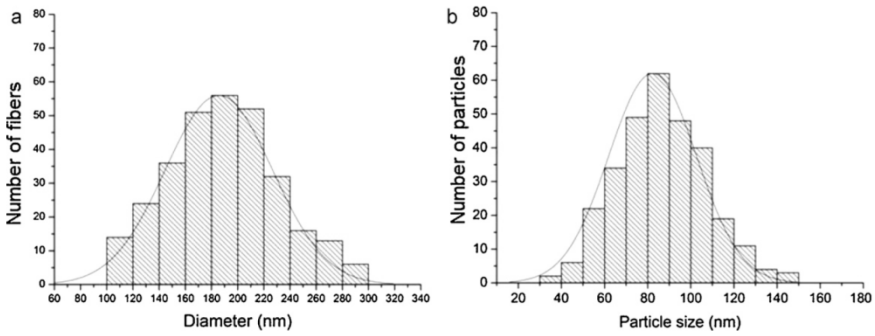

Fig. 7. (a) and (b) Distributions of fibrous diameters and particle sizes of the $SrWO_4$–PVA spider's web, synthesized from the M13 solution, before and after calcination at 600 °C for 3 h, respectively.

between the corresponding interpreted and simulated patterns, they are in good accordance.

3.6. Distributions of fibers and particles

Distributions of fibrous diameters and particle sizes of the spider's web, synthesized from the M13 solution, before and after calcination at 600 °C for 3 h are shown in Fig. 7. These fibrous diameters and particle sizes were started to be counted and arranged from the smallest to the largest values. Their distributions fitted very well with normal curves over the ranges of 60–320 nm with the average of 185.6 nm diameter, and 20–150 nm with the average of 82.3 nm particle size.

3.7. Formation mechanism

During electrospinning, electric field from a +15 d.c. kV voltage generated heat through the mixture of $Sr(CH_3COO)_2$, $H_{26}N_6O_{40}W_{12}{\cdot}xH_2O$, and PVA. Sr^{2+} cations (electron pair acceptors—Lewis acid) chemically combined with $[WO_4]^{2-}$ anions (electron pair donors—Lewis base). The chemical reaction between these two species ($Sr^{2+} \leftarrow :WO_4^{2-}$) proceeded to form covalent bonds. The lowest molecular orbital energy of Lewis acid interacted with the highest molecular orbital energy of Lewis base. $SrWO_4$ molecules were finally synthesized [4,28], and nucleated to form nuclei, blended in the PVA fibrous template. Due to the electrospinning, the products were in the shape of spiders' webs. Upon calcination at high temperatures, $SrWO_4$ nuclei grew to form larger nanoparticles. Their growth rates were increased with the increasing in the calcination temperatures. At 600 °C calcination, the product was composed of a number of the biggest $SrWO_4$ nanoparticles joined together like nanofibers, woven in the shape of a spider's web.

3.8. UV–vis absorption

Fig. 8 shows the $(\alpha h\nu)^2$ vs $h\nu$ curve of the $SrWO_4$ spider's web. By using Wood and Tauc equation [4,16,28–30] below.

$$\alpha h\nu = \left(h\nu - E_g\right)^n \quad (1)$$

where α is the absorbance, h the Planck constant, ν the photon frequency, E_g the energy gap, and n the pure numbers associated with the different types of electronic transitions. For n = 1/2, 2, 3/2 and 3, the transitions are the direct allowed, indirect allowed, direct forbidden, and indirect forbidden, respectively. It should be noted that the absorption was controlled by two photon energy ($h\nu$) ranges—the high and low energies. When the photon energy was greater than the energy band gap, absorption was linearly increased with the increasing of photon energy. The steep inclination of the linear portion of the curve was caused by the UV absorption for charged transition from the topmost occupied state of valence band to the bottommost unoccupied state of the conduction band. For the photon energy with less than the energy band gap, the absorption curve became different from linearity, due to the UV absorption for charged transition relating to different defects. The direct energy gap (E_g) was determined by extrapolating the linear portion of the curve to the zero absorbance. In the present research, $SrWO_4$ with scheelite-type tetragonal structure presented the direct allowed electronic transition [4,28,30], with

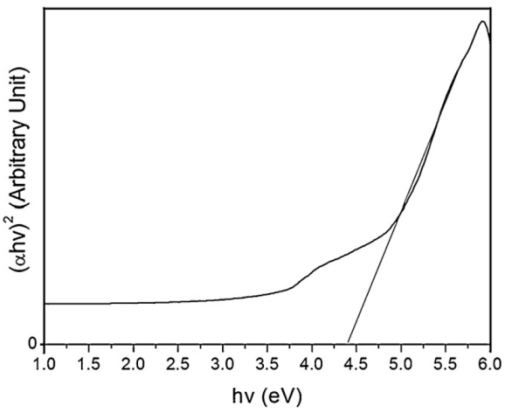

Fig. 8. The $(\alpha h\nu)^2$ versus $h\nu$ plot of the $SrWO_4$ spider's web, synthesized from the M13 solution.

the energy gap of 4.47 eV—in good accordance with the previous reports [16]. In fact, energy gap is controlled by several factors such as the electronegativity of transition metal ions, connectivity of the polyhedrons, deviation in the O–W–O bonds, distortion of the $[WO_4]^{2-}$ tetrahedrons, growth mechanism, and degree of structural order–disorder in the lattice [16,28].

3.9. Photoluminescence

PL spectra of $SrWO_4$–PVA spider's web, synthesized from the M13 solution, after calcination at 300 °C, 400 °C, 500 °C and 600 °C for 3 h (Fig. 9) show the intrinsic peaks with their surrounding shoulders. The intrinsic peaks were due to the $^1T_2 \rightarrow {}^1A_1$ transition of electrons within $[WO_4]^{2-}$ anions [31,32], which were treated as excitons. The shoulders were caused by some defects and/or impurities, and interpreted as extrinsic transition. Generally, PL intensity is controlled by the number of charged transition. In the present research, the emission peaks were in the spectral region at 439–441 nm—having the potential applications for photonic sensors and devices. Starting from 300 °C to 600 °C calcination, PL intensities were 74, 89, 98, and 100%, respectively. They were increased with the increase in the calcination temperatures, and became the highest at 600 °C calcination.

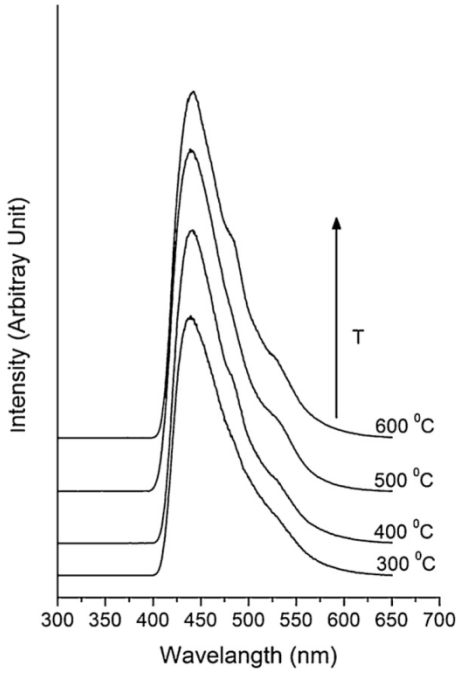

Fig. 9. PL spectra of $SrWO_4$–PVA spider's web, synthesized from the M13 solution, after calcination at 300 °C, 400 °C, 500 °C and 600 °C for 3 h.

4. Conclusions

$SrWO_4$–PVA spiders' webs were synthesized from strontium acetate, ammonium metatungstate hydrate, and different contents of poly (vinyl alcohol) (PVA, 125,000 MW) by the +15 kV direct voltage electrospinning process. In the present research, the $SrWO_4$–PVA spider's web synthesized from the solution containing 1.3 g PVA were further calcined in air at 300 °C, 400 °C, 500 °C and 600 °C for 3 h. At 600 °C calcination, the product was tetragonal scheelite structured $SrWO_4$ nanofibers shaped like a spider's web with the luminescence emission of 439–441 nm, and direct energy gap of 4.47 eV—one of the promising products for a wide variety of applications.

Acknowledgements

We wish to thank the Thailand's Office of the Higher Education Commission for providing financial support through the National Research University (NRU) Project, and the Strategic Scholarships for Frontier Research Network of the Joint Ph.D. Research Program, and the Graduate School of Chiang Mai University for general support.

References

[1] L.D. Feng, X.B. Chen, C.J. Mao, A facile synthesis of $SrWO_4$ nanobelts by the sonochemical method, Mater. Lett. 64 (2010) 2420–2423.
[2] Z.H. Ju, R.P. Wei, J.X. Ma, C.R. Pang, W.S. Liu, A novel orange emissive phosphor $SrWO_4:Sm^{3+}$ for white light-emitting diodes, J. Alloys Compd. 507 (2010) 133–136.
[3] Z. Ju, R. Wei, X. Gao, W. Liu, C. Pang, Red phosphor $SrWO_4:Eu^{3+}$ for potential application in white LED, Opt. Mater. 33 (2011) 909–913.
[4] T. Thongtem, S. Kungwankunakorn, B. Kuntalue, A. Phuruangrat, S. Thongtem, Luminescence and absorbance of highly crystalline $CaMoO_4$, $SrMoO_4$, $CaWO_4$ and $SrWO_4$ nanoparticles synthesized by co-precipitation method at room temperature, J. Alloys Compd. 506 (2010) 475–481.
[5] Y. Duan, F. Yang, H. Zhu, Z. Zhu, C. Huang, Z. You, Y. Wei, G. Zhang, C. Tu, Continuous-wave 560 nm light generated by intracavity $SrWO_4$ Raman and KTP sum-frequency mixing, Opt. Commun. 283 (2010) 5135–5138.
[6] D. Chen, G. Shen, K. Tang, H. Zheng, Y. Qian, Low-temperature synthesis of metal tungstates nanocrystallites in ethylene glycol, Mater. Res. Bull. 38 (2003) 1783–1789.
[7] S. Thongtem, S. Wannapop, T. Thongtem, Characterization of $CoWO_4$ nano-particles produced using the spray pyrolysis, Ceram. Int. 35 (2009) 2087–2091.
[8] T. Thongtem, S. Kaowphong, S. Thongtem, Sonochemical preparation of $PbWO_4$ crystals with different morphologies, Ceram. Int. 35 (2009) 1103–1108.
[9] D. Errandonea, F.J. Manjón, N. Garro, P. Rodríguez-Hernández, S. Radescu, A. Mujica, A. Muñoz, C.Y. Tu, Combined Raman scattering and ab initio investigation of pressure-induced structural phase transitions in the scintillator $ZnWO_4$, Phys. Rev. B 78 (2008) 054116–54121.
[10] J.M. Deitzel, J. Kleinmeyer, D. Harris, N.C. Beck Tan, The effect of processing variables on the morphology of electrospun nanofibers and textiles, Polymer 42 (2001) 261–272.
[11] Z.M. Huang, Y.Z. Zhang, M. Kotaki, S. Ramakrishna, A review on polymer nanofibers by electrospinning and their applications in nanocomposites, Compos. Sci. Technol. 63 (2003) 2223–2253.
[12] Powder Diffract. File, JCPDS-ICDD, 12 Campus Boulevard, Newtown Square, PA 19073-3273, U.S.A. 2001.

[13] E.A. El-hefian, M.M. Nasef, A.H. Yahaya, The preparation and characterization of chitosan/poly (vinyl alcohol) blended films, E-J. Chem. 7 (2010) 1212–1219.
[14] K. Pal, A.K. Banthia, D.K. Majumdar, Preparation and characterization of polyvinyl alcohol–gelatin hydrogel membranes for biomedical applications, AAPS PharmSciTech 8 (2007), doi:10.1208/pt080121, Art. No. 21.
[15] C. Suryanarayana, M.G. Norton, X-ray Diffraction: A Practical Approach, Plenum Press, New York, 1998.
[16] J.C. Sczancoski, L.S. Cavalcante, M.R. Joya, J.W.M. Espinosa, P.S. Pizani, J.A. Varela, E. Longo, Synthesis, growth process and photoluminescence properties of $SrWO_4$ powders, J. Colloids Interface Sci. 330 (2009) 227–236.
[17] Z.I. Ali, F.A. Ali, A.M. Hosam, Effect of electron beam irradiation on the structural properties of PVA/V2O5 xerogel, Spectrochim. Acta Part A 72 (2009) 868–875.
[18] G.M. Clark, W.P. Doyle, Infra-red spectra of anhydrous molybdates and tungstates, Spectrochim. Acta 22 (1966) 1441–1447.
[19] G. Zhang, R. Jia, Q. Wu, Preparation, structural and optical properties of AWO_4 (A = Ca, BaSr) nanofilms, Mater. Sci. Eng. B 128 (2006) 254–259.
[20] F.A. Miller, C.H. Wilkins, Infrared spectra and characteristic frequencies of inorganic ions, Anal. Chem. 24 (1952) 1253–1294.
[21] R.L. Frost, L. Duong, M. Weier, Raman microscopy of selected tungstate minerals, Spectrochim. Acta Part A 60 (2004) 1853–1859.
[22] T.T. Basiev, A.A. Sobol, Y.K. Voronko, P.G. Zverev, Spontaneous Raman spectroscopy of tungstate and molybdate crystals for Raman lasers, Opt. Mater. 15 (2000) 205–216.
[23] S.P.S. Porto, J.F. Scott, Raman spectra of $CaWO_4$, $SrWO_4$, $CaMoO_4$, and $SrMoO_4$, Phys. Rev. 157 (1967) 716–719.
[24] A. Golubović, R. Gajić, Z. Dohčević-Mitrović, S. Nikolić, Nd induced changes in IR spectra of $CaWO_4$ single crystals, J. Alloys Compd. 415 (2006) 16–22.
[25] B. Ding, H.Y. Kim, S.C. Lee, D.R. Lee, K.J. Choi, Preparation and characterization of nanoscaled poly (vinyl alcohol) fibers via electrospinning, Fiber Polym. 3 (2002) 73–79.
[26] K.W. Andrews, D.J. Dyson, S.R. Keown, Interpreting Electron Diffraction Patterns, Plenum Press, New York, 1971.
[27] C. Boudias, D. Monceau, CaRIne Crystallography 3.1, DIVERGENT S.A., Centre de Transfert, 60200 Compiègne, France, 1989–1998.
[28] L.S. Cavalcante, J.C. Sczancoski, R.L. Tranquilin, M.R. Joya, P.S. Pizani, J.A. Varela, E. Longo, $BaMoO_4$ powders processed in domestic microwave-hydrothermal: synthesis, characterization and photoluminescence at room temperature, J. Phys. Chem. Solids 69 (2008) 2674–2680.
[29] J.C. Sczancoski, L.S. Cavalcante, N.L. Marana, R.O. da Silva, R.L. Tranquilin, M.R. Joya, P.S. Pizani, J.A. Varela, J.R. Sambrano, M.S. Li, E. Longo, J. Andrés, Electronic structure and optical properties of $BaMoO_4$ powders, Curr. Appl. Phys. 10 (2010) 614–624.
[30] J.H. Ryu, B.G. Choi, J.W. Yoon, K.B. Shim, K. Machi, K. Hamada, Synthesis of $CaMoO_4$ nanoparticles by pulsed laser ablation in deionized water and optical properties, J. Lumin. 124 (2007) 67–70.
[31] A. Phuruangrat, T. Thongtem, S. Thongtem, Synthesis of lead molybdate and lead tungstate via microwave irradiation method, J. Cryst. Growth 311 (2009) 4076–4081.
[32] A. Phuruangrat, T. Thongtem, S. Thongtem, Preparation, characterization and photoluminescence of nanocrystalline calcium molybdate, J. Alloys Compd. 481 (2009) 568–572.

Materials Letters 64 (2010) 122–124

Contents lists available at ScienceDirect

Materials Letters

journal homepage: www.elsevier.com/locate/matlet

Characterization of Bi_2S_3 with different morphologies synthesized using microwave radiation

Titipun Thongtem [a,*], Anukorn Phuruangrat [b,*], Surangkana Wannapop [b], Somchai Thongtem [b]

[a] Department of Chemistry, Faculty of Science, Chiang Mai University, Chiang Mai 50200, Thailand
[b] Department of Physics and Materials Science, Faculty of Science, Chiang Mai University, Chiang Mai 50200, Thailand

ARTICLE INFO

Article history:
Received 17 May 2009
Accepted 6 October 2009
Available online 9 October 2009

Keywords:
Characterization methods
Electron microscopy
Nanomaterials

ABSTRACT

Bi_2S_3 with different morphologies (nanoparticles, nanorods and nanotubes) was synthesized using bismuth nitrate pentahydrate ($Bi(NO_3)_3{\cdot}5H_2O$) and two kinds of sulfur sources (CH_3CSNH_2 and NH_2CSNH_2) in different solvents (water, ethylene glycol and propylene glycol) via a microwave radiation method at 180 W for 20 min. X-ray powder diffraction (XRD), scanning electron microscopy (SEM) and transmission electron microscopy (TEM) indicated that all of the products are orthorhombic Bi_2S_3 phase of nanoparticles, nanorods and nanotubes, influenced by the sulfur sources and solvents. Formation mechanisms of the products with different morphologies are also proposed.

1. Introduction

In recent years, semiconducting nanomaterials have received considerable attention due to their wide applications in the fabrication of optical and electronic devices. A group of $A_2^VB_3^{VI}$ (A = As, Sb, Bi; B = S, Se, Te) chalcogenides are semiconductors, which have many applications for different devices, such as television cameras with photoconducting targets, thermoelectric, electronic, optoelectronic, and IR spectroscopy [1–3]. Among them, bismuth sulfide (Bi_2S_3), a layered semiconductor with orthorhombic system, is a candidate for photodiode arrays and photovoltaic converters, due to its low energy gap (1.3 eV) which has been widely used in thermoelectric cooling technologies [1–5].

There are a variety of methods used to synthesize the chalcogenide, such as low temperature chemical reaction [4], hydrothermal method [5], solvothermal route [3,6], rapid polyol process [7], and microwave irradiation [2]. Among them, the microwave method exhibits much advantage. Since 1986, microwave irradiation was discovered to be an efficient heating process. It has a number of applications in chemistry and is widely used to synthesize zeolites and other inorganic materials. The microwave synthesis, which is generally quite fast, is simple and very efficient. It has an advantage over conventional method, by consuming shorter reaction time, and producing small particle size, narrow particle size distribution and phase with high purity [8].

In this study, the characterization of bismuth sulfide with different morphologies (nanoparticles, nanorods and nanotubes) synthesized by a microwave irradiation method is reported.

* Corresponding authors. Tel.: +66 53 943345; fax: +66 53 892277.
E-mail addresses: ttpthongtem@yahoo.com (T. Thongtem), phuruangrat@hotmail.com (A. Phuruangrat).

0167-577X/$ – see front matter © 2009 Elsevier B.V. All rights reserved.
doi:10.1016/j.matlet.2009.10.006

2. Experiment

Bi_2S_3 nanoparticles, nanorods and nanotubes were synthesized by a microwave irradiation method using the Bi^{3+}:S^{2-} molar ratio of bismuth nitrate pentahydrate ($Bi(NO_3)_3{\cdot}5H_2O$) and thioacetamide (CH_3CSNH_2, TA) or thiourea (NH_2CSNH_2, TU) at 2:3. They were dissolved in 30 ml different solvents (water, ethylene glycol (EG) and propylene glycol (PG)), which were followed by 0.5 ml 65 % HNO_3 adding with 30 min stirring at room temperature. Each precursor solution was transferred into a cooking microwave oven, and heated by a microwave radiation (2.45 GHz [9], multimode) at 180 W for 20 min. Finally, black precipitates were synthesized, separated by filtration, washed with water and ethanol several times, dried at 80 °C for 24 h, and collected for further characterization.

3. Results and discussion

XRD patterns of the products, synthesized using bismuth nitrate pentahydrate ($Bi(NO_3)_3{\cdot}5H_2O$) and two kinds of sulfur sources (CH_3CSNH_2 and NH_2CSNH_2) in different solvents (water, ethylene glycol and propylene glycol) by a microwave radiation at 180 W for 20 min, are shown in Fig. 1. All the diffraction peaks were indexed and specified as pure orthorhombic Bi_2S_3 phase of the JCPDS database no. 17–0320 [10]. No impurities such as Bi_2O_3, Bi and S were detected. The diffraction peaks are quite sharp, indicating that the products are well crystalline orthorhombic Bi_2S_3 structure.

The morphologies of all products were characterized using a transmission electron microscope. Fig. 2 shows the TEM and HRTEM images, and SAED patterns of Bi_2S_3 powders, synthesized by microwave irradiation using $Bi(NO_3)_3$ and TA in difference solvents. In aqueous solution, Bi_2S_3 (Fig. 2a) is composed of a number of nanoparticles with

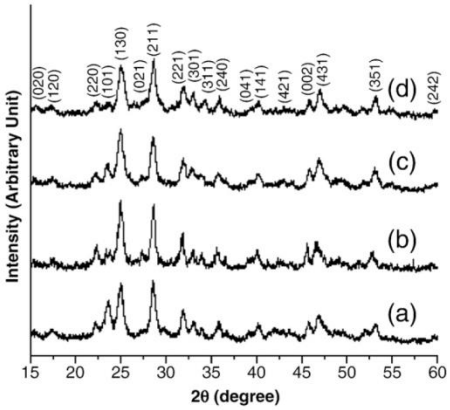

Fig. 1. XRD patterns of Bi_2S_3, synthesized by microwave irradiation using $Bi(NO_3)_3$ and difference sulfur sources: (a) TU in water, (b) TA in water, (c) TA in EG and (d) TA in PG.

their size range of 10–20 nm. SAED pattern (inset of Fig. 2a) shows several concentric rings, corresponding to the polycrystalline Bi_2S_3 [10]. When EG and PG were used as solvents, the morphologies of the products changed into nanorods with 20 nm diameter and 50–60 nm long in EG (Fig. 2b), and 10 nm diameter and 70–120 nm long in PG (Fig. 2d). Their HRTEM images (Fig. 2c and e) present the interplanar spaces of 3.97 Å, corresponding to the (220) crystallographic planes. SAED pattern of a Bi_2S_3 nanorod (Fig. 2f) indicated a single crystal with the [100] direction as zone axis. HRTEM images and SAED patterns demonstrated that the one dimensional Bi_2S_3 nanorods grew in the [001] direction.

In this case, the formation mechanism of Bi_2S_3 using $Bi(NO_3)_3$ and thioacetamide (CH_3CSNH_2, TA) in aqueous solution under microwave heating can be proposed as follows.

$$Bi(NO_3)_3 + H_2O \rightarrow BiONO_3 + 2HNO_3 \quad (1)$$

$$CH_3CSNH_2 + H_2O \rightarrow CH_3CONH_2 + H_2S \quad (2)$$

$$3H_2S + 2BiONO_3 \rightarrow Bi_2S_3 + 2HNO_3 + 2H_2O \quad (3)$$

$Bi(NO_3)_3$ was hydrolyzed by H_2O [1] to produce $BiONO_3$. At the same time, CH_3CSNH_2 reacted with H_2O under microwave irradiation, controlled by the slow release of S^{2-} ions from CH_3CSNH_2, to form CH_3CONH_2 and H_2S. Next step, the released H_2S reacted with $BiONO_3$ to form Bi_2S_3 nanoparticles. It is noteworthy that Bi_2S_3 nanoparticles did not form by the decomposition of the precursor complexes, but by the reaction of the released H_2S and $BiONO_3$ [8]. When either of the polyol compounds (EG and PG) was used as a solvent, it plays an

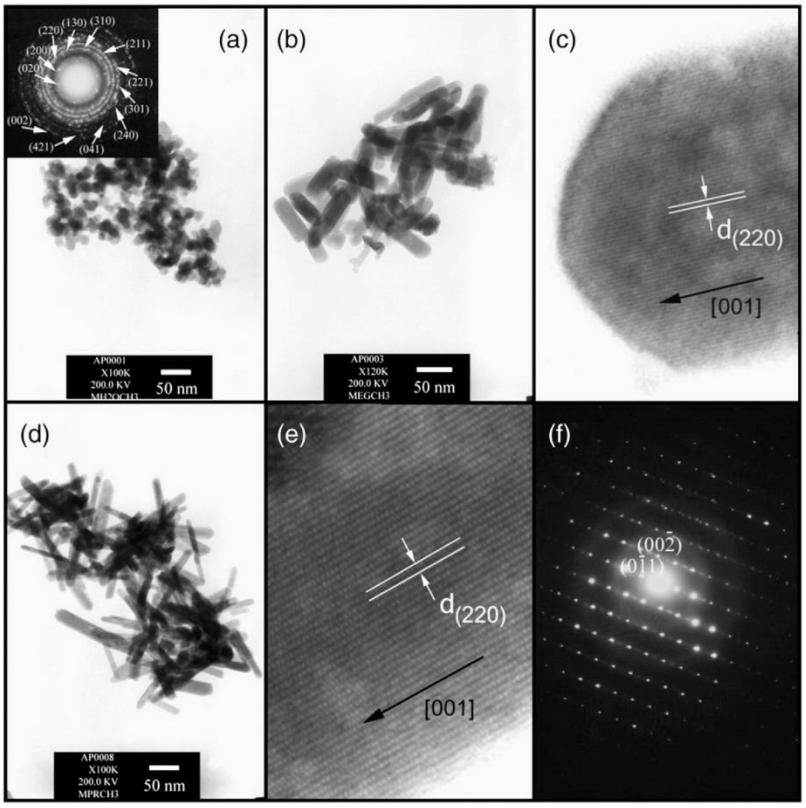

Fig. 2. TEM and HRTEM images, and SAED patterns of Bi_2S_3 powders, synthesized by microwave irradiation using $Bi(NO_3)_3$ and TA in different solvents: (a) water, (b and c) EG, and (d–f) PG.

important role in the formation of the Bi_2S_3 nanorods, by the effective complexing and stabilizing the surfaces of nanoparticles [11]. Bi_2S_3 nuclei formed and grew. They were capped on their side-walls by hydroxyl groups of the polyol solvent. Due to the effect of hydrogen bonds between hydroxyl groups, polyol molecules may exist as long chains and acted as a soft template, leading to the growth of Bi_2S_3 nuclei in the shape of nanorods. The slow release of S^{2-} could provide a stable monomer concentration. The combinations of these two facts promote the one-dimensional growth. In fact, the crystal morphology is an extrinsic embodiment of an intrinsic crystal structure. Bi_2S_3 is a typical layered structure that is possessed of the strongest chemical bonding along the c axis, and a weaker van der Waals attraction among the layered structure, which results in the anisotropic growth along the c axis [1,11].

Fig. 3 shows SEM image of the Bi_2S_3 nanotubes, synthesized using Bi $(NO_3)_3$ and TU as precursors in aqueous solution under microwave irradiation. They are 50 nm diameter and 2–3 μm long. Fig. 4a shows TEM image of the Bi_2S_3 nanotubes synthesized at the same condition as in Fig. 3. They are 30 nm diameter and 200–400 nm long. These nanotubes were broken and dispersive, during the sample preparation (ultrasonic vibration) for TEM analysis. The interplanar space (Fig. 4b) of the Bi_2S_3 nanotube was calculated and found to be 3.96 Å, corresponding to the space of the (220) plane of Bi_2S_3. It grew along the [001] direction.

When thiourea instead of thioacetamide was used for the formation of Bi_2S_3 in water, the reaction mechanism has another pathway. In this case, the proposed mechanism of Bi_2S_3 nanotubes using $Bi(NO_3)_3$ and TU in aqueous solution under microwave heating can be explained as follows [2,7,8].

$$Bi^{3+} + TU \rightarrow Bi\text{–}TU\ complexes \rightarrow Bi_2S_3 \quad (4)$$

The strong complex action between Bi^{3+} and TU leads to the formation of Bi–TU complexes in aqueous solution. Then, the Bi–TU complexes underwent the decomposition by the microwave irradiation for a certain period of time to synthesize Bi_2S_3 nanosheets, which subsequently rolled themselves up to form tubular structures [3,6]. The Bi–TU complexes are favorable for the oriented growth of the nanotubes. The microwave irradiation as heating environment provided a more rapid and simultaneous nucleation than the conventional one, due to its fast and uniform heating effect. The sulfur sources and solvents have the influence on the product morphologies and favor the synthesis of Bi_2S_3 with different pathways.

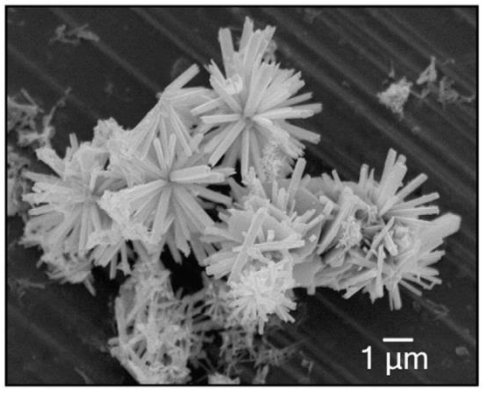

Fig. 3. SEM image of Bi_2S_3 synthesized using $Bi(NO_3)_3$ and TU in water under microwave irradiation at 180 W for 20 min.

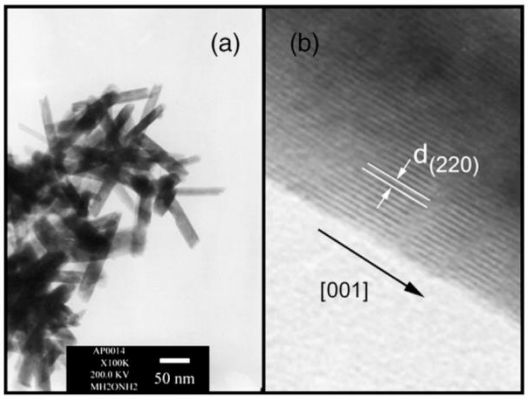

Fig. 4. TEM and HRTEM images of Bi_2S_3 synthesized using $Bi(NO_3)_3$ and TU in water under microwave irradiation at 180 W for 20 min.

4. Conclusions

Different morphologies of nanostructured bismuth sulfide including nanoparticles, nanorods and nanotubes have been successful synthesized by a microwave irradiation method at 180 W for 20 min, using Bi $(NO_3)_3 \cdot 5H_2O$ and CH_3CSNH_2 or NH_2CSNH_2 in various solvents (water, ethylene glycol and propylene glycol). XRD patterns, and TEM and SEM images showed that the products were orthorhombic structured Bi_2S_3 with the morphologies controlled by the sulfur sources and solvents.

Acknowledgement

The research was supported under the National Research University Project for Chiang Mai University, by the Commission on Higher Education, Ministry of Education, Thailand.

References

[1] Lu J, Han Q, Yang X, Lu L, Wang X. Mater Lett 2007;61:3425–8.
[2] Lu J, Han Q, Yang X, Lu L, Wang X. Mater Lett 2007;61:2883–6.
[3] Zhu G, Liu P, Zhou J, Bian X, Wang X, Li J, et al. Mater Lett 2008;62:2335–8.
[4] Sun Y, Han Q, Lu J, Yang X, Lu L, Wang X. Mater Lett 2008;62:3730–2.
[5] Phuruangrat A, Thongtem T, Thongtem S. Mater Lett 2009;63:1496–8.
[6] Liu X, Cui J, Zhang L, Yu W, Guo F, Qian Y. Nanotechnology 2005;16:1771–5.
[7] Shen G, Chen D, Tang K, Li F, Qian Y. Chem Phys Lett 2003;370:334–7.
[8] Liao XH, Wang H, Zhu JJ, Chen HY. Mater Res Bull 2001;36:2339–46.
[9] Bhunia S, Bose DN. J Cryst Growth 1998;186:535–42.
[10] Powder Diffract. File, JCPDS-ICDD, 12 Campus Boulevard, Newtown Square, PA 19073-3273, U.S.A., 2001.
[11] Zhang H, Wang L. Mater Lett 2007;61:1667–70.

Materials Letters 63 (2009) 833–836

Contents lists available at ScienceDirect

Materials Letters

journal homepage: www.elsevier.com/locate/matlet

Cyclic microwave-assisted spray synthesis of nanostructured $MnWO_4$

Somchai Thongtem [a], Surangkana Wannapop [a], Anukorn Phuruangrat [a], Titipun Thongtem [b,*]

[a] Department of Physics, Faculty of Science, Chiang Mai University, Chiang Mai 50200, Thailand
[b] Department of Chemistry, Faculty of Science, Chiang Mai University, Chiang Mai 50200, Thailand

ARTICLE INFO

Article history:
Received 4 September 2008
Accepted 8 January 2009
Available online 14 January 2009

Keywords:
Cyclic microwave-assisted spray synthesis
$MnWO_4$
Nano-plates in flower-like clusters

ABSTRACT

$MnWO_4$ with nano-plates in flower-like clusters was produced from the mists of the solutions containing $MnCl_2{\cdot}4H_2O$ and $Na_2WO_4{\cdot}2H_2O$ at different pH values by 300–900 W cyclic microwave radiation. The phase was detected by XRD and SAED, and was in accordance with that of the simulation. The flowers were characterized using SEM and TEM, and their lattice planes using HRTEM. The vibration spectra were characterized using Raman and FTIR spectrometers. Their photoluminescence is at 409–420 nm.

1. Introduction

Huebnerite ($MnWO_4$), an end member of wolframite ($Fe_xMn_{1-x}WO_4$) [1,2], has bulk electrical conductivity, relatively low melting point and novel magnetic property [3]. It displays photoluminescence with two main bands at 421 and 438 nm [3]. A number of processes have been used to produce $MnWO_4$, such as microemulsion-mediated solvothermal synthesis [3], solid-state metathetic approach [4] and microwave-assisted hydrothermal synthesis [1]. The purpose of the present research was to produce $MnWO_4$ with flower-like clusters using cyclic microwave-assisted spray synthesis. It is novel, simple, easy to handle and more economical to process.

2. Experiment

Each 0.005 mol of $MnCl_2{\cdot}4H_2O$ and $Na_2WO_4{\cdot}2H_2O$ was separately dissolved in 25 ml de-ionized water and mixed. The pH level was adjusted using NaOH. The mixture was composed of white colloid with very light weight. It was sprayed on glass slides 5 times to form the mists, which were subsequently put in a cyclic microwave radiation (30 s on for every 30 s interval) at 300–900 W for 1 h. Finally, brown powders were produced, and characterized using XRD (SIEMENS D500) operated at 20 kV, 15 mA and using K_α line from a Cu target, FTIR (BRUKER TENSOR27) with KBr as a diluting agent and operated in the range 400–1,500 cm^{-1}, Raman spectrometer (HORIBA JOBIN YVON T64000) of 50 mW Ar laser with 514.5 nm wavelength, SEM (JEOL JSM-6335F) operated at 15 kV, TEM (JEOL JEM-2010) as well as high resolution TEM (HRTEM) and selected area electron diffraction (SAED) operated at 200 kV, and photoluminescence (PL) spectrometer (PERKIN-ELMER LS50B) with a 290 nm excitation wavelength at room temperature. In addition, an electron diffraction pattern was

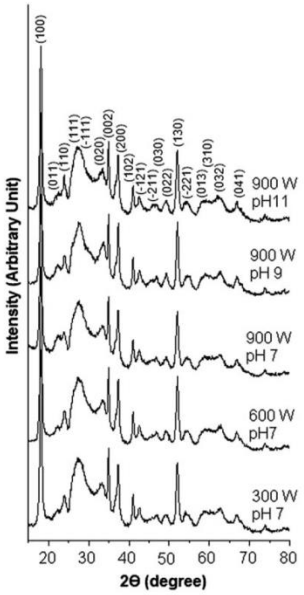

Fig. 1. XRD spectra of the products produced using different microwave powers and pH values.

* Corresponding author.
E-mail addresses: ttpthongtem@yahoo.com, ttpthongtem@hotmail.com (T. Thongtem).

0167-577X/$ – see front matter © 2009 Elsevier B.V. All rights reserved.
doi:10.1016/j.matlet.2009.01.016

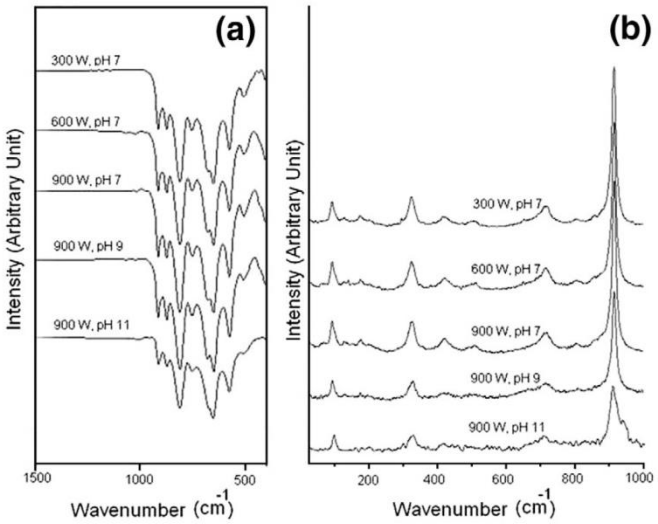

Fig. 2. (a) FTIR and (b) Raman spectra of $MnWO_4$ produced using different microwave powers and pH values.

simulated using CaRIne Crystallography 3.1 software [5] and compared with that interpreted from the experimental result.

3. Results and discussion

XRD spectra (Fig. 1) correspond to $MnWO_4$ with monoclinic crystal system, P2/c space group and huebnerite structure [6]. The spectra are very sharp showing that the products were composed of crystals. Their intensities and crystallite sizes were increased with the increase in the microwave powers which can play the role in arranging atoms in crystal lattices. Cyclic microwave energy was supplied to the mists on glass slides to overcome the potential barrier, which prevented the reaction to proceed. The mists were heated with uniformly and effectively, and the particles of controlled morphologies were produced. Calculated lattice parameters (nm) [7] (a=0.4821, b=0.5762 and c=0.4967) are very close to those of the JCPDS software [6]. These were specified that the products have monoclinic crystal system.

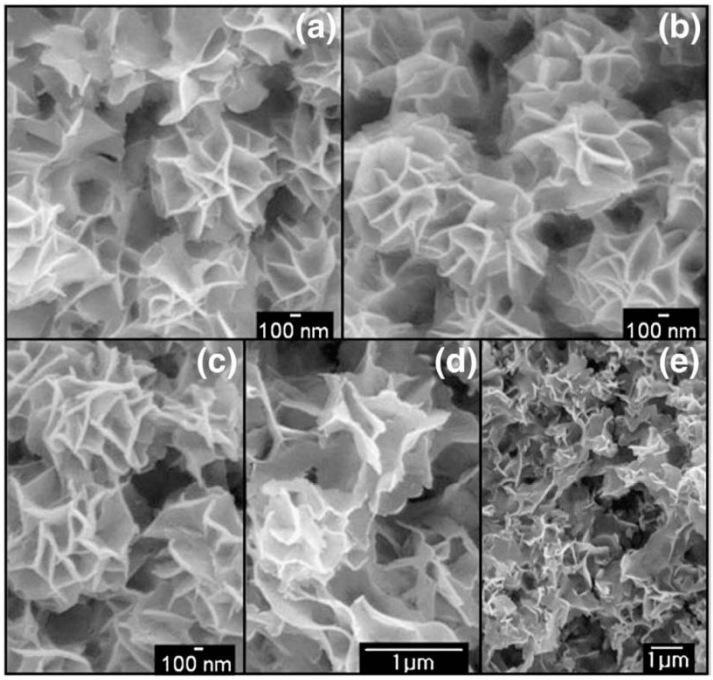

Fig. 3. SEM images of $MnWO_4$ produced using (a) 300 W, pH 7, (b) 600 W, pH 7, (c) 900 W, pH 7, (d) 900 W, pH 9 and (e) 900 W, pH 11.

FTIR spectra (Fig. 2a) of huebnerite structured products contain the inorganic modes on lower wavenumber side at 913, 871, 810, 753, 653 and 567 cm^{-1}, which are in accordance with those of other researchers [2,8]. They were specified as the internal stretching modes, namely $\nu_3(A_u)$ and $\nu_3(E_u)$ transitions [8].

Raman spectra (Fig. 2b) are very similar to those of huebnerite structured $MnWO_4$ [1]. A strong band at 912 cm^{-1} belongs to symmetric A_g mode and a weak band at 804 cm^{-1} to antisymmetric B_g mode of the terminal WO_2 groups. The 718 and 655 cm^{-1} bands respectively correspond to $\nu_{as}(B_g)$ and $\nu_{as}(A_g)$ modes of $(W_2O_4)_n$ chain. The 507 cm^{-1} band is assigned as symmetric A_g mode. Those at 326 and 419 cm^{-1} were specified by Fomichev and Kondratov as deformation modes [9], and by Daturi et al as r (B_g) and $\delta(A_g)$ modes of terminal WO_2 groups [10]. The 294 cm^{-1} band corresponds to $\nu_{def}(A_g)$ of cationic sublattices. Weak band at 177 cm^{-1}, specified as $\nu(A_g)$, was involved with Mn cations. The 101 and 138 cm^{-1} bands are the causes of interchain deformation and torsion modes. At lower wavenumber, vibration frequency is small and the structure is more regular. When the vibration is at higher wavenumber, its structure became more distorted [11].

SEM images of $MnWO_4$ were characterized. At a pH 7 and 300–900 W microwave powers (Fig. 3a–c), the products were composed of a number of nano-plates in flower-like clusters. The flowers became larger at higher powers. They have the largest size of 1,500 nm at 900 W. The present nanoflowers have almost the same size as those of other researchers, who produced $MnWO_4$ nanoflowers with the average size of 1,000 nm using microemulsion-mediated solvothermal synthesis [3]. But for the structure flowers, there are some differences between the two. During cyclic microwave-assisted synthesis, $MnCl_2{\cdot}4H_2O$ reacted with $Na_2WO_4{\cdot}2H_2O$ to produce $MnWO_4$ nuclei. Their growths are anisotropic. Plate-like particles were formed by the assemblage of monoclinic unit cells in three directions, but growth in normal direction to the plates was the slowest. Simultaneously, the plates clustered together to form flower-like colonies, which have different sizes, caused by random initiation. The flowers may contain some wavy plates, due to the microwave vibration frequency, internal stress and others. Different morphologies have the influence on the luminescent property as well. At a constant microwave power of 900 W and in strong basic solutions (Fig. 3d and e), some $[WO_4]^{2-}$ ions reacted with Na^+ ions of NaOH to

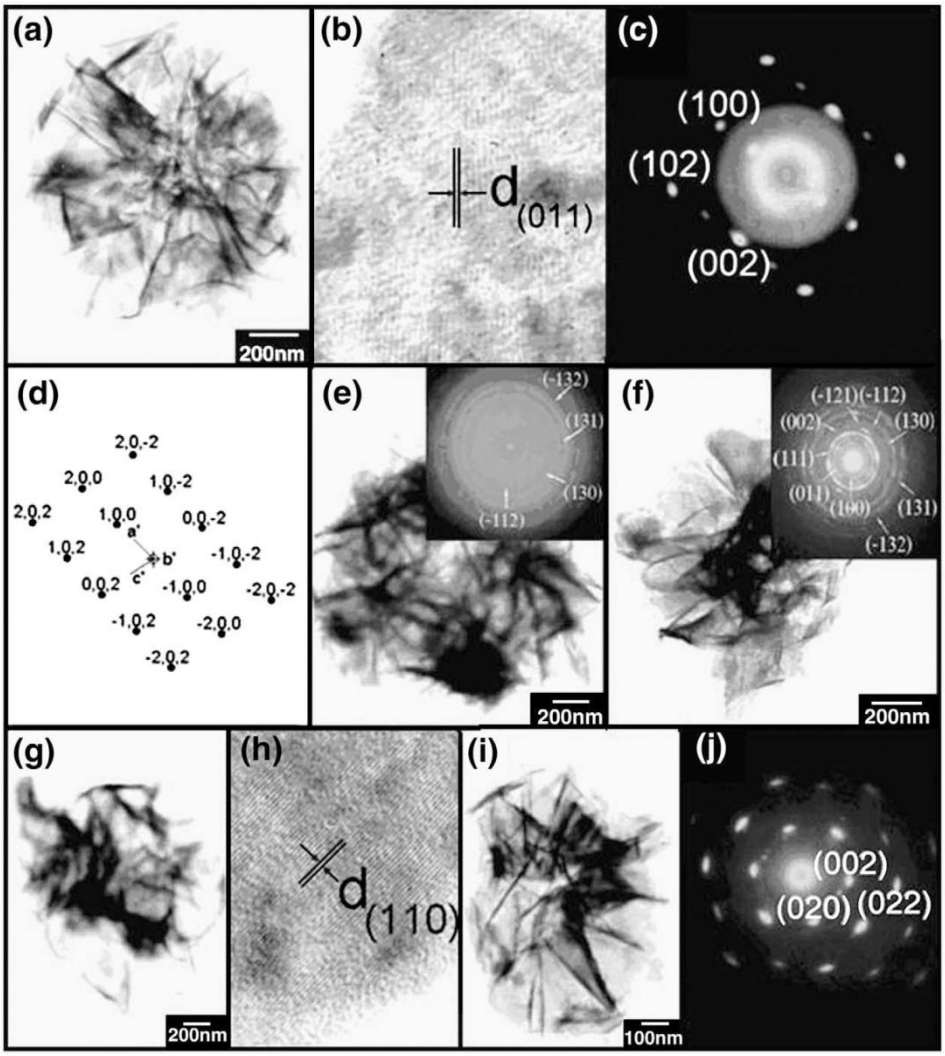

Fig. 4. TEM and HRTEM images, and SAED and simulation patterns of the products produced using (a–d) 300 W, pH 7, (e) 600 W, pH 7, (f) 900 W, pH 7, (g,h) 900 W, pH 9 and (i,j) 900 W, pH 11.

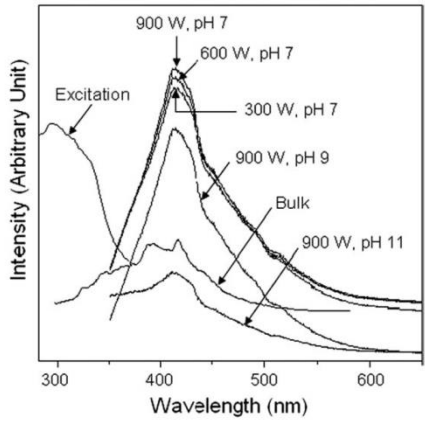

Fig. 5. PL spectra (290 nm excitation wavelength) of $MnWO_4$ produced using different microwave powers and pH values. $MnWO_4$ (bulk) was produced using the 200 °C calcination for 2 h.

form Na_2WO_4, which is very soluble in water. The remaining $[WO_4]^{2-}$ ions of a lesser extent were used to produce $MnWO_4$. The higher pH value was in the solution, the more loosened the flower-like colonies or clusters became. For the present research, the pH values played the role in determining the morphologies and defects of the products. In acidic solutions, $MnWO_4$ was soluble in the solution containing tungstic acid, and no precipitates were produced.

TEM images show that the products (Fig. 4a, e, f, g and i) were composed of a number of nano-plates with different orientations, which were clustered together in groups. HRTEM images (Fig. 4b and h) show (011) and (110) parallel planes of lattice arrays. Each array with the same orientation corresponds to a single crystal. SAED patterns (Fig. 4c and j) show diffraction patterns of systematic bright spots corresponding to lattice planes written in parentheses. Each pattern diffracted from a single crystal of $MnWO_4$ [6]. Calculated electron beams [12] are in [010] and [$\bar{1}$00] directions for the analyses of Fig. 4c and j, respectively. A simulated pattern with electron beam in [010] direction (Fig. 4d) [5] was composed of systematic array of spots. The a*, b* and c* vectors are in [100], [010] and [001] directions, respectively. Both interpreted and simulated patterns are in good accordance. But for Fig. 4e and f, the patterns appear as fully and continuously concentric rings. These imply that the products consisted of a number of nanocrystals with different orientations. Calculated interplanar spaces [13] correspond to the crystallographic planes in parentheses, specified as $MnWO_4$ [6].

Fig. 5 shows the excitation and photoluminescence (PL) spectra of the present research. By using a 290 nm excitation wavelength, PL spectra show the intrinsic peaks, caused by a nonlinear two-photon stimulation process [14]. It can be excited either in the excitonic absorption band or in the recombination process [15]. The emissions are blue spectra at 409–420 nm although the products were produced using different conditions. The results are in accordance with the 421 and 438 nm for nanostructure flowers [3], and 2.8±0.2 eV band gap for nanostructure clusters [4]. The PL intensities were increased with the increase in the microwave powers and acidity level. It is the highest at 900 W and a pH 7. The degree or extent of crystallinity was much improved at higher microwave powers, which promoted the number of charge transition (stronger intensity) of the products. In strong basic solutions, the lesser extent of $[WO_4]^{2-}$ ions was the cause to produce defects in the products. They became the least at the pH 7, which led to the strongest in intensity. Except for the product produced at 900 W and a pH 11, the emission intensities are higher than that of $MnWO_4$ (bulk) with 200 °C and 2 h calcination.

4. Conclusions

$MnWO_4$ with huebnerite structure was successfully produced using a cyclic microwave-assisted spray synthesis. It was composed of a number of nano-plates in flower-like clusters. Each nano-plate was composed of a number of crystallographic planes aligning in systematic array. Vibration wavenumbers provided the evidence of huebnerite structure of $MnWO_4$. PL emission shows the intrinsic peaks at 409–420 nm. The highest intensity was emitted from the 1500 nm flower-like clusters.

Acknowledgements

We are extremely grateful to the Thailand Research Fund (TRF), and National Research Council of Thailand (NRCT) for supporting the research.

References

[1] Kloprogge JT, Weier ML, Duong LV, Frost RL. Mater Chem Phys 2004;88:438–43.
[2] Ingham B, Chong SV, Tallon JL. Curr Appl Phys 2006;6:553–6.
[3] Xing Y, Song S, Feng J, Lei Y, Li M, Zhang H. Solid State Sci 2008;10:1299–304.
[4] Parhi P, Karthik TN, Manivannan V. J Alloys Compd 2008;465:380–6.
[5] Boudias C, Monceau D, CaRIne crystallography 3.1, 17 rue du Moulin du Roy, F-60300 Senlis, France (1989–1998).
[6] Powder Diffract. File, JCPDS Internat. Centre Diffract. Data, PA 19073-3273, U.S.A.; 2001. reference code: 74–1497.
[7] Suryanarayana C, Norton MG. X-Ray Diffract. NY: Plenum Press; 1998.
[8] Zhou H, Yiu Y, Aronson MC, Wong SS. J Solid State Chem 2008;181:1539–45.
[9] Fomichev VV, Kondratov OI. Spectrochim Acta 1994;50A:1113–20.
[10] Daturi M, Busca G, Borel MM, Leclaire A, Piaggio P. J Phys Chem B 1997;101:4358–69.
[11] Fu H, Pan C, Zhang L, Zhu Y. Mater Res Bull 2007;42:696–706.
[12] Thongtem T, Phuruangrat A, Thongtem S. Mater Lett 2008;62:454–7.
[13] Andrews KW, Dyson DJ, Keown SR. Interpret. Electr. Diffract. Patt. 2nd ed. NY: Plenum Press; 1971.
[14] Mikhailik VB, Bailiff IK, Kraus H, Rodnyi PA, Ninkovic J. Radiat Meas 2004;38:585–8.
[15] Pankratov V, Grigorjeva L, Millers D, Chernov S, Voloshinovskii AS. J Lumin 2001;94–95:427–32.

ELSEVIER Science Press

Trans. Nonferrous Met. Soc. China 19(2009) s100−s104

Transactions of Nonferrous Metals Society of China

www.tnmsc.cn

Characterization of $MnWO_4$ with flower-like clusters produced using spray pyrolysis

Somchai THONGTEM[1], Surangkana WANNAPOP[1], Titipun THONGTEM[2]

1. Department of Physics and Materials Science, Faculty of Science, Chiang Mai University, Chiang Mai, 50200, Thailand;
2. Department of Chemistry and Center for Innovation in Chemistry, Faculty of Science, Chiang Mai University, Chiang Mai, 50200, Thailand

Received 2 March 2009; accepted 30 May 2009

Abstract: $MnWO_4$ (huebnerite) with flower-like clusters of nano-plates was produced from the solutions containing $MnCl_2·4H_2O$ and $Na_2WO_4·2H_2O$ by the 300 ℃ spray pyrolysis. The phase was detected by X-ray diffraction (XRD) and selected area electron diffraction (SAED), and is in accordance with the results characterized using energy dispersive X-ray (EDX) analysis. The flower-like clusters of nano-plates were characterized using scanning and transmission electron microscopes (SEM and TEM), and their parallel lattice planes using a high resolution transmission electron microscope (HRTEM). Vibration spectra of the huebnerite structured products were characterized using Raman and Fourier transform infrared (FTIR) spectrometers. Their photoluminescence (PL) emissions are in the same spectral region at 405−412 nm.

Key words: spray pyrolysis; $MnWO_4$; flower-like clusters

1 Introduction

Wolframite ($Fe_xMn_{1-x}WO_4$) is an iron manganese tungstate mineral, which is the intermediate between iron-rich ferberite ($FeWO_4$) and manganese rich huebnerite ($MnWO_4$)[1−2]. $MnWO_4$ has bulk electrical conductivity, relatively low melting point and novel magnetic property[3], caused by its antiferromagnetic spin structure[4]. It can display photoluminescence (PL) emission with two main bands at 421 and 438 nm[3]. There are a number of processes used to produce $MnWO_4$, such as microwave-assisted synthesis[1], melt solution process[5], solvothermal route[6], aqueous salt metathesis reaction[7], sol-gel technique[8], ambient template synthesis[9], solid state metathetic approach [10], and surfactant-assisted complexation-precipitation method[4]. The purpose of this research was to produce $MnWO_4$ with flower-like clusters, from additive-free solution, using a spray pyrolysis method, which is simple and easy to handle, and more economical to process.

2 Experimental

Each 0.005 mol of $MnCl_2·4H_2O$ and $Na_2WO_4·2H_2O$ was separately dissolved in 25 mL de-ionized water and mixed for 10 min. The mixture was sprayed on glass slides 10 times, which were placed in a 300 ℃ furnace for 10−40 h. No other additives were used in the process. The products were washed with de-ionized water and 95% ethanol, and dried at 60 ℃ for 10 h. Then they were intensively characterized using a X-ray diffractometer (XRD) operated at 20 kV, 15 mA and using the K_α line from a Cu target, a Fourier transform infrared (FTIR) spectrometer with KBr as a diluting agent and operated in the range 500−1 600 cm^{-1}, a Raman spectrometer of 50 mW Ar laser with λ=514.5 nm, a scanning electron microscope (SEM) equipped with an energy dispersive X-ray (EDX) analyzer operated at 15 kV, a transmission electron microscope (TEM) and a high resolution transmission electron microscope (HRTEM) as well as the use of selected area electron

Corresponding author: Titipun THONGTEM; Tel: +66-53-943345; Fax: +66-53-892277; E-mail: ttpthongtem@yahoo.com; ttpthongtem@hotmail.com

diffraction (SAED) technique operated at 200 kV, and a photoluminescence (PL) spectrometer using a 293 nm excitation wavelength at room temperature[3].

3 Results and discussion

The XRD spectra of the products (Fig.1) were indexed using Bragg's law for diffraction. They correspond to that of the JCPDS software with reference code 74-1497[11]. They have P2/c space group of paramagnetic phase[5] and huebnerite structure[11]. It is composed of a number of edge-sharing (MnO_6) and (WO_6) octahedrons in a series of zigzags along *c* axis. Mn and W atoms are alternately arranged parallel to the (100) planes[5]. The broad XRD spectrum of glass (Fig.1), specified as amorphous phase, is also shown for comparison. Its spectrum was covered by the spectra of the products, showing that the deposited products on glass substrates are thick enough to prevent the X-ray beam from reflecting on them. The mists on glass slides are heated effectively, and a number of particles of controlled morphologies are produced. Atoms composing the products are arranged as systematic array in the crystal. Thus the spectra are very sharp. Their XRD intensities are also increased with the increase in the prolonged times which play the role in arranging atoms in crystal lattice.

The FTIR spectra (Fig.2(a)) of $MnWO_4$ with

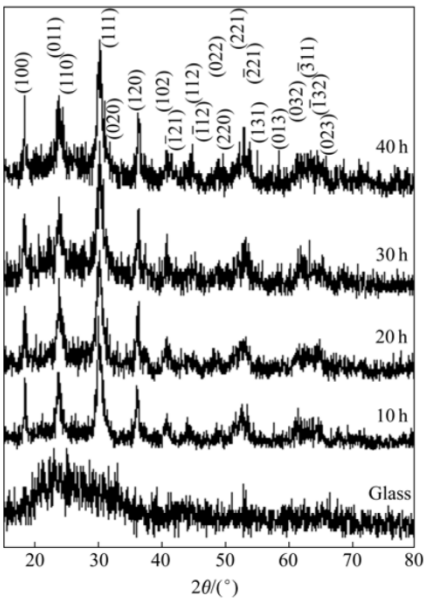

Fig.1 XRD spectra of glass and products on glass slides produced for 10, 20, 30 and 40 h

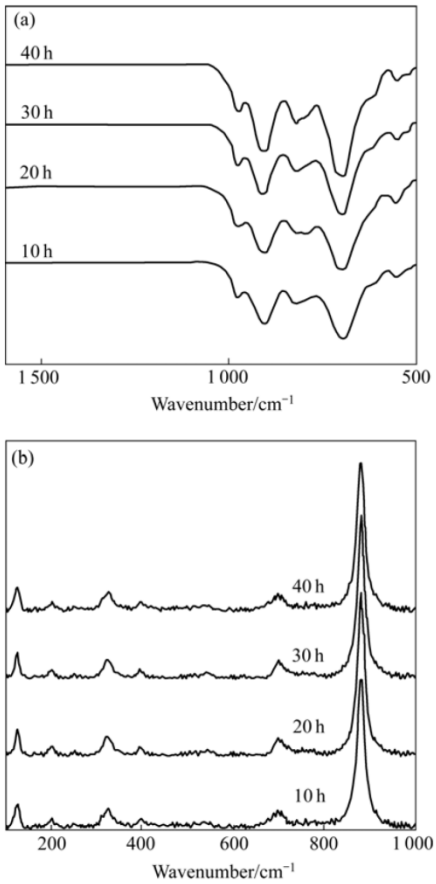

Fig.2 FTIR(a) and Raman spectra(b) of $MnWO_4$ produced for 10, 20, 30 and 40 h

huebnerite structure show the inorganic modes in the range 556−983 cm^{-1} of the low wavenumber side at 556, 694, 826, 908 and 983 cm^{-1}. The vibrations are in accordance with those of other researchers[2, 9]. These bands are assigned to be the internal stretching modes of $v_3(A_u)$ and $v_3(E_u)$ transitions[9].

The Raman spectra (Fig.2(b)) of the huebnerite structure are very similar to those of KLOPROGGE et al[1]. A medium strong band is detected at 125 cm^{-1}. The 200 cm^{-1} band is specified as $v(A_g)$ vibration involving the Mn cations, and the 245 cm^{-1} band as $v_{def}(A_g)$ vibration of the cationic sublattices. Those of 324 and 393 cm^{-1} bands are respectively specified by FOMICHEV and KONDRATOV as deformation modes[12], and by DATURI et al as $r(B_g)$ and $\delta(A_g)$ vibrations of terminal WO_2 groups[13]. The 538 cm^{-1} band is specified as the symmetric A_g vibration. The 698 cm^{-1} band corresponds to the $v_{as}(B_g)$ vibration of

$(W_2O_4)_n$ chain. The strongest intensity at 875 cm^{-1} belongs to symmetric A_g vibration of the terminal WO_2 groups. At lower Raman wavenumber, the vibration frequency is smaller and the structure is in the state of closing to normal crystal lattice. When the vibration is at higher wavenumber, its structure becomes more distorted[14]. The higher amplitude of the atomic vibration does, the more the product structure distorts, and the opposite is also true.

The SEM images of $MnWO_4$ (Fig.3) are characterized. The products are composed of a number of nano-plates in flower-like clusters. The flowers become larger, when the test is done in the longer period. They are the largest at 40 h test. For the present research, $MnCl_2{\cdot}4H_2O$ reacts with $Na_2WO_4{\cdot}2H_2O$ to produce $MnWO_4$ nuclei, which grows very rapidly by thermal heating. Their growths are anisotropic. Plate-like particles are produced, and simultaneously cluster to form flower-like colonies. They have different sizes, which are caused by random nucleation and growth processes.

Each product was put into a beaker containing de-ionized water. After ultrasonic vibration, the product-dispersed water was dropped on a copper grid and dried in ambient atmosphere for further analysis. TEM images (Figs.4(a), (c) and (d)) show that the products are composed of a number of nano-plates with different orientations. The product of Fig.4(a) clusters together in irregular shape. But for those of Figs.4(c) and (d), they become more dispersive. HRTEM image (Fig.4(b)) show a number of (011) lattice planes in systematic arrays of crystal structure. Each array with the same orientation corresponds to a single crystal. SAED patterns (Figs.4(a), (c) and (d)) show several concentric rings. They are diffusive and hollow, showing that the products are composed of a number of nanosized crystals with different orientations. The calculated interplanar spaces[15] were compared with those of the JCPDS software[11]. They correspond to a variety of crystallographic planes labeled in parentheses. They are specified that the products are $MnWO_4$.

The EDX spectra (Fig.5) reveal the presence of Mn, W and O in the products[16]. They are in good accordance with the phase detected using XRD and SAED. Au and C are also detected. They are caused by the sputtered Au on the products to improve the quality of SEM images, and by C tape used for sample mounting. Different energy peaks are detected due to the electronic

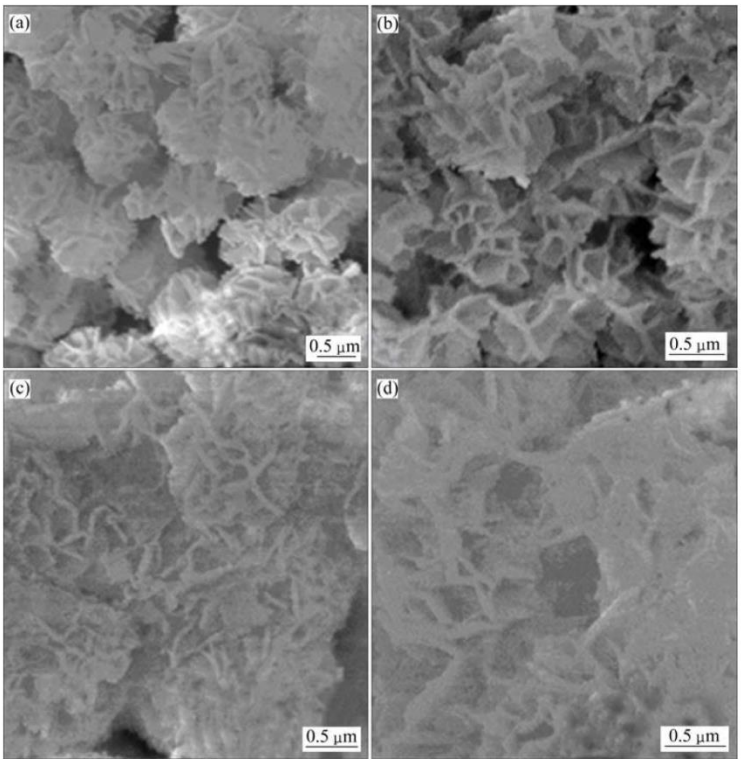

Fig.3 SEM images of $MnWO_4$ produced for 10(a), 20(b), 30(c) and 40 h(d)

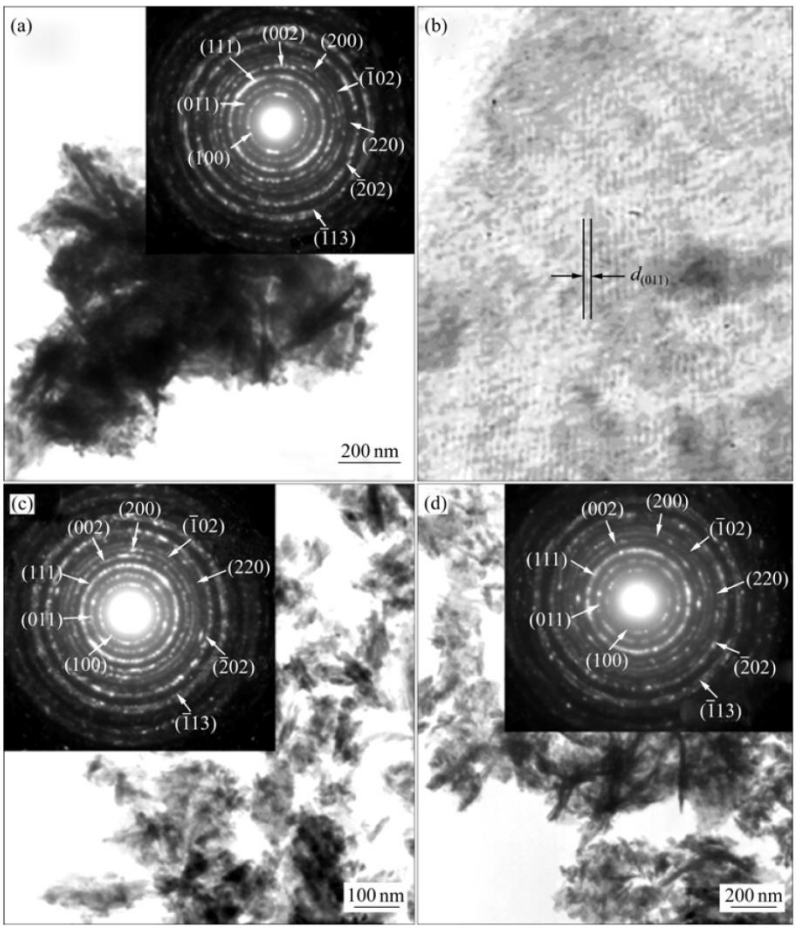

Fig.4 TEM and HRTEM images, and SAED patterns of $MnWO_4$ produced for 10 h(a, b), 20 h(c) and 30(d)

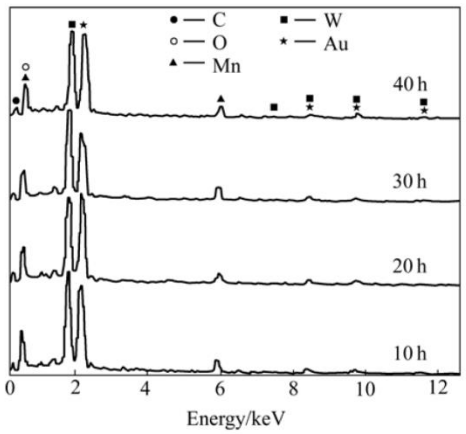

Fig.5 EDX spectra of $MnWO_4$ produced for 10, 20, 30 and 40 h

Table 1 Emission energies of atoms

Atom	Emission energy/keV	Spectral line
Mn	0.6	L_{α}
	5.9	$K_{\alpha1,2}$
W	1.8	M_{α}
	7.4	L_{l}
	8.4	L_{α}
	9.7	$L_{\beta1}$
	11.3	$L_{\gamma1}$
O	0.5	$K_{\alpha1,2}$
Au	2.1	M_{α}
	8.5	L_{l}
	9.7	L_{α}
	11.4	$L_{\beta1}$
C	0.3	$K_{\alpha1,2}$

transition of atoms as summarized in Table 1[16].

By using a 293 nm excitation wavelength[3], photoluminescence (PL) spectra (Fig.6) show electronic transition within $(WO_4)^{2-}$ anion molecular complex, associated with the intrinsic emission[17−18]. The intrinsic luminescence is caused by a nonlinear two-photon stimulation process[18]. They can be excited either in the excitonic absorption band or in the recombination process[19], resulting from the huebnerite-structured products. The intrinsic emission peaks are in the spectral region at 405−412 nm although the products are produced using different prolonged times. The results are in accordance with those detected by other researchers[3, 10]. PL intensities are increased with the increase in time. It is the highest at 40 h test. The shoulders or green bands, depended on the excitation type and sample quality, are caused by some defects and impurities, and are specified as the extrinsic emission[18].

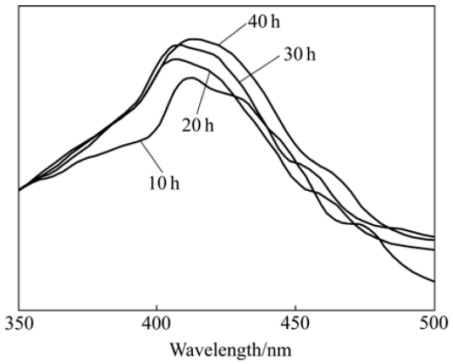

Fig.6 PL spectra of $MnWO_4$ produced for 10, 20, 30 and 40 h

4 Conclusions

$MnWO_4$ on glass slides were successfully produced by the 300 ℃ spray pyrolysis method. The phase are $MnWO_4$, composing of Mn, W and O. The products are flower-like clusters of nano-plates, each of which is composed of a number of crystallographic planes aligning in lattice array. Vibration wavenumbers provide the evidence of huebnerite structure, corresponding to the product phase. PL emission shows the narrow central peaks in the same spectral region at 405−412 nm. The highest intensity peak is emitted from the product of 40 h test.

Acknowledgements

We are extremely grateful to the Thailand Research Fund (TRF) and Center for Innovation in Chemistry (PERCH-CIC), Commission on Higher Education (CHE), Ministry of Education, Thailand, for financial support.

References

[1] KLOPROGGE J T, WEIER M L, DUONG L V, FROST R L. Microwave-assisted synthesis and characterization of divalent metal tungstate nanocrystalline minerals: Ferberite, hübnerite, sanmartinite, scheelite and stolzite[J]. Mater Chem Phys, 2004, 88: 438−443.

[2] INGHAM B, CHONG S V, TALLON J L. Layered tungsten oxide-based hybrid materials incorporating transition metal ions[J]. Curr Appl Phys, 2006, 6: 553−556.

[3] XING Y, SONG S, FENG J, LEI Y, LI M, ZHANG H. Microemulsion-mediated solvothermal synthesis and photo-luminescent property of 3D flowerlike $MnWO_4$ micro/nanocomposite structure[J]. Solid State Sci, 2008, 10: 1299−1304.

[4] LEI S, TANG K, FANG Z, HUANG Y, ZHENG H. Synthesis of $MnWO_4$ nanofibres by a surfactant-assisted complexation-precipitation approach and control of morphology[J]. Nanotech, 2005, 16: 2407−2411.

[5] HEYER O, HOLLMANN N, KLASSEN I, JODLAUK S, BOHATÝ L, BECKER P, MYDOSH J A, LORENZ T, KHOMSKII D. A new multiferroic material: $MnWO_4$[J]. J Phys: Condens Matter, 2006, 18: L471−L475.

[6] CHEN S J, CHEN X T, XUE Z, ZHOU J H, LI J, HONG J M, YOU X Z. Morphology control of $MnWO_4$ nanocrystals by a solvothermal route[J]. J Mater Chem, 2003, 13: 1132−1135.

[7] MONTEMAYOR S M, FUENTES A F. Electrochemical characteristics of lithium insertion in several 3D metal tungstates ($MnWO_4$, M = Mn, Co, Ni and Cu) prepared by aqueous reactions[J]. Ceram Internat, 2004, 30: 393−400.

[8] QU W, WLODARSKI W, MEYER J U. Comparative study on micromorphology and humidity sensitive properties of thin-film and thick-film humidity sensors based on semiconducting $MnWO_4$[J]. Sensors Actuat B, 2000, 64: 76−82.

[9] ZHOU H, YIU Y, ARONSON M C, WONG S S. Ambient template synthesis of multiferroic $MnWO_4$ nanowires and nanowire arrays[J]. J Solid State Chem, 2008, 181: 1539−1545.

[10] PARHI P, KARTHIK T N, MANIVANNAN V. Synthesis and characterization of metal tungstates by novel solid-state metathetic approach[J]. J Alloys Comp, 2008, 465: 380−386.

[11] Powder diffraction files[S]. JCPDS-ICDD. USA, PA 19073-3273, 2001.

[12] FOMICHEV V V, KONDRATOV O I. Vibrational spectra of compounds with the wolframite structure[J]. Spectrochim Acta, 1994, 50A: 1113−1120.

[13] DATURI M, BUSCA G, BOREL M M, LECLAIRE A, PIAGGIO P. Vibrational and XRD study of the system $CdWO_4$-$CdMoO_4$[J]. J Phys Chem B, 1997, 101: 4358−4369.

[14] FU H, PAN C, ZHANG L, ZHU Y. Synthesis, characterization and photocatalytic properties of nanosized Bi_2WO_6, $PbWO_4$ and $ZnWO_4$ catalysts[J]. Mater Res Bull, 2007, 42: 696−706.

[15] ANDREWS K W, DYSON D J, KEOWN S R. Interpretation of electron diffraction patterns[M]. 2nd ed. New York: Plenum Press, 1971: 14−15.

[16] X-ray Absorption and Emission Energies[M]. Oxford Instruments Analytical, Halifax Rd., High Wycombe Bucks HP12 3SE, UK.

[17] TREADAWAY M J, POWELL R C. Luminescence of calcium tungstate crystals[J]. J Chem Phys, 1974, 61: 4003−4011.

[18] MIKHAILIK V B, BAILIFF I K, KRAUS H, RODNYI P A, NINKOVIC J. Two-photon excitation and luminescence of a $CaWO_4$ scintillator[J]. Radiat Measur, 2004, 38: 585−588.

[19] PANKRATOV V, GRIGORJEVA L, MILLERS D, CHERNOV S, VOLOSHINOVSKII A S. Luminescence center excited state absorption in tungstates[J]. J Luminesc, 2001, 94/95: 427−432.

(Edited by YUAN Sai-qian)

Available online at www.sciencedirect.com
ScienceDirect
Ceramics International 35 (2009) 2087–2091
CERAMICS INTERNATIONAL
www.elsevier.com/locate/ceramint

Short communication

Characterization of $CoWO_4$ nano-particles produced using the spray pyrolysis

Somchai Thongtem [a,*], Surangkana Wannapop [a], Titipun Thongtem [b]

[a] *Department of Physics, Faculty of Science, Chiang Mai University, Chiang Mai 50200, Thailand*
[b] *Department of Chemistry, Faculty of Science, Chiang Mai University, Chiang Mai 50200, Thailand*

Received 9 July 2008; received in revised form 3 October 2008; accepted 6 November 2008
Available online 9 December 2008

Abstract

$CoWO_4$ nano-particles were produced by spraying the solution containing $CoCl_2{\cdot}6H_2O$ and $Na_2WO_4{\cdot}2H_2O$ on glass slides at 250–450 °C. XRD, SAED, TEM, HRTEM and AFM revealed the presence of $CoWO_4$ nano-particles with their crystallographic planes aligning in systematic array. Raman spectra provide evidence of the wolframite structure, corresponding to the product phase. Their photoluminescence (PL) emissions show the narrow central peaks of the same spectral region at 411–419 nm.

Keywords: Spray pyrolysis; $CoWO_4$; Nano-particles

1. Introduction

Naturally, wolframite and scheelite are the majorities of tungsten ores formed on earth [1]. Their structures are controlled by cationic radii. Small radii (<0.077 nm) are in favor of forming wolframite structure, but large radii (>0.099 nm) favor scheelite structure [2,3]. Each of the tungsten atoms is surrounded by six oxygen atoms for wolframite [4], and by four oxygen atoms for scheelite [5]. The metal tungstates have very attractive properties in scintillation, electro-optics and microwave applications [1,4,6]. There are a number of methods used to prepare nano-structured tungstates, such as microwave-assisted synthesis [2,7], hydrothermal and solvothermal processes [3,6,8–10] and sonochemistry [11].

2. Experimental

For the present research, each 0.2 mol of $CoCl_2{\cdot}6H_2O$ and $Na_2WO_4{\cdot}2H_2O$ was dissolved in 25 ml de-ionized water and mixed. The mixture was stirred for 10 min and sprayed on glass slides 10 times in the temperature range 250–450 °C. The slides were kept at constant temperatures for 10 h, and removed from the furnace. No other additives were used in the process. It is simple and easy to handle, and more economical to process in large scale. The products were washed with de-ionized water and 95% ethanol, dried at 60 °C for 10 h and intensively characterized.

3. Results and discussion

Comparing XRD spectra (Fig. 1a) with that of the JCPDS software (reference code: 15-0867) [12], the products were $CoWO_4$ with monoclinic crystal system and P2/a space group. The phase has wolframite structure [2,3,13]. During characterization, X-ray beam reflected and diffracted with the crystalline products and sharp spectra were produced. Their strongest

* Corresponding author.
E-mail addresses: schthongtem@yahoo.com, sthongtem@hotmail.com (S. Thongtem).

0272-8842/$34.00
doi:10.1016/j.ceramint.2008.11.014

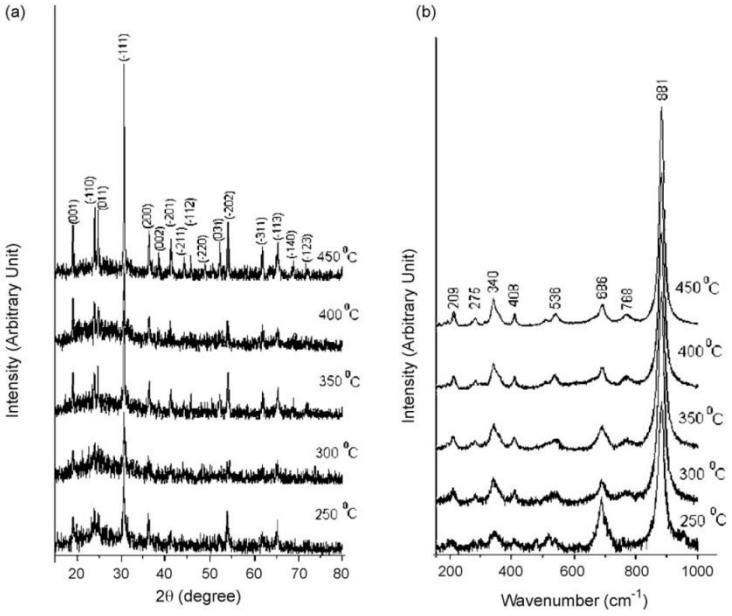

Fig. 1. (a) XRD and (b) Raman spectra of the products produced at different temperatures.

intensity peaks are at $2\theta = 30.6^\circ$ and diffracted from (−1 1 1) planes of the products. No other characteristic peaks of impurities were detected showing that the products are at a pure phase. XRD intensities were increased with the increase in the test temperatures which can play the role in arranging atoms in systematic order. Their crystallite sizes were enlarged as well. At 450 °C, XRD peaks have the strongest intensities and the crystallite sizes are the largest.

Raman spectra (Fig. 1b) of the wolframite structured products compose of a strong band at 881 cm^{-1} and a weak band at 768 cm^{-1}. They were specified as symmetric and asymmetric stretching vibrations of terminal W=O bonds, respectively [13]. The weak bands at 686 and 536 cm^{-1} are caused by the asymmetric and symmetric stretching of O–W–O bridges of $(W_2O_4)_n$ polymeric chain. Those at 408 and 340 cm^{-1} are tentatively specified as the in-plane deformation and rotation of W–O bonds (terminal and bridging), respectively. Weak band at 275 cm^{-1} is caused by Co–O stretching. The 209 cm^{-1} band is likely to be out-of-plane vibration [13]. The more Raman wavenumber of the atomic vibration does, the more the product structure distorts, and the opposite is also true [8].

TEM images (Fig. 2a–c) show a number of nano-particles influenced by test temperatures. Diameters (D) of 300 nano-particles at different temperatures were measured [14], and are shown in Fig. 3a–e. The products are composed of a number of nano-particles with different sizes. Their distributions are very close to the normal curves. The average sizes are in the ranges 16.25–25.23, 17.03–25.27, 22.65–42.59, 40.34–61.50 and 46.81–68.27 nm at 250, 300, 350, 400 and 450 °C, respectively. The values of log(D) and T^{-1} (Fig. 3f) matched very well with the Arrhenius-type equation [15],

$$\log D = 3.06 - \frac{946.21}{T}.$$

It shows that particle sizes increased monotonically with the increase in test temperature. It was assumed that heat capacity of formation of the nano-particles is constant with temperature. Calculated activation energy is 1.306×10^{-20} J·(particle)$^{-1}$, which is the energy consumption for every particle formed in the present process. Particle shape and size influence the PL as well. During the process, growth rates of the particles were very low. A number of nano-sized particles formed. HRTEM image (Fig. 2d) shows that a number of (0 0 2) lattice planes are in systematic array. Each grain is composed of atomic planes in the same direction, and corresponds to a single crystal. SAED patterns (Fig. 2a–c) show a number of random and continuous bright spots. They are so close that they form fully concentric rings. These indicate that the products consist of nano-sized crystals with different orientations. Calculated interplanar spaces

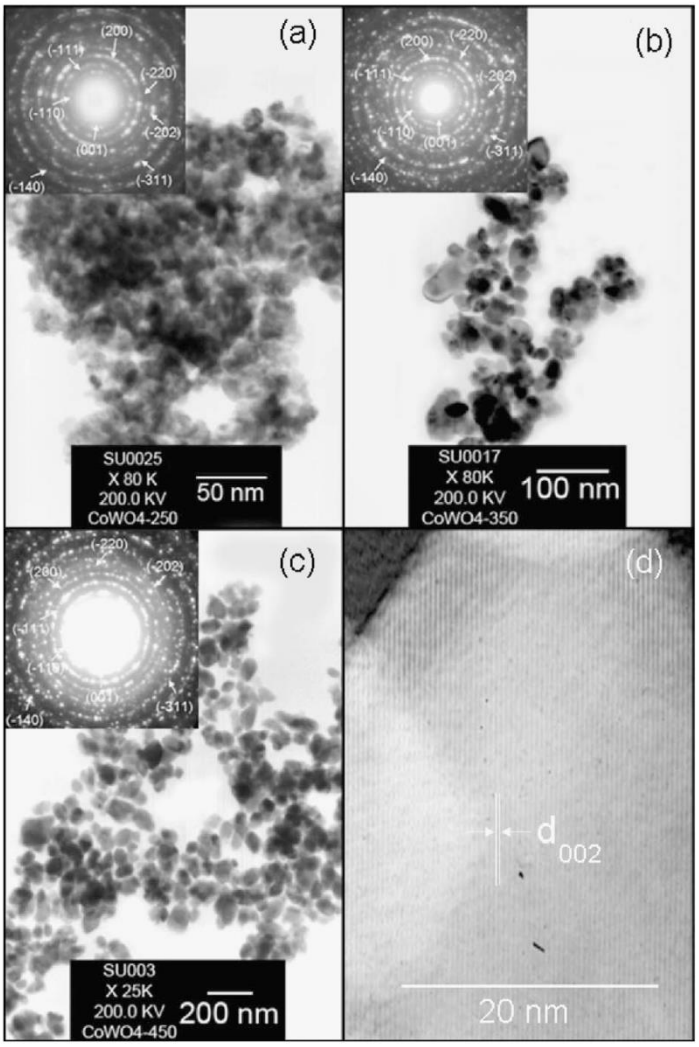

Fig. 2. (a–c) TEM images and SAED patterns of the products produced at 250, 350 and 450 °C, respectively. (d) HRTEM image of $CoWO_4$ produced at 450 °C.

[7] were compared with those of the JCPDS software [12]. They correspond to (0 0 1), (−1 1 0), (−1 1 1), (2 0 0), (−2 2 0), (−2 0 2), (−3 1 1) and (−1 4 0) planes of the crystals and were specified as $CoWO_4$.

The sprayed products on glass substrates at different temperatures were characterized using AFM. Fig. 4 shows the evolution of roughness with the test temperatures. The deposition did not form regular patterns. Surfaces of the substrates were very rough due to the deposited products. Their roughness at 250, 300, 350, 400 and 450 °C are 24.7, 45.8, 51.3, 95.5 and 106.9 nm, respectively. Roughness increased with the increase in test temperature. Nucleation and growth processes led to the irregular patterns on the substrates. Generally, vibration at high temperature was more violent than that at low temperature. Atoms and particles have more chance to arrange themselves in good order which is in favor with flat surface. For the present analysis, growth is the dominant process.

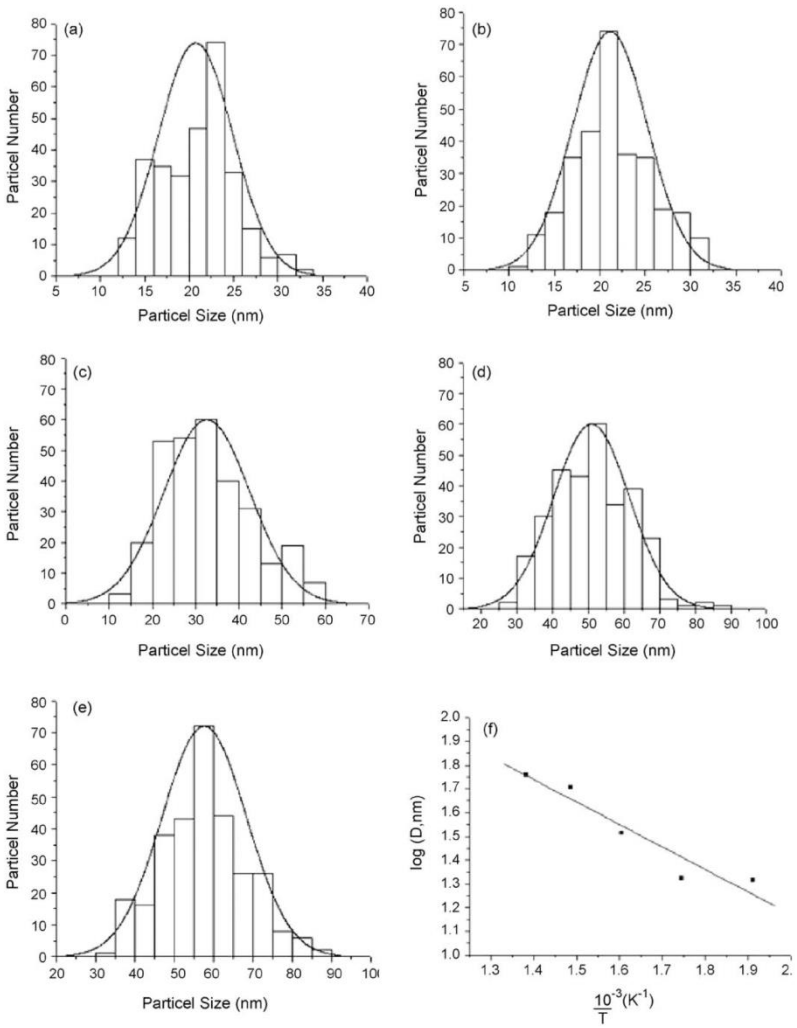

Fig. 3. (a–e) Particle size distributions of $CoWO_4$ produced at 250, 300, 350, 400 and 450 °C, respectively. (f) Particle size dependency on the temperature.

By using a 300 nm excitation wavelength, photoluminescence (PL) spectra (Fig. 5) show the narrow central (intrinsic) peaks with their surrounding shoulders [16–18]. The emission peaks are in the same spectral region at 411–419 nm although the products were produced at different temperatures. The intrinsic luminescence was caused by the annihilation of a self-trapped exciton, which formed excited $[WO_6]^{6-}$ complex [19]. It can be excited either in the excitonic absorption band or in the recombination process [19], due to the wolframite-structured products. The shoulders are from some defects and impurities. PL intensity is controlled by the number of charged transfers in the products. For present analysis, their intensities increased with the increase in test temperatures. It is the highest at 450 °C. Shapes, sizes, degree of crystallinity and others can play a role in emission as well.

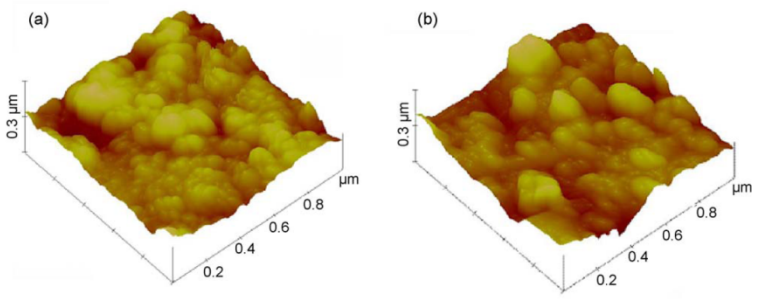

Fig. 4. AFM images of $CoWO_4$ deposited on glass substrates at (a) 350 and (b) 450 °C.

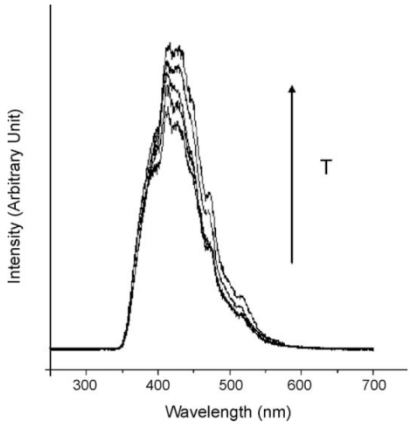

Fig. 5. PL spectra of $CoWO_4$ nano-particles produced at 250, 300, 350, 400 and 450 °C.

4. Conclusion

$CoWO_4$ nano-particles were successfully produced by spray pyrolysis at 250–450 °C. The products are pure phase with wolframite structure. They are composed of a number of nano-particles with their crystallographic planes aligning in a systematic array. Particle sizes and roughness increased with the increase in test temperature, due to the growth process. The particle sizes at different temperatures fitted very well with the Arrhenius-type equation. Vibrations of atoms provided evidence of the wolframite structure, corresponding to the product phase. PL emission shows the narrow central peaks of the same spectral region at 411–419 nm.

Acknowledgement

We are extremely grateful to the Thailand Research Fund for supporting the research.

References

[1] S.H. Yoon, D.W. Kim, S.Y. Cho, K.S. Hong, J. Eur. Ceram. Soc. 26 (2006) 2051–2054.
[2] J.T. Kloprogge, M.L. Weier, L.V. Duong, R.L. Frost, Mater. Chem. Phys. 88 (2004) 438–443.
[3] S.H. Yu, B. Liu, M.S. Mo, J.H. Huang, X.M. Liu, Y.T. Qian, Adv. Funct. Mater. 13 (2003) 639–647.
[4] R. Dafinova, K. Papazova, A. Bojinova, J. Mater. Sci. Lett. 17 (1998) 237–239.
[5] A. Golubović, R. Gajić, Z. Dohčević-Mitrović, S. Nikolić, J. Alloys Compd. 415 (2006) 16–22.
[6] X.C. Song, E. Yang, R. Ma, H.F. Chen, Y. Zhao, J. Nanopart. Res. 10 (2008) 709–713.
[7] T. Thongtem, A. Phuruangrat, S. Thongtem, Curr. Appl. Phys. 8 (2008) 189–197.
[8] H. Fu, C. Pan, L. Zhang, Y. Zhu, Mater. Res. Bull. 42 (2007) 696–706.
[9] L. Zhen, W.S. Wang, C.Y. Xu, W.Z. Shao, L.C. Qin, Mater. Lett. 62 (2008) 1740–1742.
[10] T. You, G. Cao, X. Song, C. Fan, W. Zhao, Z. Yin, S. Sun, Mater. Lett. 62 (2008) 1169–1172.
[11] T. Thongtem, A. Phuruangrat, S. Thongtem, Appl. Surf. Sci. 254 (2008) 7581–7585.
[12] Powder Diffract. File, JCPDS Internat. Centre Diffract. Data, PA 19073-3273, U.S.A., 2001.
[13] S.L. González-Cortés, T.C. Xiao, P.M.F.J. Costa, S.M.A. Rodulfo-Baechler, M.L.H. Green, J. Mol. Catal. A 238 (2005) 127–134.
[14] Scion Image, Scion Corp., 82 Worman's Mill Ct., Suite H, Frederick, MD 21701, 1997–2005.
[15] S. Thongtem, C. Boonruang, T. Thongtem, M. McNallan, Surf. Interface. Anal. 37 (2005) 765–769.
[16] Y. Zhang, N.A.W. Holzwarth, R.T. Williams, Phys. Rev. B 57 (1998) 12738–12750.
[17] M.J. Treadaway, R.C. Powell, J. Chem. Phys. 61 (1974) 4003–4011.
[18] V.B. Mikhailik, I.K. Bailiff, H. Kraus, P.A. Rodnyi, J. Ninkovic, Radiat. Meas. 38 (2004) 585–588.
[19] V. Pankratov, L. Grigorjeva, D. Millers, S. Chernov, A.S. Voloshinovskii, J. Lumin. 94–95 (2001) 427–432.